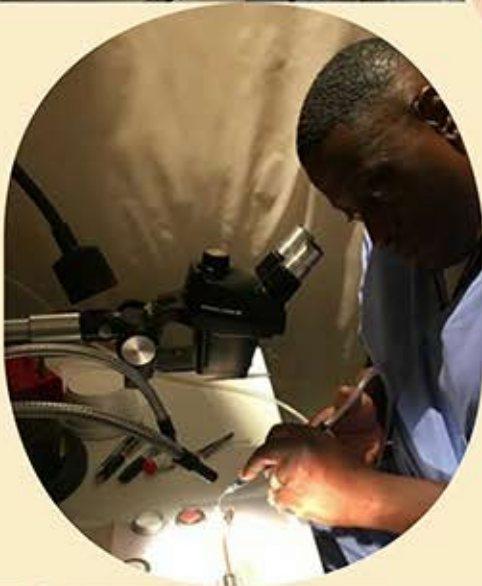
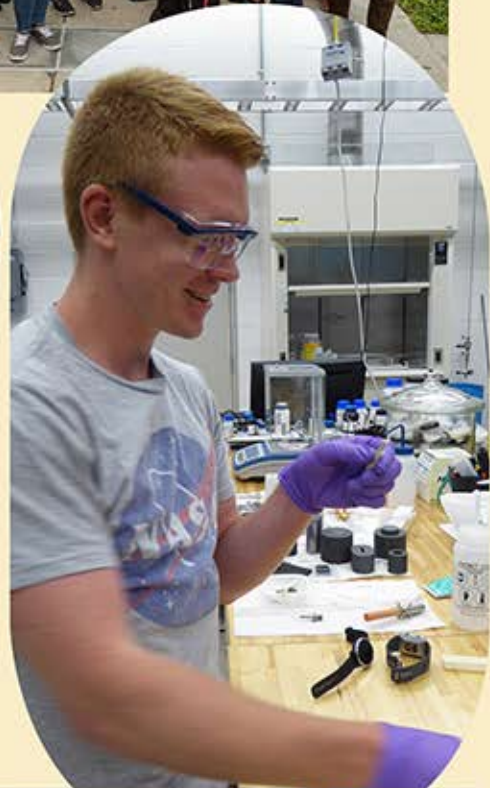
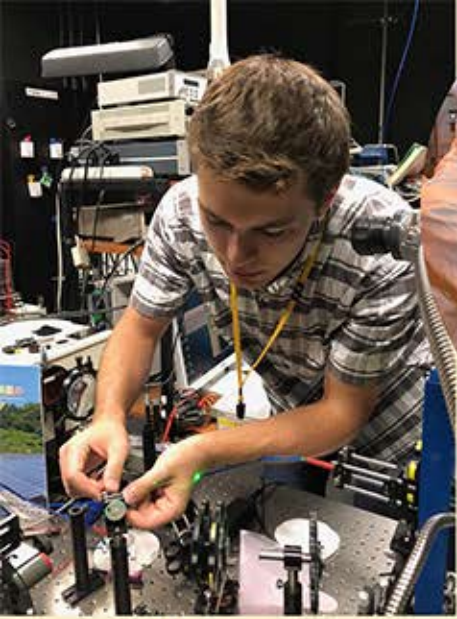


2018 REU REPORTS

• CNF • CNF iREU •
• CTECH • KEP •
• PARADIM •
• PARADIM CU • PARADIM JHU •

**RESEARCH EXPERIENCE FOR
UNDERGRADUATES PROGRAMS**



2018 REU Final Reports

Research Experience for Undergraduates (REU) Programs Represented:

Cornell NanoScale Science & Technology Facility (CNF) • CNF International (CNF iREU)

Center for Transportation, Environment & Community Health (CTECH)

Keeping the Ezra Promise (KEP)

Platform for the Accelerated Realization, Analysis, and Discovery of Interface Materials (PARADIM)

PARADIM @ Cornell University (CU) • PARADIM @ Johns Hopkins University (JHU)

Table of Contents

Understanding Consumer Decisions
on Alternative Fuel Vehicles Using
Discrete Choice Models. 2

Sayeeda Tuz Jahin Aishee, 2018 CTECH REU

Topics in Nano-Biophotonics: Fabrication
of Plasmonic Metasurfaces that Attract and
Spectroscopically Interrogate Cancer Cells 4

Vivek Anil, 2018 CNF REU

Site Specific Dual Modification of Native
Antibodies Via Microbial Transglutaminase 6

John Bohn, 2018 KEP

Conjugated Nanoparticle Induced
Apoptosis in Cancer Cells 8

Isabel Castillo, 2018 CNF iREU

Understanding the Structure
of Germanium Sulfide (GeS) 10

Miguel Castro-Rivera, 2018 PARADIM REU

Investigation of Intrinsic Defects in
Sputtered Titanium Oxide Surfaces 12

Peter Chang, 2018 CNF iREU

STEM Imaging and Composition
Mapping of Multiferroic Oxides. 14

Mr. Anthony Coleman, 2018 PARADIM REU

Implementing a Functional ARPES System 16

Stephanie Eberly, 2018 PARADIM REU

Wetting Layer Engineering
for GaSb Quantum Dots 18

Carl Felstiner, 2018 CNF iREU

Investigating the Structure of Multiferroic Oxides
with STEM Imaging and Diffraction Mapping ... 20

Iryna Glushchenko, 2018 PARADIM REU

Automating a Cryogenic Transport System
for Measuring Quantum Materials. 22

Ken Ho Tai Ran, 2018 PARADIM CU REU

New Photopatterning Materials
for Advanced Lithography 24

Jordan Phillip Howard-Jennings, 2018 CNF REU

High Dynamic Gas Pressure Single Crystal Growth 26 <i>Zachary Kennedy, 2018 PARADIM JHU REU</i>	Development of a MEMS Tool to Study the Physics of Water and Ice 46 <i>Kody Whisnant, 2018 CNF REU</i>
Non-Equilibrium Investigations of Canted Antiferromagnet Under Flowing Electrical Current 28 <i>Yonghun Lee, 2018 PARADIM CU REU</i>	Fabricating 2D Silica with Atomic Layer Deposition 48 <i>Reed Yalisove, 2018 CNF REU</i>
Growing and Characterizing Monolayer Transition Metal Dichalcogenides (2D TMDs) Materials for PARADIM Users 30 <i>Cesar Lema, 2018 PARADIM REU</i>	Systematic Floating Zone Single Crystal Growth for Machine Learning Objectives.. .. 50 <i>Jessica Zahn, 2018 PARADIM JHU REU</i>
On Chip Production of GM1 for the Treatment of Huntington’s Disease... .. 32 <i>Regina Mannino, 2018 KEP</i>	Spin-Orbit Torques from SrRuO₃-SrIrO₃ Epitaxial Heterostructure 52 <i>Cyrus Zeledon, 2018 PARADIM CU REU</i>
Growing and Designing 2D Transition Metal Dichalcogenide (2D-TMDC) Materials for PARADIM Users 34 <i>Marcus Marracci, 2018 PARADIM REU</i>	Development of a Multipurpose Ultrahigh Vacuum System for Electrical and Optical Measurements of Surface-Modified Quantum Materials 54 <i>William Zhang, 2018 PARADIM CU REU</i>
STM Observation and Manipulation of Dimethyl Indolino Benzo-Nitrile (IBN) Molecules on Au <111> Surfaces. 36 <i>Paola Perez, 2018 CNF iREU</i>	INDEX 56
Development of Nanoplasmonic Mo-Au Photocatalysts for Ammonia Synthesis... .. 38 <i>Joshua Romo, 2018 KEP</i>	
Characterization of Magnetic Thin Films for Actuating Origami Devices 40 <i>Sierra Russell, 2018 CNF REU</i>	
Modeling Random Memristive Nanowire Networks... .. 42 <i>Daniel Teal, 2018 CNF iREU</i>	
Synthesis, Preparation, and Thermoelectric Properties of Synthetic Mineral Sulfides 44 <i>Jace Waybright, 2018 CNF iREU</i> <i>NOT INCLUDED IN THIS BOOK</i>	

Photography Credits

The cover image is from “STM Observation and Manipulation of Dimethyl Indolino Benzo-Nitrile (IBN) Molecules on Au <111> Surfaces” by Paola Perez, 2018 CNF iREU Intern — the full report is on page 36.

The photographs of the CNF, CNF iREU, CTECH, KEP, PARADIM, and PARADIM CU interns were taken by Don Tennant, the interns, NIMS site staff, and Cornell University Photography.

This brochure and the reports are all online at <http://paradim.cornell.edu/education> and http://www.cnf.cornell.edu/cnf_2018reu.html

Cornell NanoScale Science & Technology Facility (CNF)

CNF International (CNF iREU)

Center for Transportation, Environment & Community Health (CTECH)

Keeping the Ezra Promise (KEP)

**Platform for the Accelerated Realization, Analysis,
and Discovery of Interface Materials (PARADIM);**

PARADIM @ Cornell • PARADIM @ Johns Hopkins

Research Experience for Undergraduates (REU) Programs

2018 REU Final Reports



Starting with the white t-shirt: Felstiner; Chang; Perez; Waybright; Castillo; Teal



Inset Zak Kennedy, JHU; Nucci; Romo; Howard-Jennings; Russell; Bohn; Glushchenko; Mammino; Yalisove; Eberly; Aishee; Lee; Anil; Whisnant; Zhang; Zeledon; Castro-Rivera; Ho; Marracci; Lema; Coleman; Mallison; Inset Jessica Zahn, JHU

Understanding Consumer Decisions on Alternative Fuel Vehicles Using Discrete Choice Models

Sayeeda Tuz Jahin Aishee, 2018 CTECH REU Intern

Engineering School, Cornell University

*REU Program: 2018 Center for Transportation Environment and Community Health
Research Experience for Undergraduates (CTECH REU) Program*

CTECH REU Principal Investigator: Prof. Linda Nozick, Civil and Environmental Engineering, Cornell University

CTECH REU Mentor: Dr. Esther Chiew, Civil and Environmental Engineering, Cornell University

*Primary Sources of CTECH REU Funding: Center for Transportation Engineering and Community Health,
Cornell University, and the National Science Foundation*

Contact: sta48@cornell.edu, lkn3@cornell.edu, wc437@cornell.edu

Website: http://www.cnf.cornell.edu/cnf_2018reu.html

Abstract:

In a rapidly transforming technological world, air pollution levels are highly dependent on people’s decision to buy less polluting cars. In this study, we used Discrete Choice Modeling to analyze data of vehicle choice to recommend the most attractive attributes of alternative fuel vehicles to businesses. With this information, businesses could cater to customers’ preferences, resulting in higher sales of alternative fuel vehicles and, ultimately, reducing toxic air pollution. Using R, a computer modeling software, we found that consumers highly value cost efficiency, high-performance, and having a variety of fueling options. These attributes could increase the market share of alternative fuel vehicles so that six out of seven people would buy an alternative fuel vehicle.

Summary of Research:

In 2016, 6.1 million deaths were caused by air pollution related health risks [1]. Additionally, 28% of US global warming emissions are caused by the transportation sector; that’s more than any other sector in the nation. We wanted to combat this by having more consumers opt for alternative fuel vehicles instead of gas vehicles. To figure out what people want the most, we analyzed a data set from a survey of around 1000 individuals from California, shown in Figure 1. Individuals were required to choose a vehicle from different alternatives while considering their attributes. We used discrete choice modeling as the data included continuous variables such as purchase price, operational cost, and range along with dummy variables such as engine type, vehicle type, and performance. Discrete models specifically analyze choices that customers make between products or services. They produce utility, or the willingness to buy a product, to predict the probability of choosing an alternative. Utility is usually directly related to probability, so the higher the utility, the higher the probability.

	Vehicle A	Vehicle B	Vehicle C
Vehicle Type	Large SUV	Mini Car	Compact PU
Engine Type	Gasoline	Electric	Hybrid
Performance	Top Speed 80MPH	Top Speed 80MPH	Top Speed 80MPH
	0-60: 16 Seconds	0-60: 16 Seconds	0-60: 16 Seconds
Total Purchase Price*	\$36,298	\$16,594	\$33,025
Operating Cost (less routine maintenance)	\$56.70/mo	\$7.85/mo	\$29.10/mo
Range (in miles)	300 - 500	140 - 150	400 - 700

*Total Purchase Price is the amount customers can expect to pay for the vehicle new at the dealership

Figure 1: One question from the survey. Consumers had to choose one vehicle while considering the attributes.

We used Multinomial Logit Models from the realm of Discrete Choice Models to portray our data set. The key inaccuracy of this model comes from only being able to detect systematic variation and suggesting proportional substitution. Systematic variation doesn't account for inherent biases of individuals or any random choices they make. Proportional substitution implies that if the probability for choosing one alternative increases the probability for choosing the other alternatives decrease proportionally. We derived a function that includes all the alternative specific attributes and produces generic coefficients. We tested that this was the most accurate function using Log-Likelihood Ratio Test. Since this function produced the highest log likelihood ratio compared to the other functions, which excluded some attributes, it was the most representative of the data set.

Results and Conclusions:

Using the function (Figure 2), we derived coefficients for all the attributes shown in Figure 3. The negative coefficients of the continuous variables signify that as the actual value of the attributes increase, people would be

```
mlogit(formula = choice ~ pprice + ocost + range + electric +
  hybrid + hperf + lperf + mini + small + large + sSUV + mSUV +
  lSUV + compPU + fullPU + minivan + 0, data = data1, method = "nr",
  print.level = 0)
```

Figure 2: The R command that lists the function used to analyze the data set.

```
Frequencies of alternatives:
      1      2      3
0.33172 0.35337 0.31491

nr method
5 iterations, 0h:0m:0s
g'(-H)^-1g = 0.000247
successive function values within tolerance limits

Coefficients :
      Estimate Std. Error z-value Pr(>|z|)
pprice  -0.0532178  0.0017621 -30.2019 < 2.2e-16 ***
ocost    -0.0265221  0.0017894 -14.8219 < 2.2e-16 ***
range    0.4458927  0.0769181  5.7970 6.752e-09 ***
electric 1.0975419  0.0768052 -14.2899 < 2.2e-16 ***
hybrid   0.7546017  0.0428463 17.6118 < 2.2e-16 ***
hperf    0.1884808  0.0217873  8.6510 < 2.2e-16 ***
lperf    -0.2556816  0.0222666 -11.4827 < 2.2e-16 ***
mini     1.3091796  0.0796035 -16.4462 < 2.2e-16 ***
small    -0.3351288  0.0687550 -4.8742 1.092e-06 ***
large    0.1452564  0.0690467  2.1037 0.0354010 *
sSUV     -0.0055082  0.0660140 -0.0834 0.9335016
mSUV     0.6510700  0.0713574  9.1241 < 2.2e-16 ***
lSUV     0.4632372  0.0834508  5.5510 2.840e-08 ***
compPU   -0.3520306  0.0687153 -5.1230 3.007e-07 ***
fullPU   0.0283859  0.0718255  0.3952 0.6926905
minivan  0.2633300  0.0708870  3.7148 0.0002034 ***
---
Signif. codes:  0 '***' 0.001 '**' 0.01 '*' 0.05 '.' 0.1 ' ' 1

Log-Likelihood: -6939.9
```

Figure 3: The summary of the data set with coefficients and significance levels.

less inclined to choose an alternative with the increased amount of attribute and vice versa. For example, since the coefficient for purchase price (pprice) is negative, it implies that as pprice increases the willingness of a customer to choose an alternative with an increased pprice decreases. It's the opposite with range, since the coefficient is positive. People are more likely to choose an alternative with an increased range. When it comes to the discrete variables, if a coefficient for an attribute is negative people are less likely to choose an alternative with that attribute. According to Figure 3, people are less willing to buy a vehicle that is electric (negative coefficient) and more likely to buy a vehicle that is hybrid (positive coefficient). However, overall 1/5th of the market was willing to buy electric vehicles and that market share increased when a vehicle was a small or a compact vehicle. When the pprice of a vehicle was lower than the median pprice of the market, the operational cost (ocost) of a vehicle was lower than the median ocost of the market, and the range of the vehicle was greater than the median range of the market, 84.41% of the market chose to buy hybrid or electric vehicles. Consumers would also pay \$16,000 more for a hybrid vehicle instead of a gas vehicle, \$83 more for one extra mile in an electric vehicle, and \$4,000 more for a high-performance vehicle over a mid-performance vehicle.

Future Work:

Analyzing updated data based on real market consumer decisions from around the nation would provide a more accurate prediction of the market shares.

Acknowledgements:

I would like to thank my professor Dr. Linda Nozick, my mentor Dr. Esther Chiew, the program coordinators Celia Szczepura-McLean, Joe Rowe, and Melanie-Claire Mallison. This project was funded with the help of Center for Transportation Engineering and Community Health, Cornell University, and the National Science Foundation.

References:

- [1] "Air Pollution Contributed To More Than 6 Million Deaths In 2016 [Infographic]." McCarthy, Niall. Forbes, Forbes Magazine, 18 Apr. 2018, www.forbes.com/sites/niallmccarthy/2018/04/18/air-pollution-contributed-to-more-than-6-million-deaths-in-2016-infographic/#4a28acaf13b4.
- [2] "Sources of Greenhouse Gas Emissions." EPA, Environmental Protection Agency, 11 Apr. 2018, www.epa.gov/ghgemissions/sources-greenhouse-gas-emissions.

Topics in Nano-Biophotonics: Fabrication of Plasmonic Metasurfaces that Attract and Spectroscopically Interrogate Cancer Cells

Vivek Anil, 2018 CNF REU Intern

**Engineering Science, Physics,
The Pennsylvania State University**

*REU Program: 2018 Cornell NanoScale Science & Technology Facility Research Experience for Undergraduates Program
CNF REU Principal Investigator: Professor Gennady Shvets, School of Applied and Engineering Physics, Cornell University*

*CNF REU Mentors: Dr. Steven He Huang, School of Applied and Engineering Physics, Cornell University;
Dr. Maxim Shcherbakov, School of Applied and Engineering Physics, Cornell University*

*Primary Source of CNF REU Funding: National Science Foundation via the National Nanotechnology
Coordinated Infrastructure (NNCI) Grant No. NNCI-1542081*

Contact: vivek3anil@gmail.com, gs656@cornell.edu, hh623@cornell.edu, mrs356@cornell.edu

Website: http://www.cnf.cornell.edu/cnf_2018reu.html

Abstract:

Current methods for detecting cancer rely heavily on imaging or tumor markers that are often inaccurate and inefficient. Meanwhile, Fourier transform infrared spectroscopy (FTIR) has been widely studied as a method for label-free biosensing because the characteristic vibrational modes of most biomolecules oscillate at mid-IR frequencies [1]. More recently, plasmonic metasurfaces have drawn interest because they can be engineered to have a resonant electromagnetic response over a broad range of frequencies. Their unique properties enable them to confine light to nanoscale regions (high local field concentration) and have a wavelength-specific response, which is ideal for molecular sensing by spectroscopy [2]. Infrared (IR) plasmonic metamaterials are particularly useful for biosensing: the resonant response of these materials can be tuned to match that of the vibrational modes in biomolecules so that biomolecules can be sensed via surface-enhanced IR spectroscopy. We investigated the use of plasmonic metasurfaces for detection of selected vibrational modes by fabricating gold metasurfaces on an infrared-transparent calcium fluoride (CaF_2) substrate; the metasurfaces were patterned using electron-beam lithography. We successfully fabricated three different types of structures: Fano resonant asymmetric metamaterials (FRAMMs), nanoantennae, and nanoslits, and validated the presence of resonance peaks by performing FTIR on the metasurfaces to obtain reflectance spectra. By adjusting the structures' dimensions, the resonances (quality factor $Q \sim 10$) seen in each structure's reflectance spectra were tuned to match the amide I ($\sim 1650 \text{ cm}^{-1}$) and carbohydrate ($\sim 2900 \text{ cm}^{-1}$) molecular resonances, which are present in cells. Our results demonstrate the potential to develop an improved method of cancer detection via surface-enhanced IR spectroscopy with engineered plasmonic metasurfaces.

Summary of Research:

Introduction. Biomolecular components in cells possess characteristic vibrational modes in the IR, which can be spectroscopically probed to obtain information from cells [1]. The signals from these vibrational modes are often weak, and so we propose using a plasmonic metasurface to enhance these signals. The dimensions and spatial arrangements of the structures were chosen such that the metasurface resonated at frequencies similar to cellular vibrations. Each set of structures with the same dimensions were fabricated together, with consistent spacing between structures, in squares, called pixels. This was done for the sake of testing simplicity: each pixel could be probed as an individual metasurface, and so we could assess how well each set of dimensions enabled us to tune to a particular resonance.

Fabrication. For the FRAMMs and nanoantennae, the fabrication process was as follows: CaF_2 wafers were washed and dried thoroughly, and then $\sim 240 \text{ nm}$ PMMA was spin-coated onto the wafers. The wafer was then baked at 170°C . We patterned the metasurface using the JEOL 9500 electron-beam lithography system. We developed the PMMA from the patterned areas using a methyl isobutyl ketone-isopropanol developer (MIBK:IPA 1:3). We evaporated 10 nm Cr and 70 nm Au onto the substrate at 1 \AA/s each. Remaining PMMA was lifted-off in an overnight acetone bath. The process for fabricating nanoslits was similar, except that we evaporated Au between cleaning and spin-coating, and added an extra ion mill etching step after development and before lift-off.

FTIR Experiment. The metasurface was integrated into a polydimethylsiloxane microfluidic chamber; a solution — phosphate buffer saline (PBS), ethanol, or DI water — was injected into the chamber, and an IR spectroscopy was done on the metasurface (probing pixel by pixel) in the chamber using a Bruker-Hyperion FTIR-microscope system.

Results and Conclusions:

We were able to successfully tune our FRAMM (pi structure) and nanoantenna resonances to the desired frequencies, as seen in Figure 1 — where the “Pi_5” ($d = 225.1 \text{ nm}$ and $L = 1.727 \mu\text{m}$ as in Figure 2a) and “Nanoantenna_2” ($w = 234.8 \text{ nm}$ and $L = 1.693 \mu\text{m}$ as in Figure 2b) pixels resonate at the amide I frequency ($\sim 1650 \text{ cm}^{-1}$) and the “Pi_3” ($d = 66.19 \text{ nm}$ and $L = 0.9555 \mu\text{m}$ as in Figure 2a) and “Nanoantenna_1” ($w = 238.3 \text{ nm}$ and $L = 0.9624 \mu\text{m}$ as in Figure 2b) pixels resonate at the carbohydrate frequency ($\sim 2900 \text{ cm}^{-1}$). In general, we saw that as we increase the size of FRAMM structures, we decrease the position of the resonant frequency (Figure 3); this relationship proved useful for tuning resonances.

We also successfully fabricated nanoslits and adjusted structure dimensions ($w \sim 50 \text{ nm}$ and $L \sim 700 \text{ nm}$ for “slit_1” and $w \sim 50 \text{ nm}$ and $L \sim 1500 \text{ nm}$ for “slit_2”) such that we observed the interference between the nanoslit peaks and the deionized (DI) water ($\sim 1660 \text{ cm}^{-1}$ and 3400 cm^{-1}) and ethanol ($\sim 3000 \text{ cm}^{-1}$ and 3400 cm^{-1}) resonances (Fig.4). Figure 4 suggests the potential for biosensing by tuning resonances to observe similar interference between biomolecular vibrations in cells and our metasurfaces’ resonances. Furthermore, integrating our metasurface into the microfluidic chamber shows even more promise for developing a device for biosensing by surface-enhanced spectroscopy.

Future Work:

Future work will include refining nanoslit fabrication and resonance tuning, attaching cancer cells to the metasurface and performing FTIR to obtain biomolecular information from cells, comparing nanoantennae and nanoslits to determine which shows greater near field enhancement, and analyzing spectra to understand how we can use them to distinguish between healthy and cancerous cells.

Acknowledgements:

I would like to thank my PI, Prof. Gennady Shvets, my mentors, Dr. Steven Huang and Dr. Maxim Shcherbakov, CNF staff, and the National Science Foundation (Grant No. NNCI-1542081) for giving me the opportunity to participate in this Research Experience for Undergraduates Program.

References:

- [1] Baker, M. J., et al. (2014). Using Fourier transform IR spectroscopy to analyze biological materials. *Nature Protocols*,9, 1771-1791.
- [2] Wu, C., et al. Fano-resonant asymmetric metamaterials for ultrasensitive spectroscopy and identification of molecular monolayers. *Nature Materials*,11(1), 69-75.

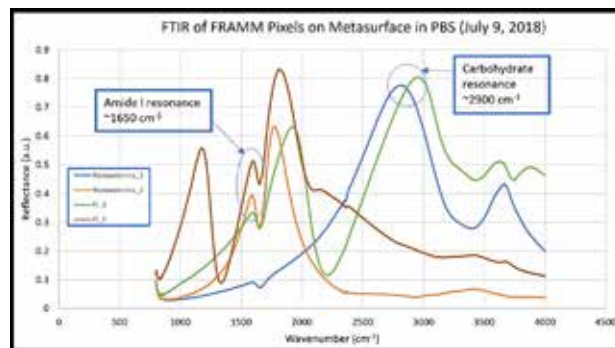


Figure 1: Reflectance spectra of FRAMM and nanoantenna pixels in PBS, tuned to match amide I and carbohydrate resonances.

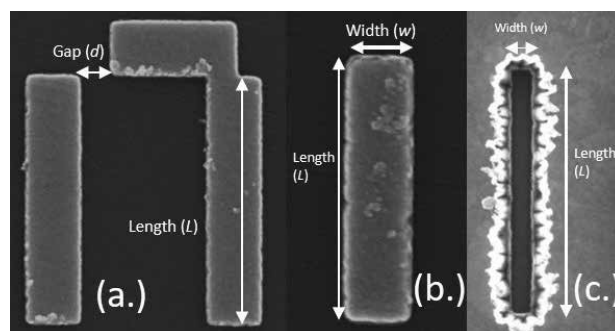


Figure 2: SEM images (taken at 20.00 kV) of (a) FRAMM (pi), (b) nanoantenna, and (c) nanoslit structures.

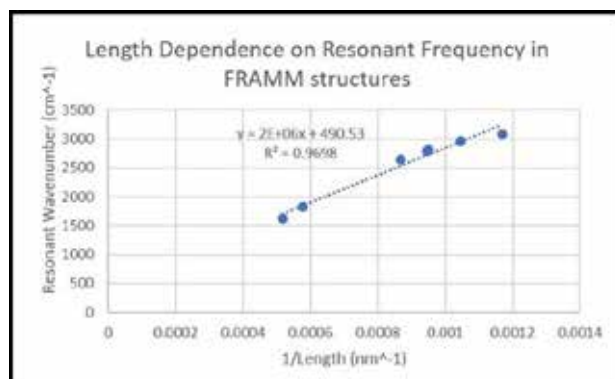


Figure 3: Relationship between length and position of the resonance seen in reflectance spectra for FRAMMs in PBS.

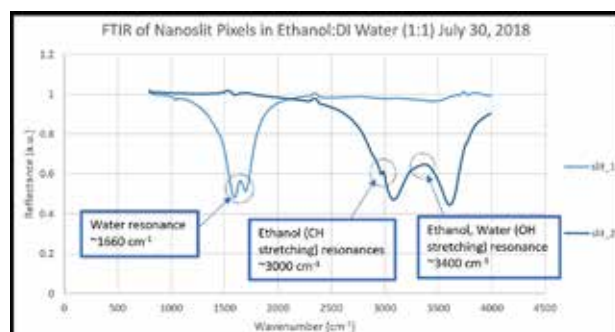


Figure 4: Reflectance spectra for 50 nm wide nanoslits in ethanol-DI water mixture showing water and ethanol resonances.

Site Specific Dual Modification of Native Antibodies Via Microbial Transglutaminase

John Bohn, 2018 KEP Intern

**Chemical and Biomolecular Engineering,
University of Illinois at Urbana-Champaign**

Program: 2018 Keeping the Ezra Promise (KEP) Program

KEP Principal Investigator: Dr. Christopher Alabi, Chemical and Biomolecular Engineering, Cornell University

KEP Mentor: Joshua Walker, Department of Chemical and Biomolecular Engineering, Cornell University

Primary Source of KEP Funding: Keeping the Ezra Promise (KEP), Robert Frederick Smith School of Chemical and Biomolecular Engineering, Cornell University

Contact: johnb2@illinois.edu, caa238@cornell.edu, jaw483@cornell.edu

Website: http://www.cnf.cornell.edu/cnf_2018reu.html

Abstract:

Antibody-drug conjugates (ADCs) are a method of targeted drug delivery. Past research has created ADCs with a drug-to-antibody ratio of two. The aim of this research is to create a bifunctional linker that could attach two chemically distinct compounds twice. The designed linker structures were then attached to a Herceptin antibody, which targets the Her2 receptor, and tested via SDS-PAGE for addition. Results showed that a cross-linker with an ethylenedioxy spacer was the most effective linker. Using FRET, the tetrazine functional group had a rate constant of $31,333 \frac{1}{M \cdot s}$, while the azide functional group did not have a clear rate constant. An MTS toxicity assay showed that the antibody-drug conjugate was more toxic than the free drug. Further studies utilizing more structures with varying PEG lengths are needed to show a strong correlation between structure and conjugation efficiency.

Summary of Research:

Antibodies are naturally occurring proteins that attack specific targets, called antigens. In recent years, these antibodies have been used medicinally as antibody-drug conjugates, in which a linker molecule is attached to the antibody [1]. This allows a drug compound to attach to the linker so that it can be delivered specifically to the desired target. However, traditional antibody-drug conjugates created using the enzyme-modification method use a linker with only one functional group, and therefore can only attach one type of chemical compound [2]. Since most medicinal drug therapies use more than one chemical compound, its usefulness is very limited.

The aim of this research is to address these problems by creating a bifunctional, bioorthogonal linker molecule with tetrazine and azide functional groups. Since both groups can attach drug compounds, the linker allows for two chemically-distinct drug compounds to be attached per linker. Figure 1 presents the synthesis scheme for both linkers, which are distinguished by the spacer between the primary amine and tertiary amide functional groups. This is to test the effect of steric hindrance caused by the tetrazine and azide functional groups.

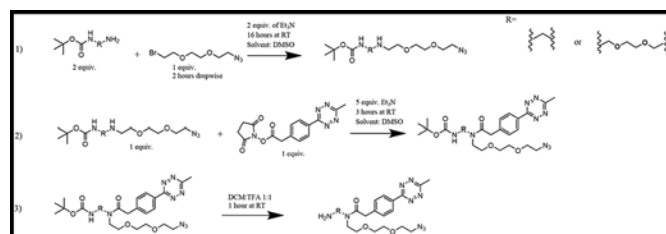


Figure 1: Synthesis scheme for both linker structures.

Once synthesized, the linkers were attached to the Herceptin antibody. This was completed by reacting the antibodies with Peptide:N-glycosidase F, which removes the native glycan at asparagine 297. The antibodies were then reacted with the desired linker and microbial transglutaminase, which attached the linkers to the antibody's conjugation site at glutamine 295.

Figure 2 gives a visual overview of this process.

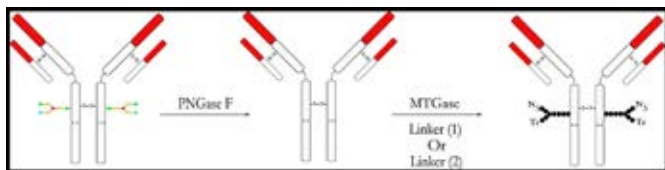


Figure 2: A general overview for the attachment of linkers. After the addition of PNGase F, the native glycan is removed at asparagine 297. The MTGase then attaches the linker to glutamine 295.

For confirmation, the antibody-linker conjugates were placed in an SDS-PAGE gel, which separates the components in solution based on molecular weight. To aid in separation, the antibody-linker conjugates were reacted with two polymers: DBCO- and TCO-modified 5,000 molecular weight polyethyleneglycol (PEG). DBCO-PEG attaches to azide functional groups, while TCO-PEG attaches to tetrazine functional groups. As control groups, two other antibody-linker conjugates were introduced to the gel: one with only an azide functional group, and one with only a tetrazine functional group. When the tags are introduced, only the DBCO will react with the azide linker, and only the TCO will react with the tetrazine linker. Both tags will react with the bifunctional linker, so an even larger shift will be observed, thereby confirming the presence of the bifunctional linker.

The kinetics of the reaction were measured using Förster resonance energy transfer. FRET uses two spectrally matched fluorophores and measures their energy transfer. Carboxyrhodamine-DBCO was used for the azide functional group, while Cy5-TCO was used for the tetrazine functional group. In this experimental setup, carboxyrhodamine-DBCO was initially attached and Cy5-TCO was introduced in solution; measuring the energy transfer allowed for a measurement for the rate of addition. In another experiment, Cy5-TCO was initially attached, and carboxyrhodamine-DBCO was introduced to measure the rate of the DBCO-Azide reaction.

Finally, a toxicity test was conducted using an MTS assay. In this assay, the antibody-drug conjugate was introduced to SKOV7 cells. While incubated at 37°C for a period of four days, the antibody-drug conjugate killed cells. Then, MTS was added, which is broken down in live cell mitochondria to produce formazan, which has an absorbance. By measuring the difference in absorbance between a control solution and the solution with antibody-drug conjugate introduced, the toxicity of the antibody-drug conjugate can be assessed.

Results and Conclusions:

Synthesis of both linkers was successful. However, only the ethylenedioxy linker conjugated to the antibody. Kinetic testing with the tetrazine functional group on the

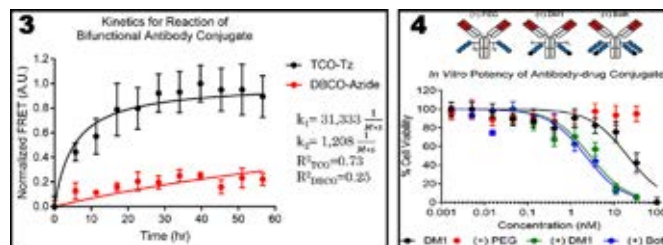


Figure 3, left: Kinetics data for the ethylenedioxy linker. The addition of Cy5-TCO had a rate coefficient of 31,333 $1/(M*s)$, which corresponds to literature values. The addition of carboxyrhodamine-DBCO failed, most likely due to low concentration. Figure 4, right: MTS toxicity assay data. Note that the antibody-drug conjugate was more toxic than the free drug.

ethylenedioxy linker gave a rate constant of 31,333 $\frac{1}{M*s}$, which corresponds to an accepted literature value of $\sim 30,000 \frac{1}{M*s}$ for a linker utilizing only the tetrazine functional group (Figure 3). Finally, the MTS assay showed that the antibody-drug conjugate carrying the drug compound DM1, a maintansine derivative, was more toxic than the free drug in solution. (Figure 4).

Future Work:

While the results show that an effective bifunctional linker can be synthesized and conjugated, further exploration on the effect of structure needs to be completed. Two structures are not comprehensive enough to make strong connections between structure and conjugation efficiency. More structures, with different amounts and locations of PEG spacing, should undergo the tests described above.

Acknowledgements:

I would like to acknowledge the Keeping Ezra's Promise Program and the Robert Frederick Smith School of Chemical and Biomolecular Engineering for funding. I would also like to acknowledge the Alabi Lab for allowing me to research at their facilities this summer.

References:

- [1] Caddick, S.; Chudasama, V.; and Maruani, A. Recent Advances in the Construction of Antibody-Drug Conjugates. *Nature Chemistry*, 2016, 8, pp. 114-119.
- [2] Belmant, Z., et al. Transglutaminase-Based Chemo-Enzymatic Conjugation Approach Yields Homogeneous Antibody-Drug Conjugates. *Biconjugate Chemistry*, 2014, 25, pp. 569-578.

Conjugated Nanoparticle Induced Apoptosis in Cancer Cells

Isabel Castillo, 2018 CNF iREU Intern

Physics, Vassar College

REU Program: 2018 Cornell NanoScale Facility International Research Experience for Undergraduates (CNF iREU) Program at the National Institute of Material Science (NIMS), Tsukuba, Ibaraki, Japan

CNF iREU Principal Investigator: Dr. Jun Nakanishi, NIMS

CNF iREU Mentor: Dr. Shota Yamamoto, Mechanobiology Group, NIMS

Primary Source of CNF iREU Funding: National Science Foundation under Grant No. OISE-1559368

Contact: gicastillopedra@vassar.edu, nakanishi.jun@nims.go.jp, yamamoto.shota@nims.go.jp

Website: http://www.cnf.cornell.edu/cnf_2018reu.html

Abstract:

The activity of cells is highly dependent on their extracellular environments composed of soluble factors, surrounding cells and extracellular matrices (ECMs). These extracellular stimuli activate intracellular machinery called signal transduction, which directs the cells to a specific phenotype. The purpose of this project was to develop new materials to chemically and mechanically engineer cellular environments and look at their impact on cellular activities using a nanobiointerface and nanomaterial synthesis and characterization.

Summary of Research:

X polymer was conjugated with a Y nanoparticle in an effort to induce apoptosis in cancer cells of Z cancer type. Preparation of the conjugated particle included steps to wash the particle and obtain an adequate size before inserting the conjugated particle in the cancer cell. Obtaining an adequate size involved putting the functionalized nanoparticle through several cycles of ultra-centrifuge utilizing an adequate solvent that mimicked the natural body environment that Z cancer cells are found in. The ultra-centrifuge process allowed for an effective particle size, and sufficient collection of functionalized nanoparticle concentration.

Particle concentration was confirmed utilizing a spectrometer. A comparison sample's concentration utilizing the manufacture's information was utilized to determine if the concentration collected was enough to perform cellular experiments. Sufficient concentration allowed for the testing protocol to determine if the polymer in question was binding to the correct site of the Z cancer cell.

Additionally, Western Blotting was followed to analyze the phosphorylation levels of the Z cancer cells after insertion of the functionalized nanoparticle.

The beforehand procedures allowed for fruitful results for further cellular experiments to include apoptosis.

In preparation for the apoptosis experiment, the protocol for Annexin V was followed. In addition of apoptosis testing, necrosis was also tested for utilizing PI. A control group and a group with the soluble polymer was also prepared for comparison purposes with our sample.

Results and Conclusions:

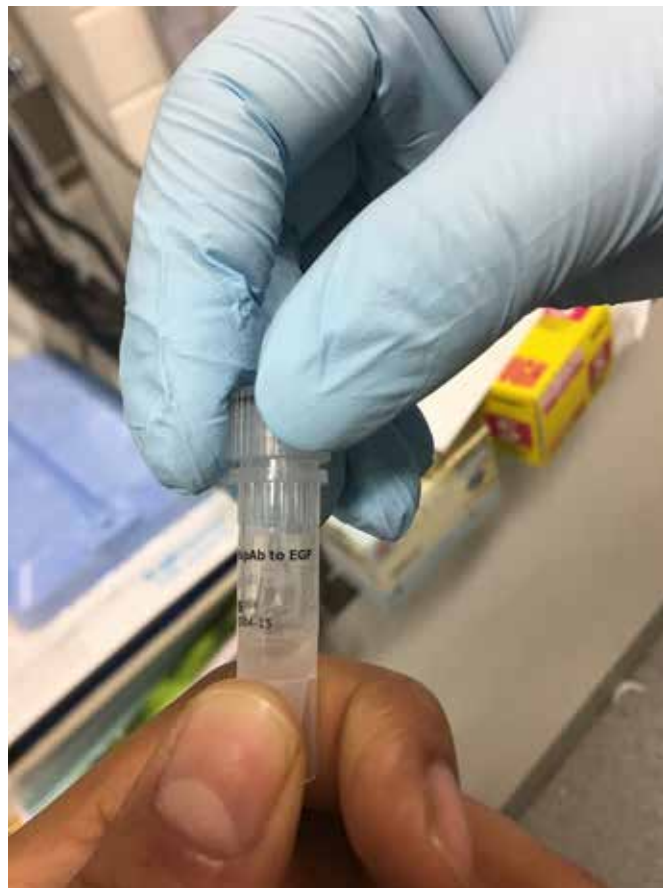
Putting the conjugated nanoparticles through an ultra-centrifuge procedure proved to be an effective method to separate the functionalized particles from the non-functionalized particles. The spectrometer revealed a sufficient enough concentration to performed the cellular experiments. Thus, confirming that the set ultra-centrifuge parameters were adequate and efficient. The phosphorylation levels obtained contradicted prior results and expectations, therefore, further analysis of the polymer concentration on the nanoparticle needs to be performed. The Annexin V protein group was successful in the determination of apoptosis. The PI group allowed for the analysis of necrosis in the Z cancer cells. The apoptosis and necrosis levels observed were promising thus fortifying the need to continue studies to understand the mechanisms in play during the apoptotic and necrotic stage.

Future Work:

Further work needs to be performed to determine if the material we used is the most efficient and durable. Additionally, the size of the functionalized nanoparticle has been revised to explore the possibility of other sizes being more efficient at inducing apoptosis or necrosis. Lastly, further work is needed to understand the biological and physical mechanism from the moment of insertion to the apoptotic stage as many unknowns remain.

Acknowledgements:

Dr. Jun Nakanishi, Dr. Shota Yamamoto, Dr. Lynn Rathbun, All NIMS staff and members, NNCI, NSF (Grant # OISE-1559368) and Cornell University.



Isabel works on her project in the lab at NIMS.



The 2018 iREU Interns with Program Creator and Coordinator, Dr. Lynn Rathbun; Mr. Jace Waybright, Mr. Carl Felstiner, Ms. Paola Perez, Mr. Peter Chang, Ms. Gina Isabel Castillo, Mr. Daniel Teal, Dr. Rathbun

Understanding the Structure of Germanium Sulfide (GeS)

Miguel Castro-Rivera, 2018 PARADIM REU Intern

Mechanical Engineering, Inter-American University of Puerto Rico, Bayamon Campus

REU Program: 2018 Platform for the Accelerated Realization, Analysis and Discovery of Interface Materials
Research Experience for Undergraduates (PARADIM REU) Program

PARADIM REU Principal Investigator: Prof. Darrell Schlom, Materials Science and Engineering, Cornell University

PARADIM REU Mentor: Dr. Betül Pamuk, Department of Applied and Engineering Physics, Cornell University

Primary Source of PARADIM REU Funding: Support for PARADIM is provided under NSF Grant # DMR-1539918
as part of the Materials Innovation Platform Program

Contact: mcastro1222@interbayamon.edu, schlom@cornell.edu, betul.pamuk@cornell.edu

Websites: <http://paradim.cornell.edu/education>, http://www.cnf.cornell.edu/cnf_2018reu.html

Abstract:

The purpose of this project was to manipulate GeS band gap by applying bi-axial strain to the material with the goal of optimizing the gap. To complete this process, we used computational methods with density functional theory (DFT). We obtained an indirect band gap $E_g = 0.78$ eV, almost half of the experimental result. When the structure was strained, the gap remained indirect and increased to 0.87 eV for 5% tensile, while for 5% compressive, the gap closed completely. However, an interesting behavior was observed between 0% and 2% tensile, the conduction band minimum (CBM) changed from being at Γ , to a point in between $\Gamma \rightarrow X$ path.

Introduction:

Finding an alternative sustainable source of energy has turned into one of the most important quests for humanity. Out of the many different sources, solar power is one that shows a lot of promise. Energy from the sun has the potential of supplying the planet energy demand of 363 terawatt hours per day in a matter of seconds, but this is limited due to the high cost of silicon-based photovoltaics (PVs) and their low conversion efficiency (e.g. $\sim 31\%$) [1]. One key aspect to improving the efficiency of PVs lies in the capture and conversion of the energy obtained from solar photons. Because photons with energy lower to the band gap of the material are not absorbed, and those with higher energy release heat due to electron relaxation through the bands, it is essential that any PV material has a band gap close to the optimal absorption value, e.g. ~ 1.3 eV [2]. A potential substitute for Si-based PVs is GeS, due to its abundance and non-toxic properties [3]. One complication remains, GeS has a ~ 1.74 eV gap [4]. Therefore, using density function theory (DFT), we decided to alter GeS to obtain a more ideal band gap.

Methods:

We used a projector augmented wave pseudopotentials method with an electronic energy convergence of 10^{-8} eV

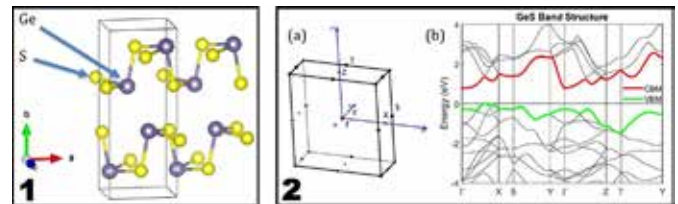


Figure 1, left: Orthorhombic GeS structure. Figure 2, right: (a) BZ path used from [9]. (b) Band results. Conduction band minimum (CBM). Valence band maximum (VBM).

and a force tolerance of 10^{-3} eV/Å [5], which are included in the VASP package [6,7]. We implemented the parametrization scheme of Perdew-Burke-Ernzerhof for solids (PBEsol) with the generalized gradient approximation (GGA) for the exchange and correlation functional within DFT. After loading the structure into VASP, we used a converged value of 650 eV for energy cutoff and an electronic momentum mesh of size $12 \times 6 \times 12$ for the sampling of the Brillouin Zone (BZ). GeS has a layered crystal structure containing eight atoms in the primitive unit cell. The initial parameters used for GeS are from [8]. After relaxing the crystal structure, the ground state parameters were the following: $a = 4.14$ Å, $b = 10.35$ Å and $c = 3.67$ Å. The crystal structure representation of GeS, the band structure and BZ can be seen in Figure 1 and 2 respectively.

Using DFT, we started to strain GeS bi-axially ($\pm 5\%$, 1% step) by changing and fixing lattice parameters “a” and “c” simultaneously to their respective new values. A visual representation is shown in Figure 3 (a) and (b).

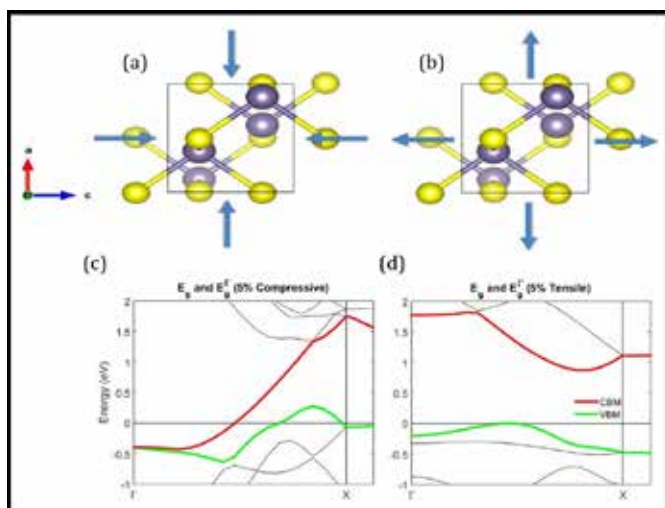


Figure 3: (a) Compressive bi-axial strain. (b) Tensile bi-axial strain. (c) Closing of the gap at 5% compressive strain. (d) $E_g = 0.87$ eV and $E_g^\Gamma = 1.98$ eV at 5% tensile strain.

Results and Conclusions:

We analyzed the fundamental indirect gap of $E_g = 0.78$ eV between valence band maximum (VBM) $^\gamma$ in the $\Gamma \rightarrow X$ direction and CBM at Γ . We also observed a direct gap $E_g^\Gamma = 1.06$ eV at Γ symmetry point. This was due to how close both gaps are in value, and also because a direct gap has less energy loss than an indirect gap. As it is shown in Figure 3 (c), we found that when we applied 5% compressive strain, both E_g and E_g^Γ became zero because the valence and conduction band intersected one another. When it was 5% tensile strained (Figure 3 (d)), both gaps increased, $E_g = 0.87$ eV and $E_g^\Gamma = 1.98$ eV, unfortunately making E_g^Γ too big to remain a competing gap. Also, Figure 4 shows how E_g and E_g^Γ

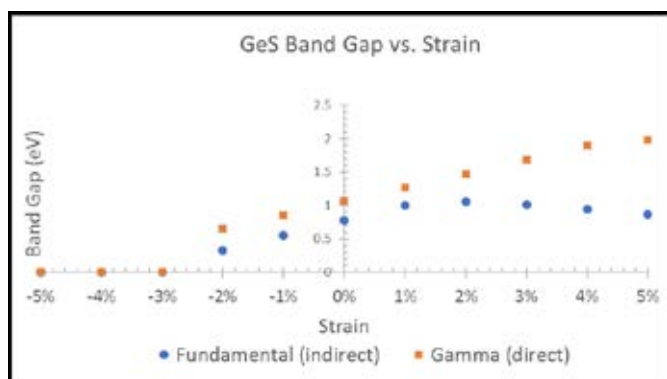


Figure 4: Summary of E_g and E_g^Γ band gap results.

behaved with different strain values. The unstrained result under-estimated the experimental value of 1.74 eV [4]. This indicates some issues in the approximating methods. However, we observed that with tensile strain, CBM changed from Γ point to a position in between the Γ and X path. This opens the possibility of E_g changing from indirect to a direct gap at some point in between.

Future Work:

We will improve the modeling methods to obtain a better match to the experimental gap and decrease the strain step-size to 0.2% around the transition phase between 1% and 2% tensile strain with the hopes of observing a direct gap.

Acknowledgements:

Support for PARADIM is provided under DMR-1539918 as part of the NSF Materials Innovation Platform Program. Calculations performed at Tardis computer cluster at Cornell University Center for Advanced Computing (CAC), with access given by Prof. Fennie. Special thanks to the PARADIM and CNF staff, and my fellow PARADIM interns.

References:

- [1] N. S. Lewis, Science 315, 798 (2007).
- [2] L. Zhu, T., et. al, Opt. Express 24, A740 (2016).
- [3] P. D. Antunez, et. al, Nanoscale 3, 2399 (2011).
- [4] D. D. Vaughn, et. al, J. Am. Chem. Soc. 132, 15170 (2010).
- [5] J. P. Perdew, et. al, Phys. Rev. Lett. 100, 136406 (2008).
- [6] G. Kresse and D. Joubert, Phys. Rev. B 59, 1758 (1999).
- [7] G. Kresse and J. Hafner, Phys. Rev. B 47, 558 (1993).
- [8] J. M. Skelton, et. al, J. Phys. Chem. C 121, 6446 (2017).
- [9] L. Makinistian and E. A. Albanesi, Phys. Rev. B 74, 045206 (2006).

Investigation of Intrinsic Defects in Sputtered Titanium Oxide Surfaces

Peter Chang, 2018 CNF iREU Intern

Physics, University of Dallas

REU Program: 2018 Cornell NanoScale Facility International Research Experience for Undergraduates (CNF iREU) Program at the National Institute of Material Science (NIMS), Tsukuba, Ibaraki, Japan

CNF iREU Principal Investigators: Dr. Takeo Ohsawa, Dr. Naoki Ohashi, NIMS

CNF iREU Mentor: Dr. Takeo Ohsawa, NIMS

Primary Source of CNF iREU Funding: National Science Foundation under Grant No. OISE-1559368

Contact: pchang@udallas.edu, ohashi.naoki@nims.go.jp, ohsawa.takeo@nims.go.jp

Website: http://www.cnf.cornell.edu/cnf_2018reu.html

Abstract:

The discovery of a quasi-two-dimensional electron liquid (q2DEL) formed at metal-oxide surfaces has motivated research with applications towards next generation oxide electronics. The preparation of well-defined surfaces is important for generating these interesting electronic states. However, unintentional defects and their roles in determining surface properties remain an area of debate. Near surface oxygen vacancies have long been held responsible for reduced surface defects in titanium oxides (TiO_2). However, many previous experimental results have highlighted the persistence of reduced states in sputtered TiO_2 even after surface vacancies were removed, thereby indicating that the intrinsic nature of these surfaces is still controversial. Consequently, further investigation of intrinsic defects in TiO_2 surfaces is still needed. In this study, we present rutile TiO_2 as a model oxide. Surface defects in niobium-doped TiO_2 single crystals with different crystal orientations are monitored using x-ray and ultraviolet photoelectron spectroscopy (XPS/UPS) as a function of Ar^+ exposure and annealing temperature. In agreement with previous studies, XPS spectra show an increase with sputtering time in reduced Ti^{3+} and Ti^{2+} surface states in addition to the standard Ti^{4+} state. These reduced peaks are removed and surface stoichiometry is restored under annealing at only 300°C and 400°C for $\text{Nb}:\text{TiO}_2$ $\langle 110 \rangle$ and $\langle 001 \rangle$, respectively, suggesting a bulk-assisted re-oxidation. These results indicate that interstitial titanium and not oxygen anions are the primary movers for re-oxidizing reduced TiO_2 at relatively low temperatures.

Introduction:

Due to its high dielectric constant, titanium oxide (TiO_2) has been proposed as a potential replacement for silicon dioxide as a gate insulator material [1]. This idea has received increased attention with the discovery of a quasi-two-dimensional electron liquid (q2DEL) that exists at metal-oxide surfaces, resulting in a number of useful properties applicable towards the development of oxide electronics [2].

These surface states are responsible for defects that result from doping electrons into TiO_2 . These excess electrons are observed through reduced states of Ti which normally has a charge of plus four in pristine TiO_2 . Photoelectron spectroscopy is best suited to detect reduced surface states, since the binding energy of electrons ejected through the photoelectric effect carries information about the element, electron orbital and chemical environment. Reduced states in TiO_2 show up via a chemical shifting of the Ti $2p$ peak and through the rise of the Ti $3d$ peak inside the band gap.

In order to generate these electronic states, it is necessary to form well-defined surfaces obtained through ion

radiation and subsequent annealing. However, this process induces intrinsic defects into TiO_2 that must be taken into account if using XPS to study the q2DEL states.

Near surface oxygen vacancies have long been held responsible for intrinsic defects in TiO_2 . However, past experimental results have shown the persistence of reduced surface states even after oxygen vacancies were removed through oxygen exposure. In this study, we further clarify the properties of intrinsic defects in TiO_2 by monitoring their amount as a function of Ar^+ radiation, annealing temperature and crystal orientation.

Experimental Procedure:

Rutile niobium-doped TiO_2 ($\text{Nb}:\text{TiO}_2$) samples with $\langle 001 \rangle$, $\langle 100 \rangle$, $\langle 110 \rangle$ and $\langle 111 \rangle$ crystal planes were sputtered with Ar^+ for thirty seconds, one minute, two minutes and three minutes. The Ti $2p$, O $1s$ and valence band photoelectron peaks were observed using Al $K\alpha$ X-ray. Defect ratios in the Ti $2p$ peaks and the area under the Ti $3d$ peaks were used to quantify the amount

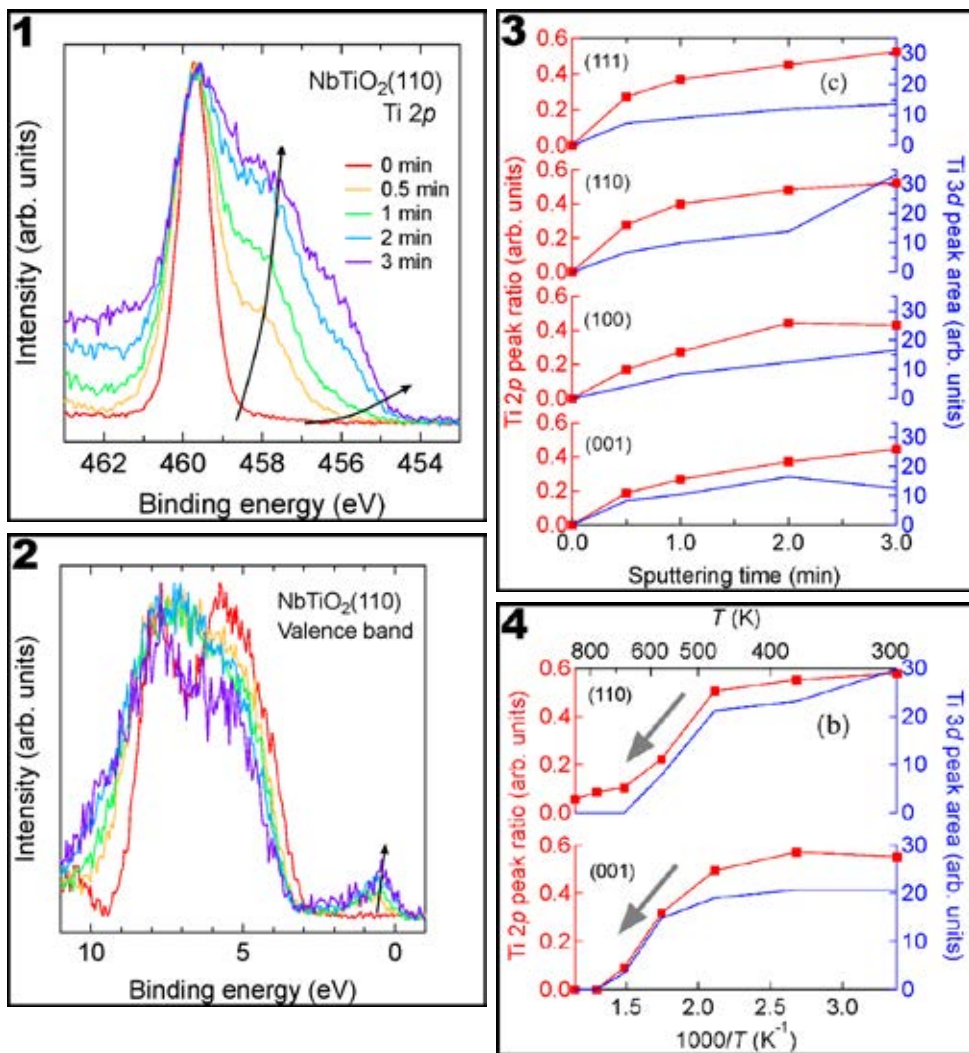


Figure 1, top left: XPS Ti 2p scans of Nb:TiO₂ <110> surface under increasing Ar⁺ sputtering time. Figure 2, bottom left: XPS valence band scans of Nb:TiO₂ <110> surface under increasing Ar⁺ sputtering time. Figure 3, top right: Defect ratios in Ti 2p spectra and Ti 3d peak area plotted as a function of sputtering time. Figure 4, bottom right: Defect ratios in Ti 2p spectra and Ti 3d peak area plotted as a function of annealing temperature after sputtering time for three minutes.

of surface defects, and surface stoichiometry was determined by calculating the titanium to oxygen ratio.

Temperature dependence of the reduced surface states was investigated using Nb:TiO₂ <110> and <001> by first sputtering the sample for three minutes. XPS scans of the Ti 2p and 3d peaks were then conducted at 100°C intervals ranging from 25°C to 600°C.

Results and Discussion:

Figures 1-3 show how XPS spectra change with Ar⁺ sputtering time. Reduced states were evident through the Ti 3d peak inside the bandgap and in the Ti 2p scan through two shifted photoelectron peaks corresponding to Ti³⁺ and Ti²⁺. Defects increased with sputtering time and titanium to oxygen ratio decreased indicating that defect generation was accompanied by the formation of oxygen vacancies.

Figure 4 shows the temperature dependence of surface defects for the <110> and <001> crystal planes. Reduced states disappeared and surface stoichiometry was recovered under annealing at relatively low temperatures with 300°C for <110> and 400°C for <001>. These results suggested that interstitial titanium, which is mobile at lower temperatures, and not oxygen anions, is the primary mover at lower temperatures, migrating from the surface into the bulk.

The temperature experiments suggested that in addition to oxygen vacancies, interstitial titanium also contributes largely to reduced surface states in TiO₂. This is indicated by the significant decrease of defects observed under XPS as titanium cations migrated into the bulk.

Future Work:

Future experiments can study why the formation of doubly reduced Ti²⁺ states under Ar⁺ sputtering were more prone to occur in the <110> and <111> crystal planes. Additional studies can also investigate why surface

defects disappeared at different temperatures for <001> and <110>.

Acknowledgements:

I would like to thank my PI Dr. Naoki Ohashi and my mentor Dr. Takeo Ohsawa, as well as Dr. Lynn Rathbun and Dr. Nancy Healy for organizing this program. I would also like to acknowledge NNCI, NIMS and NSF who funded this program under award OISE-1559368.

References:

- [1] U. Diebold, et al., Surface Science Reports 48, 53 (2003).
- [2] R. Yukawa, et al., Physical Review B 97, 165428 (2018).
- [3] S. Wendt, et al., Science 320, 1755 (2010).

STEM Imaging and Composition Mapping of Multiferroic Oxides

Mr. Anthony Coleman, 2018 PARADIM REU Intern

Physics Engineering, Chicago State University

*REU Program: 2018 Platform for the Accelerated Realization, Analysis, and Discovery of Interface Materials
Research Experience for Undergraduates (PARADIM REU) Program*

PARADIM REU Principal Investigator: Professor Darrell Schlom, PARADIM, Cornell University

PARADIM REU Mentor: Dr. Megan Holtz, PARADIM, Cornell University

*Primary Source of PARADIM REU Funding: Support for PARADIM is provided under NSF Grant # DMR-1539918
as part of the Materials Innovation Platform Program*

Contact: schlom@cornell.edu, meh282@cornell.edu

Websites: <http://paradim.cornell.edu/education>, http://www.cnf.cornell.edu/cnf_2018reu.html

Abstract:

Multiferroic materials are fast becoming materials that are being observed as thought-provoking materials with the potentials for the next generation of data storage technologies. Although there are a few ferroic orders, we will be specifically experimenting with the coupling of the electric and magnetic order. The realization of these multiferroic materials to be operative in room temperature are few, and even more are limited with robust, coupled magnetization and polarization. Molecular beam epitaxy with oxides (MBE), is an auspicious methodology to grow, and or produce, these materials. This procedure is very promising in the production of new innovative growth recipes of properties coupled in materials, through heterostructures and interface stages. In this investigation, ferroelectric LuFeO_3 with the ferrimagnetic CoFe_2O_4 was combined, creating superlattice layers. The purpose was to advance a material with polarization and magnetization, impulsive in nature, that contains the functioning, desired properties above room temperatures. The obtaining of the characteristics of the superlattice layers on the atomic scale, is vital in this research. After the Growth of the multiferroic oxide, scanning transmission electron microscopy (STEM), was used alone with the composition mapping, using x-ray energy dispersive spectroscopy (EDS) and electron energy-loss spectroscopy (EELS). The STEM scanning and composition mapping of the material commenced. The investigation of interdiffusion between materials was the investigations purpose. We proceeded with the mapping of the elemental profiles through the film and across the bottom electrode. The inspection for the interdiffusion and growth conditions was completed and provided critical advice for the molecular beam epitaxy growth procedure following this research.

Summary of Research:

The purpose of this research was to obtain new materials with the new coupled properties, magnetization and electrical polarization at room temperature. These new properties specifically would have very useful applications for next-generation memory devices in computer and sensors. For example, a new memory element that has four bits instead of two, using both the magnetic and electronic degrees of freedom, would be groundbreaking. Additionally, the control of magnetic memory by applying a voltage would make data storage more energy efficient. To develop this material, the electric field must govern the magnetism. Although multiferroic materials have been observed previously, the polarization or magnetism were only observed in well below room temperatures conditions, or properties of the magnetism were weak.

To generate such useful new properties, the heterostructures or interfaces must be grown. These materials required a STEM scanning and a composition mapping examination of the materials, on the atomic scale. The multiferroic oxide we intend to create is ferroelectric lutetium ferrite (LuFeO_3), and ferromagnetic cobalt ferrite (CoFe_2O_4). Ferroic materials have a long-range ordering of a macroscopic property due to the lattice structure. This long-range ordering, or the crystal atomic position, is also known as translational periodicity. When the

location of an atom and its neighbors are identified by STEM, the polarization of each atom is known exactly throughout the crystal structure.

The design of this new material began with using molecular beam epitaxy (MBE). The growth of this superlattice was done on a substrate of yttria-stabilized zirconia (YSZ), with the electrode layer made from the element iridium. The superlattice elements of 20 layers of LuFeO_3 and 10 layers of CoFe_2O_4 were repeated to form the superlattice (see Figure 1). The superlattice was grown in this alternating pattern, combining ferroelectric LuFeO_3 and ferromagnetic CoFe_2O_4 to achieve the material to exhibit simultaneous orders in the ground state of each electric and magnetic properties.

The substrate YSZ is very insulating and a direct current across the thin film is desired, however, the YSZ (substrate) prohibits traditional ferroelectric testing. The iridium electrode should allow the ferroelectric testing needed, due to it being a conductive material (see Figure 1). We used elemental mapping to determine if there is interdiffusion between the superlattice layers or in the iridium electrode (See Figures 2 and 3). This composition mapping will help in the growth methods using MBE, by means of the data collected from the investigation of interdiffusion between layers.

We used focused ion beam (FIB) lift out to remove a portion of the material for atomic resolution imaging with STEM. The FIB was used to lift out the sample by using a 30kV gallium ion beam to cut out a sample. It was then attached to a TEM grid and thinned with a 5kV and 2kV milling steps to reduce surface damage down to the desired size of 20-50 nm. We then loaded the sample into the TEM. Electrons were then accelerated through the sample measuring the elastic scattered high angles produced to be measured on the Annular dark field detector, for Z contrast images (see Figure 2). For the composition mapping, we used EDS (x-ray energy dispersive spectroscopy). The power of this mapping was to identify each element binding energy, providing elemental identification due to each elements being bound at different strengths. This would provide a fingerprint of each element producing images to locate any interdiffusion.

More composition mapping was done using EELS (electron energy loss spectroscopy). This detector of the TEM, measured the scattered electron that lost energy giving us chemical information on each element, producing more images to detect if interdiffusion was present. (see Figure 3).

Results and Conclusions:

No interdiffusion in between the LuFeO_3 and the CoFe_2O_4 appeared to be present in the EDS images. EDS is not good for light elements but good for heavy detection. The absence of interdiffusion of the LuFeO_3 and the CoFe_2O_4 was due to the lower growth temperature of the CoFe_2O_4 (~ 400°C, compared to 900°C for previous growths).

A background signal in iridium that was noticed was concluded as an artifact of multiple scattering in the heavy, dense, iridium electrode layer, which was confirmed in EELS. We found that cobalt does not diffuse into LuFeO_3 when the CoFe_2O_4 is grown at low temperature.

No interdiffusion in between the superlattice layers, or into the iridium electrode was present in the EELS mapping. Also, the EELS showed no Fe, Co or O diffusing into the iridium layer.

Future Work:

Future growth on iridium electrodes should not try to compensate for interdiffusion into the electrode. From the STEM scanning and composition mapping performed by EDS and EELS on the multiferroic materials lutetium ferrite and cobalt ferrite, we obtained information to assist in developing better growth methods using oxide MBE. Further research and other characterizations shall be performed. The material looks promising.

Acknowledgments:

I would like to thank my PI, Professor Darrell Schlom, and the PARADIM group, my mentor Dr. Megan Holtz for her expertise, time, and dedication she gave to the research. I would also like to thank John Grazul and David Muller at the microscopy facilities at CCMR, Dr. Julia Nucci and REU staff, Cornell University, my lab partner Iryna Glushchenko, and the NSF for funding under grant DMR-1539918 as part of the Materials Innovation Platform Program.

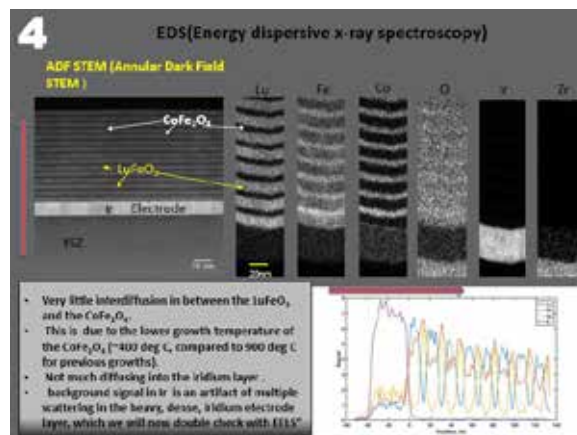
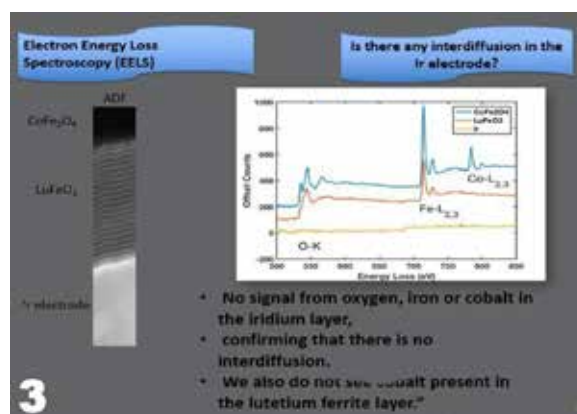
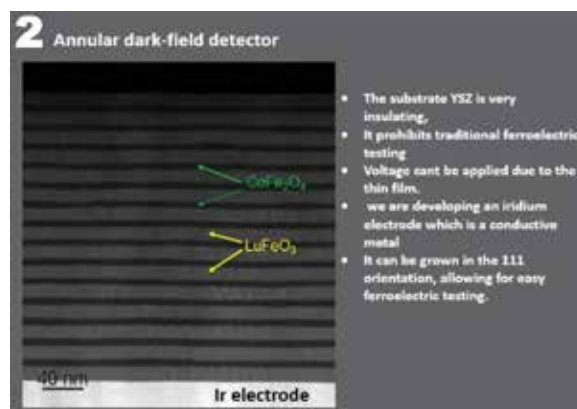


Figure 1, top: Superlattice growth. Figure 2, upper middle: STEM image. Figure 3, lower middle: EELS image. Figure 4, bottom: EDS image.

Implementing a Functional ARPES System

Stephanie Eberly, 2018 PARADIM REU Intern

Mechanical Engineering, North Carolina State University

REU Program: 2018 Platform for the Accelerated Realization, Analysis, and Discovery of Interface Materials Research Experience for Undergraduates (PARADIM REU) Program

PARADIM REU Principal Investigator: Dr. Darrell Schlom, Material Science and Engineering, Cornell University

PARADIM REU Mentors: Dr. Luca Moreschini and Dr. Edward Lochocki, MSE, Cornell University

Primary Source of PARADIM REU Funding: Support for PARADIM is provided under NSF Grant # DMR-1539918 as part of the Materials Innovation Platform Program

Contact: sgeberly@ncsu.edu, schlom@cornell.edu, lmoreschini@cornell.edu, el432@cornell.edu

Websites: <http://paradim.cornell.edu/education>, http://www.cnf.cornell.edu/cnf_2018reu.html

Abstract:

Over the past decades, angle-resolved photoemission spectroscopy, or ARPES, has become a leading characterization tool in condensed matter physics. ARPES is an extremely valuable method for probing and mapping out the electronic structure of crystalline materials. The Platform for Accelerated Realization, Analysis, and Discovery of Interface Materials, or PARADIM, is currently in the process of designing and procuring a new ARPES system. The challenge of this design is due to the nature of the technology which requires that all procedures and measurements within the system are performed under ultra-high vacuum (UHV) conditions. Our goal was to design and build a load lock and sample storage roundhouse within the UHV system for inserting and storing samples. These two components are critical for the operation of the new ARPES setup.

Summary of Project:

ARPES supplies vital information on the physics behind unique electronic and optical properties of materials through creating an image of the momentum-resolved electronic structure. ARPES has proven to be an essential tool in recent efforts to understand novel materials, whether fitting to one-electron band descriptions, such as topological insulators [1], or more complex correlated systems, which are challenging to predict with band theory and better described by a many-body picture [2]. The technology works through exploiting the basic principle of photoemission to eject electrons from the top atomic layers of a material. These photoemitted electrons pass through an electron analyzer and eventually reaching a 2D detector and camera. This process provides the emission angle and kinetic energy of the electron. Taking these two quantities, the binding energy and momentum of the electron prior to its photoexcitation can easily be extracted and the electronic band structure mapped [1].

The novel ARPES system being commissioned is part of a user facility that will be utilized by researchers across the globe. Consequently, it is imperative that the design is functional, robust, and intuitive. Figure 1 illustrates the anticipated arrangement of the lab. The molecular beam epitaxy (MBE) presently exists and is functional, whereas the ARPES system is fully designed but only partially installed. Figure 2 depicts the current state in mounting the new ARPES. MBE and ARPES are frequently used in conjunction with one another, therefore it is necessary that they communicate within UHV through a

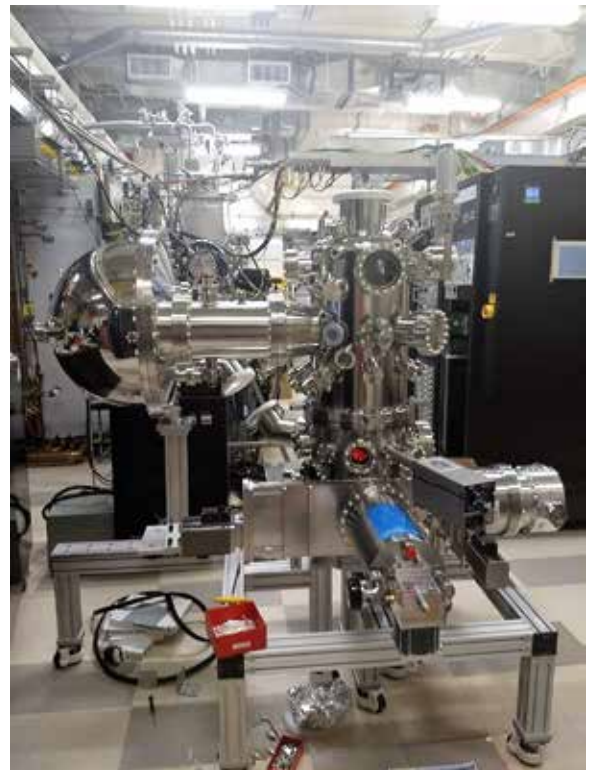


Figure 1: Image of the current state of new ARPES setup.

transfer system. The next step in commissioning the new setup is to design and build a load lock and sample storage roundhouse off of this transfer system.

Load Lock Design. Electrons cannot travel through air at atmospheric pressure, therefore photoemission requires vacuum. For assuring a reasonable stability of the sample surface, ARPES measurements are typically performed at a pressure $< 10^{-10}$ torr. The load lock, whose design is shown in Figure 3, permits users to insert and remove samples without venting the entire apparatus. It operates through a sample being inserted into the sample garage, the chamber pumping down, and then the gate valve opening. Once the gate valve is open, the sample garage travels upwards to meet a second transfer arm that picks up and pushes the sample into the main chamber to be measured. The sample garage is cut out of aluminum with a stainless steel leaf spring to secure the samples in place. The garage's capacity is six samples which maximizes the number of samples for the given length. Key features of the overall design include that the garage motion is easily motorized, it requires primarily stock parts, and the operation is simple and user friendly.

Sample Storage Design. Samples exposed to air can rarely be successfully measured by ARPES, thus it is critical they are stored within the UHV system after growth. The sample storage roundhouse serves as a long-term holding cell to protect samples if they are not immediately measured after growth in the MBE or if they need to be analyzed again later. The design, exhibited in Figure 4, consists of three sample carousel disks mechanically coupled to a solid aluminum pole. Each carousel layer holds eight samples, resulting in a total system capacity of twenty-four samples. However, extra mounting holes in the center pole allow additional sample carousel layers to be added as needed to increase storage capacity. The sample carousel is approximately 3.5 inches in diameter and placed within a 4-inch

diameter chamber. Similar to the load lock garage, the sample carousel employs thin stainless-steel leaf springs to clamp in samples and the carousel body will be waterjet cut out of aluminum. Three viewing ports are located at different angles and positions on the sample system chamber to maximize visibility of the transfer of samples into the storage carousels. Lastly, there is a gate valve that can be shut to isolate the system from the main measurement chamber in case of a leak or required maintenance.

Present Status and Future Directions:

The load lock garage has been machined, assembled, and is currently undergoing testing. Next, the stock pieces of the design will be ordered and then the assembled load lock will be attached onto the main chamber. The sample storage design is presently in the process of fine-tuning and optimization. After the final design is approved, it will follow a similar process to the load lock where custom parts are machined, and stock parts are acquired. Once both the load lock and sample storage are attached onto the ARPES system they will be tested and refined.

Acknowledgements:

A huge thank you to Luca and Ed for serving as amazing mentors. Thank you also to Dr. Darrell Schlom, Dr. Julie Nucci, and PARADIM. Lastly, thank you for our NSF funding provided by grant DMR-1539918.

References:

- [1] M. Z. Hasan and C. L. Kane, "Colloquium: Topological Insulators", *Rev. Mod. Phys.* 82, 3045 (2010).
- [2] A. Damascelli, Z. Hussain and Z.-X. Shen, "Angle-resolved photoemission studies of the cuprate superconductors", *Rev. Mod. Phys.* 75, 473 (2003).

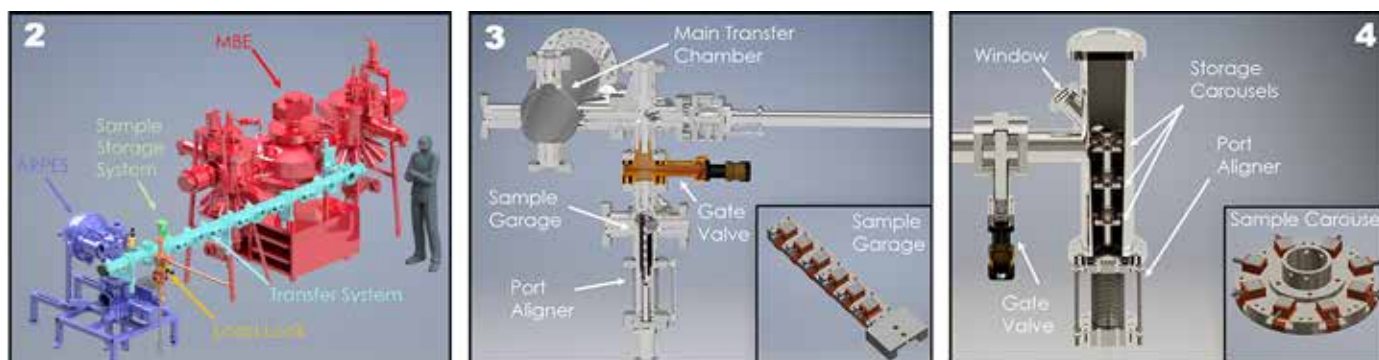


Figure 2, left: 3D AutoCAD model depicting the ARPES/MBE system. Figure 3, middle: AutoCAD model of the load lock. Figure 4, right: AutoCAD model of the sample storage.

Wetting Layer Engineering for GaSb Quantum Dots

Carl Felstiner, 2018 CNF iREU Intern

Physics, Mathematics, Whitman College

REU Program: 2018 Cornell NanoScale Facility International Research Experience for Undergraduates (CNF iREU) Program at the National Institute of Material Science (NIMS), Tsukuba, Ibaraki, Japan

CNF iREU Principal Investigator & Mentor: Dr. Takeshi Noda, Photovoltaic Materials Group, NIMS

Primary Source of CNF iREU Funding: National Science Foundation under Grant No. OISE-1559368

Contact: carlfelstiner@gmail.com, noda.takeshi@nims.go.jp

Website: http://www.cnf.cornell.edu/cnf_2018reu.html

Abstract:

Quantum dot intermediate band solar cells have the ability to absorb photons at three different wavelengths instead of just one, allowing them to surpass the Shockley-Queisser efficiency limit of 30% to a maximum theoretical efficiency of 63%. In depositing the quantum dots in the S-K growth mode, we used two different materials, indium arsenide (InAs) and gallium antimonide (GaSb), for the wetting layer to grow GaSb quantum dots. The change in wetting layer largely affected quantum dot geometry and optical properties. When fabricating solar cells, devices with the InAs wetting layer performed better than those with the GaSb wetting layer, suggesting that the InAs wetting layer allows for enhanced thermal excitation in the transition from the intermediate band to the conduction band.

Introduction:

Single band gap solar cells can only absorb photons at one energy level and have theoretical efficiency limit of 30% [1]. By introducing an intermediate band between the conduction and valence bands, solar cells can absorb photons to excite electrons at three different energy levels, allowing them to absorb sub-bandgap photons that were previously transmitted for a theoretical efficiency maximum of 63% [2]. One implementation of the intermediate band is through the usage of very small particles called quantum dots (QDs) [3-6]. QDs experience quantum confinement in all three dimensions, so they have discrete energy levels and can behave like quantum wells [7]. This allows for the intermediate band to be implemented in two different types of band structures as shown in Figure 1. We used GaSb QDs

grown on GaAs because studies have shown that those materials form a type II structure where only the holes are confined, leading to less recombination [5,6].

We deposited QDs using the Stranski-Krastanov growth method, where a thin material called the wetting layer was first deposited onto GaAs. The slightly larger lattice constant of the wetting layer (0.6 nm) than the bulk GaAs (0.56 nm) leads to a compressive strain, and once 2-3 monolayers are deposited onto the sample, quantum dots begin to form [8,9]. The wetting layer is confined in one dimension and has a step function-like density of states, leading to a continuum above the ground state energy. It assists in the transition from the intermediate to the conduction band by thermal excitations. In this project, we studied the role of the wetting layer in the formation of different QD geometries and their effects on the performance of solar cell devices.

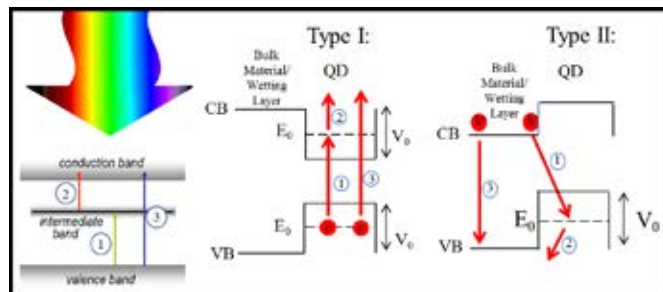


Figure 1: The three different photon excitations in the intermediate band solar cell and the corresponding types of band alignments.

Experimental Methods:

We experimented with two different device structures. The first was a device with a 2.5 ML GaSb QD layer on top of a 1 ML GaSb wetting layer, and the other consisted of 2.5 ML GaSb deposited on a 1 ML InAs wetting layer. Both materials had almost equal lattice constants. We employed molecular beam epitaxy (MBE) to deposit smooth films of bulk GaAs before depositing our QD

and wetting layers, and confirmed the deposition of our nanostructures using reflection high-energy electron diffraction (RHEED).

For solar cell device fabrication, we deposited 10 layers of the QD/wetting layer/GaAs structures on top of n-type GaAs. We then deposited n-type GaAs on top. For structural and optical characterizations, we used atomic force microscopy (AFM) and photoluminescence (PL) spectroscopy at 10K. IV characterizations to measure solar cell device performance were performed using a solar simulator at AM1.5G.

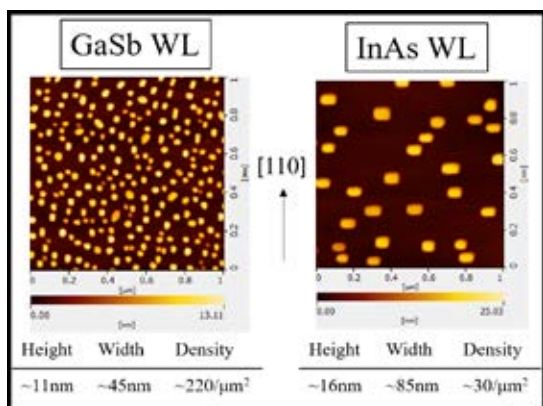


Figure 2: AFM imagery and statistics of the GaSb QDs grown using different wetting layers.

Results and Discussion:

AFM images show a sharp difference in the QD structures when using the two different wetting layers (Figure 2).

The InAs wetting layer sample had much larger and sparser QDs. PL spectra were also much different for the two samples (Figure 3). While both samples had a peak at around 1.25 eV, the peak for GaSb was not the ground state energy, and was instead around 1.05 eV. The PL data indicated that the device with the InAs wetting layer had a shallower ground state energy level in the type II configuration. JV curves showed that the device with the InAs wetting layer had much better performance (Fig.4).

Differences in the size of dots and the density in the QD layer were due to diffusion in the S-K growth process when using different wetting layers. We expected the larger dots in the InAs wetting layer device to lead to a deeper well ground state energy, which would mean the PL peak should be at a lower energy. But instead, the GaSb wetting layer device had a lower PL peak. Further investigation into this anomaly is necessary.

The lower open circuit voltage in the GaSb wetting layer solar cell can be explained by the absorption peak at a lower photon energy. The shallower ground state energy level in the InAs wetting layer device led to easier thermal excitations and a more efficient solar cell. However, a two-step photocurrent measurement is still necessary to characterize the intermediate band solar cell implementation.

Acknowledgements:

We acknowledge CNF iREU Program support from the National Science Foundation under Grant No. OISE-1559368.

References:

- [1] W. Shockley, and H.J. Queisser (1961). Applied Physics 32(510).
- [2] A. Luque, and A. Marti (1997). Physical Review Letters 78(26).
- [3] Y. Okada, K. Yoshida, Y. Shoji, and T. Sogabe (2013). IEICE Electronics Express 10.
- [4] A. Marti, N. Lopez, E. Antolin, E. Canovas, C. Stanley, C. Farmer, L. Cuadra, and A. Luque (2006). Thin Solid Films 512: 638-644.
- [5] Y. Shoji, R. Tamaki, and Y. Okada (2017). AIP Adv. 7(065305-1).
- [6] M. Elborg, T. Noda, T. Mano, M. Jo, Y. Sakuma, K. Sakoda, and L. Han (2014). Solar Energy Materials and Solar Cells 134: 108-113.
- [7] C.-K. Sun, G. Wang, J. Bowers, B. Brar, H.-R. Blank, H. Kroemer, and M. H. Pilkuhn (1996). Applied Physics Letters 68(11).
- [8] R. People, and J.C. Bean (1985). Applied Physics 47(3).
- [9] D. Leonard, M. Krishnamurthy, C. M. Reaves, S. P. Denbaars, and P. M. Petroff (1993). Applied Physics Letters 63(23).

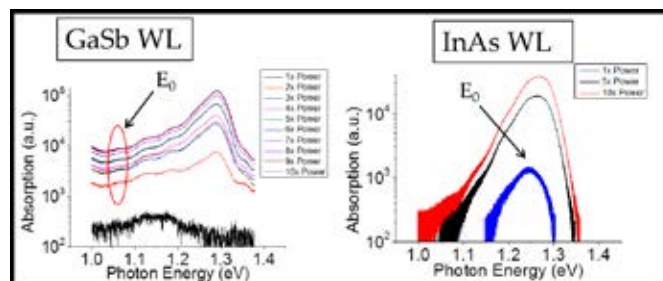


Figure 3: PL data for the samples.

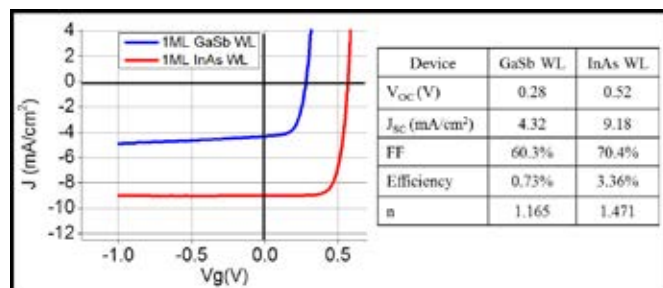


Figure 4: IV characterization under AM1.5G illumination.

Investigating the Structure of Multiferroic Oxides with STEM Imaging and Diffraction Mapping

Iryna Glushchenko, 2018 PARADIM REU Intern

Physics, Princeton University

REU Program: 2018 Platform for the Accelerated Realization, Analysis, and Discovery of Interface Materials Research Experience for Undergraduates (PARADIM REU) Program

PARADIM REU Principal Investigator: Dr. Darrell Schlom, Materials Science and Engineering, Cornell University

PARADIM REU Mentor: Dr. Megan Holtz, Materials Science and Engineering, Cornell University

Primary Source of PARADIM REU Funding: Support for PARADIM is provided under NSF Grant # DMR-1539918 as part of the Materials Innovation Platform Program

Contact: iag@princeton.edu, schlom@cornell.edu, meh282@cornell.edu

Websites: <http://paradim.cornell.edu/education>, http://www.cnf.cornell.edu/cnf_2018reu.html

Abstract:

Multiferroics are a type of material that exhibit both ferroelectric and ferromagnetic properties. Their unique coupling of electric and magnetic ordering means these materials create exciting possibilities for data storage technologies. However, few multiferroics exist at room temperature, and those that do typically have weak magnetic moments or electrical polarization. Combining the ferroelectric LuFeO_3 with the ferrimagnetic CoFe_2O_4 into a superlattice by molecular beam epitaxy (MBE) promises to overcome this problem, creating a material with spontaneous polarization and magnetization at room temperature. Scanning transmission electron microscopy (STEM) is used to investigate how these materials are layered together at the atomic scale and gain feedback on our MBE growth. Through means of a pixel array detector developed at Cornell, we use scanning diffraction combined with new data processing techniques to study the crystal structure of our material.

Summary of Research:

To create a multiferroic material, we combined the ferroelectric LuFeO_3 with the insulating ferrimagnetic CoFe_2O_4 into a superlattice (Figure 1). The CoFe_2O_4 is particularly promising for future use in data storage technologies because it is not only structurally compatible with LuFeO_3 , it also exhibits ferrimagnetic properties at a much higher temperature than the previous ferromagnetic material used in this multiferroic, LuFe_2O_4 . Furthermore, the material must be insulating so as to not shield the polarization of the ferroelectric layers. The hexagonal LuFeO_3 is stabilized on the cubic yttrium stabilized zirconium (YSZ) $\langle 111 \rangle$ substrate, with a metal electrode in between to facilitate future ferroelectric testing.

Since our multiferroic had already been grown by MBE, we immediately began investigating its structure. To prepare a sample of our material for STEM analysis, we used a focused ion beam (FIB). Through STEM, we obtained information on the crystal structure of the multiferroic film on the atomic scale. We were specifically interested in the interfaces between the electrode, LuFeO_3 ,

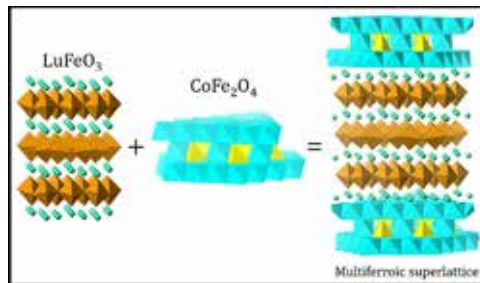


Figure 1: A representation of the crystal structure of the LuFeO_3 and CoFe_2O_4 multiferroic film.

and CoFe_2O_4 , and in examining the picometer-scale displacements driving ferroelectricity.

Afterwards, we mapped the crystal structure with a new pixel array detector developed at Cornell to produce convergent beam electron diffraction (CBED) patterns. While this is a promising method to identify different structures, CBED patterns have their drawbacks. They are easily influenced by tilts and thickness effects in the sample, which change the relative intensity of diffraction spots, making dark-field imaging of particular domains unreliable. Also, the resulting disks in diffraction space from a convergent beam are large, complicating the matter of precisely localizing diffraction spacings. To overcome these challenges, we used the Fourier Transform $\text{FT}[\log(\text{CBED})]$. The logarithm suppresses the effect of tilt variations, and the transform concentrates the diffraction disk signals into well-defined spots corresponding to atomic spacings. These can be separated by dark-field imaging, which can then be used to make real-space maps of the crystallographic zones inside our material.

Results and Conclusions:

From atomic imaging, we discovered that although the film has good structure overall, it exhibits some uneven layering — there are several partial layers at the interfaces of the LuFeO_3 and CoFe_2O_4 , so to further improve superlattice growths, we must perfect the shutter time calibration and the temperature during growth. Also, the electrode layer displays two crystal orientations with the $\langle 111 \rangle$ out-of-plane orientation, the $[01\bar{1}]$ and $[11\bar{2}]$, potentially because it nucleated with different grain orientations at the beginning of the MBE growth. Growing the electrode on a better lattice-matched substrate may improve the epitaxy. Excitingly, the LuFeO_3 layers exhibit ferroelectric distortion, and we observe domain walls where the polarization of the lutetium atoms changes throughout the layer (Figure 2). Finally, the interface between the LuFeO_3 and CoFe_2O_4 in our sample seems to prefer a 2/3 ratio of lutetium — while usually the lutetium is found in groups of three, at the interface it is in pairs. This suggests that there may not be enough lutetium added during growth.

Figure 3 displays the CBED data transformations, and as we can see, the logarithm drastically improves the amount of visible data. The Fourier Transformed data can be used to isolate the different crystal zone regions within our sample in real space (Figure 4). Even though we were already aware of our film structure, the purpose of this process is to develop this data processing technique — if applied to materials we know the structure of, we can construct a method and database that will be useful when we encounter more complex systems.

Future Work:

Further research on this multiferroic can take several directions. This sample alone still holds a wealth of information — for instance, methods such as electron energy-loss spectroscopy (EELS) and x-ray energy dispersive spectroscopy (EDS) can determine the relation between interdiffusion and growth conditions. Long-term wise, the next step is to conduct ferroelectric testing on this material, such as determining how much electric field is needed for the ferroelectric layer to switch, or observing the polarization at different amounts of charge. Ultimately, the goal is to test whether the ferroelectric switching can be coupled to that of the magnetization.

Acknowledgements:

I would like to thank my mentor, Dr. Megan Holtz, and my PI, Dr. Darrell Schlom, for their guidance. Also, thank you to the PARADIM/CNF staff for their tireless efforts throughout the summer. Furthermore, thank you to the CCMR facilities for the use of their equipment and to Cornell University for hosting me over the summer. Finally, thank you to the NSF for funding this experience — support for PARADIM is provided under DMR-1539918 as part of the NSF Materials Innovation Platform Program.

References:

- [1] Mundy, J., Brooks, C., Holtz, M., et al. "Atomically engineered ferroic layers yield a room temperature magnetoelectric multiferroic." *Nature*, Vol 537, 523-541, 22 September 2016.

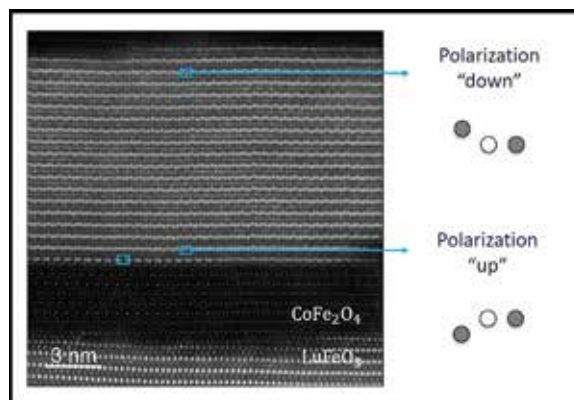


Figure 2: A layer of LuFeO_3 displaying ferroelectric distortion and a 2/3 ratio of lutetium at the interface between the LuFeO_3 and CoFe_2O_4 layer.

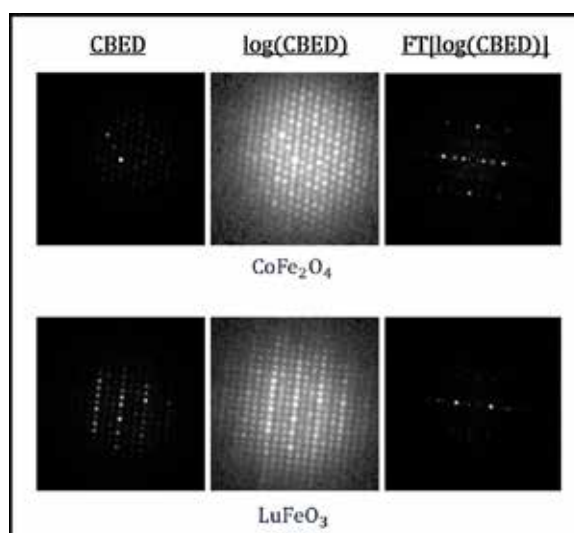


Figure 3: CBED to $\text{FT}[\log(\text{CBED})]$ data transformations for LuFeO_3 and CoFe_2O_4 .

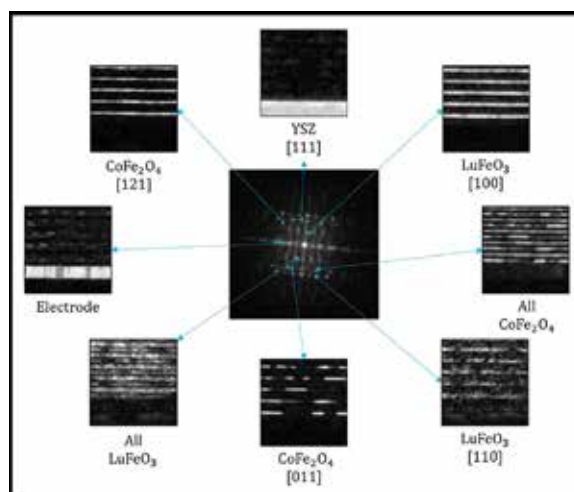


Figure 4: The real-space crystallographic zones of the multiferroic film can be isolated using dark-field imaging from the diffraction patterns obtained after the Fourier Transform.

Automating a Cryogenic Transport System for Measuring Quantum Materials

Ken Ho Tai Ran, 2018 PARADIM CU REU Intern

Electrical and Computer Engineering, College of Engineering, Cornell University

REU Program: 2018 Platform for the Accelerated Realization, Analysis, and Discovery of Interface Materials Research Experience for Undergraduates Program at Cornell (PARADIM CU REU)

PARADIM CU REU Principal Investigator: Prof. Kyle Shen, Department of Physics, Cornell University

PARADIM CU REU Mentor: Jacob Ruf, Department of Physics, Cornell University

Primary Source of PARADIM CU REU Funding: Support for PARADIM is provided under NSF Grant # DMR-1539918 as part of the Materials Innovation Platform Program

Contact: kth62@cornell.edu, kmshen@cornell.edu, jpr239@cornell.edu

Websites: <http://paradim.cornell.edu/education>, http://www.cnf.cornell.edu/cnf_2018reu.html

Abstract:

Collection of resistivity-temperature data is necessary for the determination of the residual resistance ratio (RRR) of samples, and is further useful for observing other material characteristics, including the Curie temperature of superconducting materials. Two current measurement methods are utilized: a cryogenic transport measurement system and the physical property measurement system (PPMS). This report will detail the mechanization and automation of the former, with the intent of creating an upgradable, semi-modular, automated system with improved reliability and reduced operator involvement.

Summary of Research:

Design Considerations. The current cryogenic transport measurement system measures resistivity temperature data by immersing a sample attached to a four-point terminal sensor into a dewar of liquid helium. The sensor itself is attached to a 1.5 meter long rod, with a connection box on the opposing end. The temperature is controlled by the physical positioning of the probe within the dewar, with the probe being slowly lowered until it reaches the surface of the liquid helium. The rate of change in temperature is controlled via operator feedback, with users adjusting the depth of the probe to maintain the approximate desired rate. This process on a whole takes 1-1.5 hours to complete, and is significantly faster than the PPMS system, which takes 6-7 hours. However the process requires the operator to be present for the entirety of its duration, and with the throughput of upwards of 70 samples a month, the time spent operating the system is nontrivial.

Other motivating factors for changes to the existing system include improving the mechanical reliability of the system. At maximum excursion, the probe connection box is lifted close to three meters off the ground. Because the center of gravity is located at this height without additional support, the rod has warped over its lifespan, leading to occasional mechanical stoppage and increased difficulty in the lowering and raising process. Likewise,

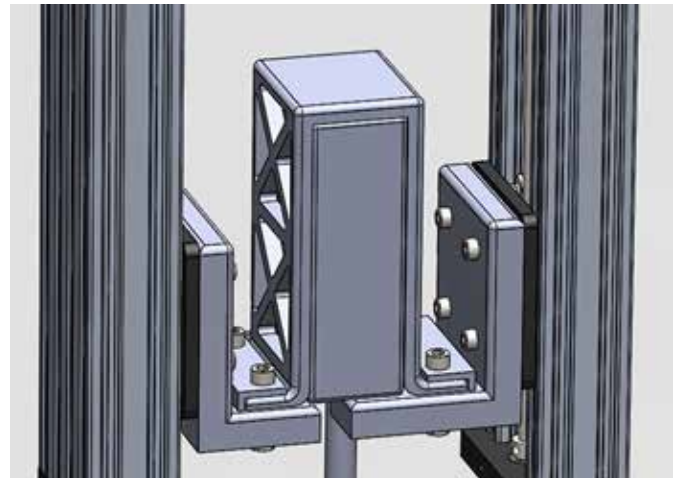


Figure 1: Mounting bracket within SolidWorks CAD software.

variation in measurement methods has also led to incorrect usage of the system.

The current system could therefore be improved by adding a hardware layer involving mechanization and automation. In addition to improving mechanical robustness, mechanization would allow for set usage of the system and further reduce potential operator error.

Hardware Design. To replace the manual mode of raising and lowering the probe, mechanized linear actuation was required. Of equal consideration was the significant travel distance necessitated for the process (one meter). The chosen option involved the implementation of a lead-screw linear actuator. This was favored over a ball-screw design because the latter would have necessitated the use of braking mechanisms and was generally less suited for vertical application. Belt-driven actuation is suited for high-speed travel but is otherwise inferior for the planned use case, suffering from slippage and poorer actuation control. A worm-screw system would require a significant re-design of the system, which was beyond the scope of the project.

To drive the linear actuators, two NEMA-23 style motors with 345 oz-in of torque were chosen. While the load imposed by the probe itself is minimal, the friction created by the o-ring seal was not. Furthermore, microstepping the motors to increase resolution would also have led to a corresponding decrease in torque. These factors necessitated the selection of higher torque motors. The mounting bracket to hold the probe was designed in SolidWorks and underwent several rapid prototyping iterations using the various 3D printers available through the ECE Makerspace and RPL. This allowed for several versions of the bracket to be developed within the span of two weeks, each with iterative improvements.

Software Design. To interface between the aforementioned hardware and the existing LabView environment used for data-taking, an Arduino microcontroller with the LabView interface for Arduino (LIFA) package was utilized. LIFA provides serial communications with the Arduino microcontroller via the LabView virtual instrument software architecture (VISA), and allows for programming of the microcontroller within the LabView environment. This enables firmware changes to be made without the need to enter a dedicated low-level programming environment, which should increase program serviceability and usability.

Software is built on state machine architecture, which is suited for the automation required by the project. The architecture further enforces a set number of “states” for the machine to exist in, and should also help to standardize measurement methods between various operators of the system. The original data-taking software has since been added as a sub-VI into the integrated motion control and measurement system.

Current Status and Future Work:

Currently, the proposed dipper system has been assembled, with electronics fully integrated. The system has completed initial trial runs, which have proven the functionality of the linear actuation method. Planned short-term improvements include designing further hardware fail-safes into the system, improving the user

interface for the software, and adding z-axis distance sensing for the actuators. Longer-term work will include the integration of a new version of the probe, as well as development of PID controls for actuation.

Acknowledgements:

The author would like to thank Professor Kyle Shen, mentor Jacob Ruf, Shen Group and PARADIM members, and Professor Julie Nucci for their guidance and assistance in this project. The author would also like to acknowledge the NSF, which has made the project possible through the Platform for the Accelerated Realization, Analysis, and Discovery of Interface Materials (PARADIM) under grant number DMR-1539918.

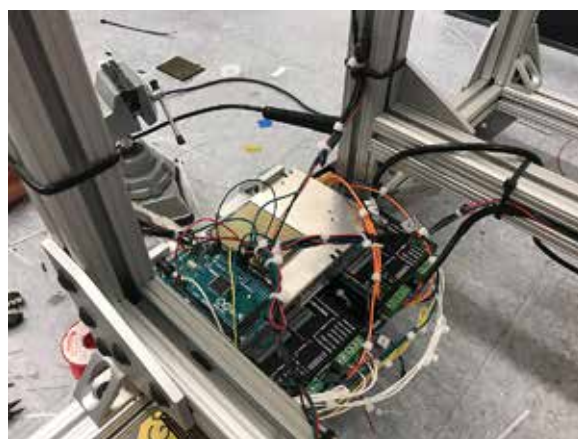


Figure 2: Integrated electronics bay for system.



Figure 3: Completed system in unloaded position.

New Photopatterning Materials for Advanced Lithography

Jordan Phillip Howard-Jennings, 2018 CNF REU Intern

Engineering, Harvey Mudd College

REU Program: 2018 Cornell NanoScale Science & Technology Facility Research Experience for Undergraduates Program

CNF REU Principal Investigator: Christopher Kemper Ober, Materials Science and Engineering, Cornell University

CNF REU Mentors: Kazunori Sakai, Materials Science and Engineering, Cornell University; Seok-Heon Jung, Materials Science and Engineering, Cornell University; Christopher Alpha, CNF, Cornell University

Primary Source of CNF REU Funding: National Science Foundation via the National Nanotechnology Coordinated Infrastructure (NNCI) Grant No. NNCI-1542081

Contact: jhowardjennings@g.hmc.edu, ks2288@cornell.edu, sj736@cornell.edu, alpha@cnf.cornell.edu

Website: http://www.cnf.cornell.edu/cnf_2018reu.html

Abstract:

Photolithography, which is a patterning method used to produce micro/nano-scale features, is currently approaching capabilities of producing sub-10 nm features at EUV wavelengths [1]. We present the findings of material development and characterization of model chemically amplified resists (CARs) to study novel photoacid generators (PAGs), as well as of Zn and Zr metal oxide nanoparticle (MO-NP) resists which offer many advantages over CARs.

Background:

For the past decade, the semiconductor industry has been using immersion lithography to make deep-UV lithography critical dimensions smaller [2]. However, and particularly with CARs which utilize PAGs to “amplify” the photo-reaction that occurs upon exposure, two issues arise: defective patterns resulting from the leaching of resist into the immersion fluid [2], and a sensitivity boost at the expense of line-edge roughness (LER) [3,4]. For EUV lithography to become an industry standard, current materials development of EUV resists must address these issues.

MO-NPs have garnered attention for resist development because they offer many potential and realized advantages to current resist technologies: smaller size relative to polymer photoresists [5], and a ligand-exchange photoreactive mechanism that is more controllable than the deprotection reactions that occur with generated photoacids in conventional resists [6], among other benefits. Currently, metal oxide methacrylate resists produced from hafnium and zirconium have been shown to be potential candidates for EUV resists because of their high resolution and sensitivity [6].

Furthermore, the ligand-exchange mechanism occurring between the acid groups on the metal oxides and the generated photoacids that produces a solubility switch in the exposed area is of interest of further investigation. Since there is a direct correlation between scumming (a phenomena associated with high LER) and the

type of PAG used [3], a study of how PAGs alter resist performance is necessary for understanding how newly developed PAGs may provide better compatibility for EUV MO-NP resists.

Materials and Methods; Synthesis

MO-NP Resists. Resist solutions were prepared by combining 91 mg metal oxide, 9.1 mg PAG (N-hydroxynaphthalimide triflate), and 1.9 g PGMEA in a small glass vial. The metal oxide and PAG were dissolved in PGMEA through 12-16 minutes of stirring on a handheld vortex mixer.

Model CARs. Resist solutions were prepared by synthesizing the monomers tert-butyl methacrylate, isobornyl methacrylate, and methacrylic acid with AIBN as an inhibitor. Once this product was formed, it was mixed with a PAG and PGMEA and dissolved by exposure to a heat gun and vigorous hand-mixing for 10-15 minutes.

Materials and Methods; Lithographic Conditions

MO-NP Resists. Resists were spun onto bare silicon wafers at 2000 rpm for 60s and given a 60s soft bake at 40°C (Zr) or 70°C (Zn). The wafers were then exposed using a 248 KrF source ASML DUV stepper at a dose of

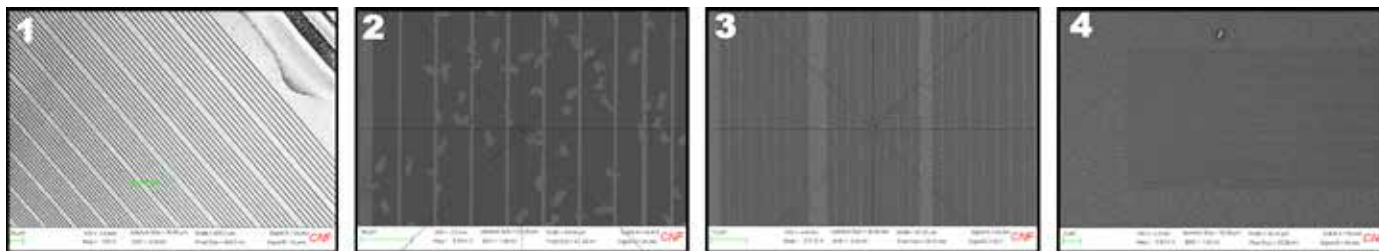


Figure 1: SEM image of various width patterns (largest 1000 nm) of Zn-oxide NP resists. Figure 2: SEM image of a 1000 nm-width pattern from the Zn-oxide NP resist. Figure 3: SEM image of a 500 nm-width pattern (center) from the Zr-oxide NP resist. Figure 4: SEM image of a pattern exposed region from the CARs.

150 mJ/cm², and subsequently developed in a range of solvents including o-xylene and m-xylene (Zr) as well as toluene and decaline (Zn).

Model CARs. DUV-42P bottom anti-reflective coating (BARC) was spun onto bare silicon wafers at 4000 rpm and given a 60s soft bake at 200°C. Resists were spun onto these wafers at 3000 rpm for 60s and given a post-annealing bake (PAB) at 100°C. Exposure took place on the ASML DUV stepper using an exposure dose matrix ranging from 10 to 358 mJ/cm², and subsequently given a 60s post-exposure bake (PEB) at 100°C before development in diluted TMAH for 60s using the Hamatech wafer processor.

Materials and Methods; Characterization

An assortment of optical microscopes capable of imaging nanometer-grade patterns were used to “check” that patterns had registered among the many pre-final lithographic steps. Once developed, scanning electron microscopy was used to qualitatively evaluate resist performance using the Zeiss Supra and Zeiss Ultra models of their SEMs. For the CARs, a pre-SEM step of sputtering a thin Au/Pd layer on the wafer surface was required to reduce SEM overcharging.

Results and Conclusions:

MO-NP Resists. Current resist development demonstrates that while good feature production is possible (Figure 1), randomly dispersed particle defects (Figure 2) and incomplete pattern registering (Figure 3) significantly distort these features. The cause of these defects is not currently understood. For the Zn-oxide resist evaluated, the gradient-matching between the particle defects and the exposed/non-developed regions (lighter area) suggest that there could be issues in material preparation such as mixing of components.

Model CARs. While the appearance of desired patterns offers confirmation that the lithography happened, the model CARs run into two issues: First, randomly

dispersed porous defects dominate both the exposed and non-exposed areas, strongly suggesting that further materials development is needed. Second, the small gradient change between the patterned and non-patterned regions suggests that the height of the patterns is negligible (this observation is confirmed by the optical profilometer), suggesting that lithographic conditions used were not optimal.

Future Work:

Further materials development in conjunction with lithographic parameter optimization is necessary to reduce the preliminary defects observed in both the MO-NP resists and the model CARs. After these defects are eliminated, an expansive design-of-experiments may be implemented to evaluate factor interactions between different material properties (i.e., PAG type/amount, metal oxides, etc.) and lithographic conditions (i.e., spin times, bake times, exposure doses, etc.).

Acknowledgements:

This work was performed in part at the Cornell NanoScale Facility, a member of the National Nanotechnology Coordinated Infrastructure (NNCI), which is supported by the NSF (Grant NNCI-1542081).

References:

- [1] Li, Li, et al. Chemical Society Reviews. doi: 10.1039/C7CS00080D (2017).
- [2] Petrillo, Karen, et al. Advances in Resist Technology and Processing XXII. doi: 10.1117/12.601621(2005).
- [3] Kosma, Vasiliki, et al. “Extreme Ultraviolet (EUV) Lithography IX. doi: 10.1117/12.2297383 (2018).
- [4] Thiyagarajan, Muthiah, Kim Dean, and Kenneth E. Consalves. Journal of Photopolymer Science and Technology. doi: 10.2494/photopolymer.18.737 (2005).
- [5] Krysak, Marie, et al. Advances in Resist Materials and Processing Technology XXVIII. doi: 10.1117/12.879385 (2011).
- [6] Jiang, Jing, et al. Journal of Photopolymer Science and Technology. doi: 10.2494/photopolymer.27.663 (2014).

High Dynamic Gas Pressure Single Crystal Growth

Zachary Kennedy, 2018 PARADIM JHU REU Intern

Physics, Georgia Institute of Technology

REU Program: 2018 Platform for the Accelerated Realization, Analysis, and Discovery of Interface Materials
Research Experience for Undergraduates Program at Johns Hopkins University (PARADIM JHU REU)

PARADIM JHU REU Principal Investigators: Dr. Tyrel McQueen, Department of Chemistry, Johns Hopkins University;
Dr. W. Adam Phelan, Department of Chemistry, Johns Hopkins University

Primary Source of PARADIM JHU REU Funding: Support for PARADIM is provided under NSF Grant # DMR-1539918
as part of the Materials Innovation Platform Program

Contact: zakkenedy@gatech.edu, mcqueen@jhu.edu, wphelan2@jhu.edu

Websites: <http://paradim.cornell.edu/education>, http://www.cnf.cornell.edu/cnf_2018reu.html

Abstract:

The study of frustrated magnetic systems is of interest due to their potential to elucidate unique low temperature thermodynamics and to advance technological capabilities through quantum computing. One system of particular interest is the $\text{RE}_3\text{Sb}_3\text{Mg}_2\text{O}_{14}$ system, where RE represents a rare earth element. This system is a derivative of the classic spin-ice pyrochlore structure, but interestingly, has a 2-D layered kagomé sublattice composed of rare earth atoms (see Figure 1). Additionally, this system shows antiferromagnetic interaction between nearest neighboring atoms, which combined with its kagomé structure, makes it an excellent quantum spin liquid candidate. The difficulty with this material is growing single crystals, which are required to further explore the system's low temperature thermodynamics through inelastic neutron scattering. The crystal growing method of choice is the high pressure floating zone technique. The challenge of growing single crystals with these materials is finding the correct set of thermodynamic conditions where the material melts congruently, and a floating zone can be established. This project will mainly focus on growing single crystals of the neodymium analog of this material for several reasons. Firstly, neodymium has three unpaired electrons in its valence shell, thus it has a magnetic moment. Secondly, the powdered form of this material has been extensively studied [2] and is confirmed to have interesting antiferromagnetic interactions.

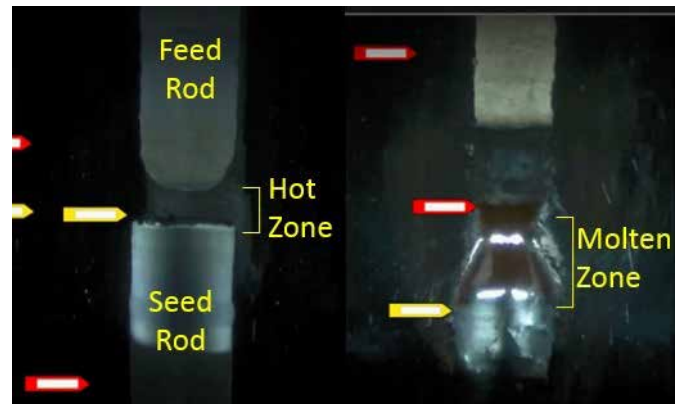


Figure 1: [1] A simplified representation of the structure of the $\text{Nd}_3\text{Sb}_3\text{Mg}_2\text{O}_{14}$ system. The image on the left visualizes the corner sharing triangles that compose the neodymium kagomé sublattices. The image on the right displays one (MgNd_3) of the two characteristic tetrahedra that compose its pyrochlore structure.

Summary of Research:

The floating zone technique (see Figure 2) utilizes a beam of focused light to create a small "hot zone" where the energy is absorbed by the sample. Two rods, normally composed of polycrystalline powder of the desired composition, are placed on either side of the hot zone. The rod underneath the hot zone is known as the seed rod and it is where the single crystal will be grown. The top rod is known as the feed rod, and it ensures that the molten zone is filled with enough material to maintain its stability. The first step of a floating zone growth is to melt the tip of the seed rod. Then, the feed rod is lowered onto the molten tip of the seed rod and a liquid floating zone is established between the two rods. Once the zone is deemed stable, the feed and seed rods are slowly lowered causing the liquid to crystallize on the

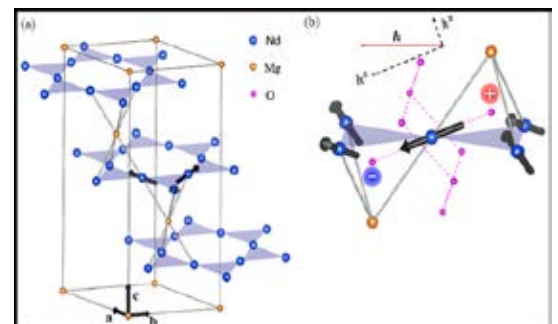


Figure 2: The arrangement of the classical floating zone growth before and after the floating zone is established.

seed rod. Initially, the solidifying liquid will form many domains, but eventually, due to the thermodynamics of the system, a single domain will be selected and a single crystal will have been grown.

This procedure will be known as the “classical floating zone growth technique”, but there are several variations of this technique. The first variation is known as the “pedestal growth technique”. This method utilizes a very thin upper rod to attempt to pull a crystal up and out of a melt. Using a thin rod allows for easier access to melts that would be difficult to connect with two full sized rods. Additionally, various materials may be used for this top rod, which may improve the adhesion and stability of the melt. The second variation is known as the “traveling solvent technique”. This method is functionally the same as the classical growth technique, but a small pellet of solvent is placed on top of the bottom rod during set up. This pellet of solvent serves to aid the melting of the desired material while, ideally, resulting in as little impurities as possible. All three of these methods were used in this study.



Figure 3, left: Result of the classical floating zone growth attempt at 165 bar. Figure 4, right: Result of the traveling solvent floating zone growth with pure Li₂MoO₄ at 150 bar.

Results and Conclusions:

Classical floating zone growth was attempted at 150 bar, 185 bar and 200 bar. No stable floating zones were established (Figure 3). Powder x-ray diffraction indicates that this material melts congruently (does not change composition when melting) under these thermodynamic conditions, but the molten material does not adhere to the solid rod, forms a solid outer shell, and frequently cracks under the conditions required to melt it.

Pedestal floating zone growth was attempted at 200 bar using an alumina top rod. The molten material also did not adhere to the alumina rod. Additionally, the temperature required to melt the kagomé is too high and causes the alumina to melt prematurely.

Traveling solvent floating zone growth was attempted with MgSb₂O₆ at 165 bar and Li₂MoO₄ at 150 bar. After signs of success with pure Li₂MoO₄, pellets of 1:1 and 3:1 molar ratios of Li₂MoO₄ to Nd₃Sb₃Mg₂O₁₄ were attempted. The MgSb₂O₆ flux is not viable as it has a melting point above that of Nd₃Sb₃Mg₂O₁₄. Pure Li₂MoO₄ showed potential as a stable floating zone was established (see Figure 4), but further exploration is needed to find the correct thermodynamic conditions to form a crystal. Powder x-ray diffraction indicates that the Li₂MoO₄ did not form a new compound with Nd₃Sb₃Mg₂O₁₄. This is another good indicator that it could be used as a potential flux. No stable floating zones were established using the pellets composed of both Li₂MoO₄ and Nd₃Sb₃Mg₂O₁₄.

Future Work:

Future work should target a way to better sinter the rods of Nd₃Sb₃Mg₂O₁₄. Increased density of these rods will only serve to increase the consistency of repeated experiments as well as prevent melts from being sucked into the rods. Finally, further research into the traveling solvent, with both Li₂MoO₄ and other solvents, shows the greatest promise toward growing single crystals of Nd₃Sb₃Mg₂O₁₄.

Acknowledgements:

NSF Grant DMR-1539918, Dr. Michal Winiarski, Lucas Pressley, Jessica Zahn, Juan Chamorro.

References:

- [1] Z. L. Dun, et al. arXiv:1806.04081 (2018).
- [2] A. Scheie, et al. arXiv:1604.03950 (2016).
- [3] W.A. Phelan, J. Zahn, Z. Kennedy, and T.M. McQueen, “Pushing Boundaries: High Pressure, Supercritical Optical Floating Zone Materials Discovery,” Submitted J. Sol. St. Chem. (2018).

Non-Equilibrium Investigations of Canted Antiferromagnet Under Flowing Electrical Current

Yonghun Lee, 2018 PARADIM CU REU Intern

Engineering Physics, Cornell University

REU Program: 2018 Platform for the Accelerated Realization, Analysis, and Discovery of Interface Materials Research Experience for Undergraduates Program at Cornell (PARADIM CU REU)

PARADIM CU REU Principal Investigator: Professor Kyle Shen, Department of Physics, Cornell University

PARADIM CU REU Mentor: Jocienne Nelson, Department of Physics, Cornell University

Primary Source of PARADIM CU REU Funding: Support for PARADIM is provided under NSF Grant # DMR-1539918 as part of the Materials Innovation Platform Program

Contact: YL634@cornell.edu, kmshen@cornell.edu, jnn26@cornell.edu

Websites: <http://paradim.cornell.edu/education>, http://www.cnf.cornell.edu/cnf_2018reu.html

Abstract:

Strontium iridium oxide (Sr_2IrO_4) is an antiferromagnetic Mott insulator, driven by strong spin-orbit coupling and Coulomb repulsion. The spin-orbit interaction locks the IrO_6 octahedra rotation and Ir magnetic moment canting. Recently, the current-induced metal-insulator transition in bulk single crystals of Sr_2IrO_4 was reported [1]. According to the study, the coupling of flowing electrical current and canting angle leads to an a-axis lattice expansion of up to 1%; this nonlinear change in lattice and magnetic structure drives a unique resistive switching behavior. For the 2018 PARADIM REU Program, we tested the electrical control of Sr_2IrO_4 in a thin film platform and clarified the physical mechanisms behind the current-induced metal-insulator transition of Sr_2IrO_4 .

Summary of Research:

Epitaxial Sr_2IrO_4 thin films, grown by molecular-beam epitaxy on LSAT <001>, NGO <001>, and STO <001> substrates, were tested at the probe station equipped with Keithley 4200A-SCS Parameter Analyzer and 4225-PMU Ultra-Fast I-V Module (for pulsed-IV). For low temperature measurements, the probe station was cooled down to $T = 80$ K by liquid nitrogen.

The current-induced electrical control implies that the current density required for metal-insulator transition should be comparable across Sr_2IrO_4 samples with different sizes. Comparison with the reported single crystal data [1], along with simple calculations of the ratio of cross-sectional area of current flow, gave a rough estimation on the amount of current required for switching in Sr_2IrO_4 thin film ($\sim 1 \mu\text{A}$). However, no nonlinear behavior was observed with Sr_2IrO_4 thin films within the compliance limit (10 mA) imposed by the probe station electronics. It was clear that the mechanism of switching in epitaxial thin films is different from bulk single crystals, because of the huge disparity of current density required for resistive switching.

Subsequent experiments were done with smaller film devices fabricated and patterned by platinum electrodes on each side. The devices' dimension was in the order of

$10 \mu\text{m} \times 10 \mu\text{m}$. Film devices with smaller cross-sectional area of current flow enabled larger current density input, and we were able to induce the nonlinear resistive switching both at $T = 300$ K and $T = 80$ K.

Results and Conclusions:

Switching behaviors and Joule heating effect observed at room temperature can be explained by the oxygen vacancy migration-driven resistive switching of oxide thin films. Under a large electric field, oxygen vacancies migrate, cluster, and form conducting filaments in oxide films [2]. If the filaments are stable after an initial voltage sweep, the film enters into a non-volatile low-resistance state—memory switching (Figure 1). On the other hand, if the filaments cannot be maintained during the voltage sweep, the low-resistance state is volatile and only maintained at the large voltage bias, returning to the original high-resistance state below a certain voltage threshold—threshold switching (Figure 2).

The migration of oxygen vacancies can be modeled as a 'hopping' process in a periodic potential. The hopping rate is very slow under E-field alone. Joule heating accelerates the hopping rate by creating a large thermal

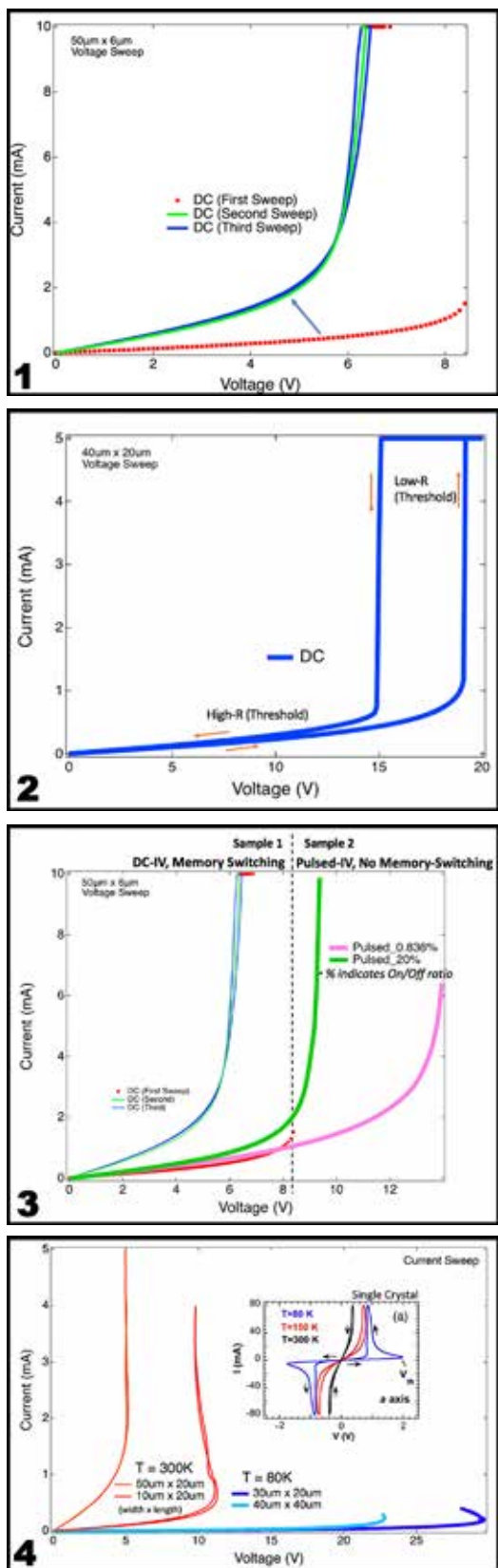


Figure 1, top: Memory resistive switching observed in Sr_2IrO_4 thin film (film dimension: width \times length). **Figure 2, upper middle:** Threshold resistive switching observed in Sr_2IrO_4 thin film. **Figure 3, lower middle:** Nonlinear resistive switching: Comparison of DC- and pulsed-mode. **Figure 4, bottom:** DC current-induced resistive switching observed in Sr_2IrO_4 thin film at $T = 300\text{ K}$ and $T = 80\text{ K}$. Inset: I-V characteristic of DC current applied along the a -axis of Sr_2IrO_4 single crystal reported by G. Cao, et al. [1].

gradient near the conducting filaments [2]. Figure 3 shows that the reduction of Joule heating under the pulsed I-V mode subdues the memory resistive switching originally found on the other film device of the same geometry.

Comparison of DC and pulsed I-V characteristic of multiple devices further showed that the nonlinear behavior originally found under DC mode disappeared under pulsed mode. The necessity of Joule heating in the resistive switching supports our hypothesis that the switching behavior of Sr_2IrO_4 at room temperature is an indication of the formation of conducting filaments consisting of oxygen vacancies.

The nonlinear I-V characteristic at $T = 80\text{ K}$, cut off at the onset of the switching behavior, exhibits a similar pattern of negative differential resistance found with the bulk single crystal [1] (Figure 4). It gives an inconclusive hint of what can potentially be the metal-insulator transition driven by the coupling of electrical current and Ir magnetic moment canting.

Further increase in current bias destroyed the film devices under testing, the reason why a comprehensive study on Sr_2IrO_4 's metallic state could not be done.

Future Work:

Further exploration of the nonlinear switching behavior below room temperature is required. More experiments with pulsed I-V should be done at low temperature to root out the possibilities of oxide film's typical oxygen vacancy migration- or joule heating-driven resistive switching.

The film devices cracked most likely due to structural changes. Sr_2IrO_4 in a thin film is more prone to cracking under structural changes than in a bulk single crystal, because of the hard substrate clamping the film grown above. This unfortunately means that it is hard to investigate deep into the metallic state, because current-induced metal-insulator transition is accompanied by large structural change—in particular, the expansion of a -axis lattice as a result of IrO_6 octahedral rotation.

If the device breakdown can be circumvented, the electronic structure of Sr_2IrO_4 in the current-induced metallic state will be studied by angle-resolved photoemission spectroscopy (ARPES). If the metallic state cannot be achieved in the thin film platform, we plan to perform the ARPES study with a bulk single crystal Sr_2IrO_4 .

Acknowledgements:

Support for PARADIM is provided under NSF Grant # DMR-1539918 as part of the Materials Innovation Platform Program.

References:

- [1] G. Cao, J. Terzic, H.D. Zhao, H. Zheng, L.E. De Long, and Peter S. Riseborough, Phys. Rev. Lett. 120, 017201 (2018).
- [2] J. Lee, S. Lee, and Tae W. Noh, Appl. Phys. Rev. 2, 031303 (2015).

Growing and Characterizing Monolayer Transition Metal Dichalcogenides (2D TMDs) Materials for PARADIM Users

Cesar Lema, 2018 PARADIM REU Intern

Bachelor of Science in Physics and Mathematics, New York University

REU Program: 2018 Platform for the Accelerated Realization, Analysis, and Discovery of Interface Materials Research Experience for Undergraduates (PARADIM REU) Program

PARADIM REU Principal Investigator: Dr. Darrell Schlom, Materials Science and Engineering, Cornell University

PARADIM REU Mentor: Mr. Don Werder, Cornell Center for Materials Research, Cornell University

Primary Source of PARADIM REU Funding: Support for PARADIM is provided under NSF Grant # DMR-1539918 as part of the Materials Innovation Platform Program

Contact: cl4393@nyu.edu, schlom@cornell.edu, djw326@cornell.edu

Websites: <http://paradim.cornell.edu/education>, http://www.cnf.cornell.edu/cnf_2018reu.html

Abstract:

Intense research into new atomically thin semiconducting materials has the electronics and semiconductor industries excited, however, the largescale monolayer growth of one of the earliest descendants of the class, transition metal dichalcogenide (TMD) films with spatial continuity and high electrical performance remains a challenge [1]. Metal-organic chemical vapor deposition (MOCVD) is a low temperature and versatile deposition process that is industrially scalable and proven to be a promising way to engineer film structure to produce high quality monolayer TMD films [2]. In our research, we grew monolayer molybdenum disulfide (MoS_2) and tungsten disulfide (WS_2) films on a 3-inch diameter silicon wafer, coated with a SiO_2 layer, in the PARADIM facilities MOCVD lab, and refining the growth recipes to find the best parameters for high-quality uniform monolayer growth of the TMD films. Our initial goal was to optimize MoS_2 and WS_2 growth recipes to grow continuous monolayer polycrystalline films on a 3-inch silicon wafer, with 5-10 micron-sized grains, by manipulating the precursor materials and growth conditions on in-house built MOCVD reactors. We characterized our TMD films using Raman spectroscopy and scanning electron microscope (SEM) imaging to confirm a continuous monolayer film with the desired grain size. We optimized the growth recipes for monolayer WS_2 films with > 4 micron-sized grains but with sparse continuity and monolayer MoS_2 films with continuous ~ 2 micron-sized grains.

Summary of Research:

Monolayer polycrystalline MoS_2 and WS_2 films were grown on 3-inch diameter silicon wafers, each in a designated MOCVD reactor system in the PARADIM facility. These two systems were clones of the systems built by Jiwoong Park at the University of Chicago. Our MOCVD reactors consisted mainly of a 4.3-inch diameter hot-wall quartz tube inside of a three-zone tube furnace with the inlet pipe connected to the precursor sources, with their flow rates individually controlled by respective mass flow controllers (MFCs).

A LabVIEW program was used to set temperatures for each zone in the tube furnace, control the flow rates of the precursors and the amount of time each parameter would run. Molybdenum hexacarbonyl (MHC) and tungsten hexacarbonyl (THC) were used as transition metal gas-phase precursors for the MoS_2 and WS_2 film growths, respectively, and diethyl sulfide (DES) was used as the chalcogen atom gas-phase precursors for both growths.

Argon and hydrogen gas (H_2) were used as carrier gases for both growths. H_2 is necessary to reduce DES and to remove carbonaceous species produced during MOCVD film growth processes [2].

Initially, MoS_2 and WS_2 films were grown on three small silicon wafer pieces with one piece placed within each zone of the tube furnace. A plate of NaCl was also placed within the tube furnace near the inlet, zone 3 of the tube furnace, as a desiccant to dehydrate the precursors entering the furnace [2]. The tube furnace was then pumped down to less than 100 mTorr. For our initial growth, we programed the MOCVD reactors with parameters from growth recipes used at the University of Chicago labs, to reproduce their growth of monolayer MoS_2 and WS_2 films with spatial continuity and 5-10 micron-sized grains. However, the reactors were not exact replicas of each other and the TMD recipes required tuning to produce the same high-quality films in our lab.

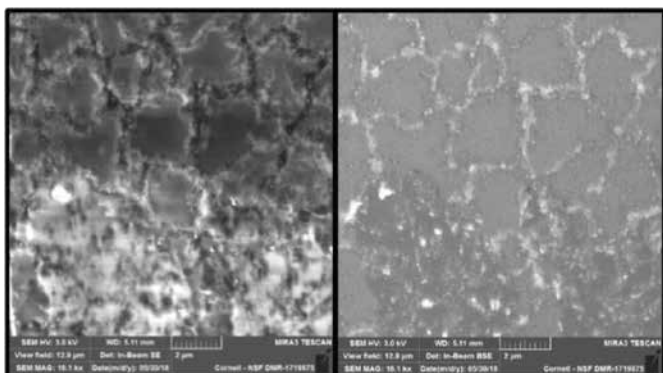


Figure 1: SEM characterization of MOCVD grown MoS_2 film. a, SE image showing film continuity and $> 2 \mu\text{m}$ grain size. b, BSE image of monolayer film.

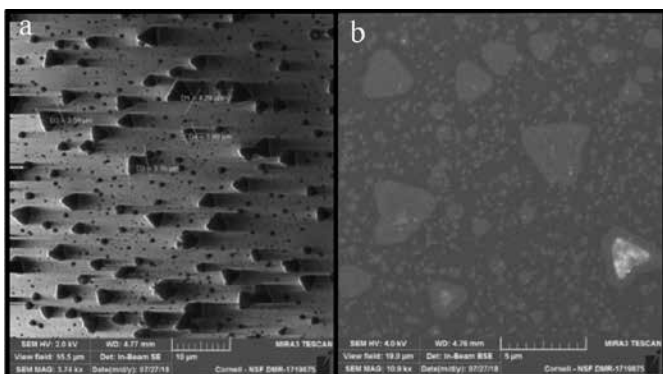


Figure 2: SEM characterization of MOCVD grown WS_2 film. a, SE image showing film topology, $> 4 \mu\text{m}$ grain size. b, BSE image of monolayer grains.

Using the Tescan Mira3 FESEM, in the CCMR facility at Cornell University, we then looked at the topology of our grown TMD films (Figures 1 and 2). If we had sub-micron sized grains, we used the CCMR Renishaw InVia Confocal Raman microscope to characterize the molecular composition of our grown TMD films based on measured Raman spectra (Figure 3) before adjusting our growth parameters. If the SEM images showed us grains greater than a micron but with poor continuity we adjusted our growth parameters based on precedents from the Chicago lab, recent literature, as well as trends we observed from previous runs. We then started a new growth changing one of the films growth parameters; growth time, precursor and carrier gas flow rates, or zone temperature. When we achieved a TMD growth with 5-10 micron-sized grains and adequate continuity, we ran the same recipe on a 3-inch diameter silicon wafer for PARADIM users.

Results and Conclusions:

Our optimized growth recipes for MOCVD grown monolayer TMD films are summarized in Figure 3. Our recipe for WS_2 produced $> 4 \mu\text{m}$ -sized monolayer grains but with sparse grain continuity. The growth recipe for MoS_2 produced a continuous monolayer film with

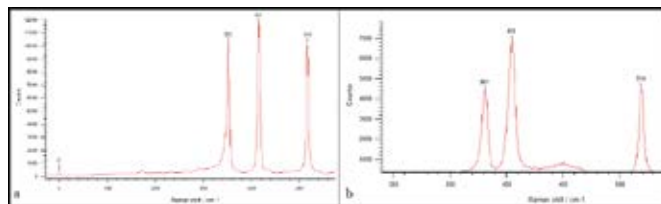


Figure 3: Raman spectrum for PARADIM lab grown TMD films. a, b, molecular identification of WS_2 (a) and MoS_2 (b) films.

Table 1: Optimized MoS_2 and WS_2 growth parameters

	MoS_2	WS_2
Growth time (hrs)	3	6
Transition metal precursor flow rate (sccm)	5	8
Chalcogen precursor flow rate (sccm)	0.4	0.3
Argon flow rate (sccm)	1000	1000
Hydrogen gas flow rate (sccm)	1	1
Furnace temperature: zone 1 ($^{\circ}\text{C}$)	650	650
Furnace temperature: zone 2 ($^{\circ}\text{C}$)	650	650
Furnace temperature: zone 3 ($^{\circ}\text{C}$)	550	550

Figure 4: Optimized growth recipes for monolayer MoS_2 and WS_2 film growth.

$\sim 2 \mu\text{m}$ -sized grains (Figure 2). With our optimized parameters, we have the recipe to grow monolayer MoS_2 and WS_2 films for PARADIM users.

Future Work:

The recipes for monolayer MoS_2 and WS_2 films will continue to be refined, as well as the growth recipes for other monolayer TMD films including molybdenum diselenide (MoSe_2) and tungsten diselenide (WSe_2) to synthesize nanosheets with grain boundaries $< 200 \text{ nm}$ in width and grains $> 5 \mu\text{m}$ in diameter. The optimized parameters will then be used to grow monolayer TMDs on oxides in the MBE-ARPES-MOCVD system being developed at the PARADIM facility to study TMD heterostructures and new physics and applications at the interfaces of 2D TMD and oxide materials.

Acknowledgements:

I would like to thank my mentor, Mr. Don Werder, my PI, Dr. Darrell Schlom, and the REU program coordinators, especially Dr. Julie Nucci, for their support and coaching throughout my research experience. Support for PARADIM is provided under NSF grant DMR-1539918 as part of the Materials Innovation Platform Program.

References:

- [1] Wonbong Choi. Recent development of two-dimensional transition metal dichalcogenides and their applications. *Materials Today*, 20, 116-130 (2017).
- [2] Kibum Kang. High-mobility three-atom-thick semiconducting films with wafer-scale homogeneity. *Nature*, 520, 656-660 (2015).

On Chip Production of GM1 for the Treatment of Huntington's Disease

Regina Mannino, 2018 KEP Intern

Chemical Engineering, Franciscan University of Steubenville

Program: 2018 Keeping the Ezra Promise (KEP) Program

KEP Principal Investigator: Professor Susan Daniel, Robert Frederick Smith School of Chemical and Biomolecular Engineering, Cornell University

KEP Mentor: Ferra Pinnock, Robert Frederick Smith School of Chemical and Biomolecular Engineering

Primary Source of KEP Funding: Keeping the Ezra Promise (KEP), Robert Frederick Smith School of Chemical and Biomolecular Engineering, Cornell University

Contact: ginamannino2@gmail.com, sd386@cornell.edu, fkp22@cornell.edu

Website: http://www.cnf.cornell.edu/cnf_2018reu.html

Abstract:

Huntington's Disease (HD) is a neurodegenerative disorder that causes physical, behavioral, and cognitive deterioration. This disease stems from a mutation in the Huntington protein that depletes levels of an essential glycolipid, ganglioside GM1. While there is currently no cure for HD, mouse model studies have shown that restoring levels of GM1 can slow and possibly halt symptoms of HD. However, GM1 is challenging to synthesize and costly to extract from brain tissue. Therefore, this study seeks to produce GM1 *ex vivo* using a microfluidic device. To advance this goal, the biosynthetic pathway that converts the ganglioside GM3 to ganglioside GM1 was mimicked in a single pot reaction, and a method that quickly identifies the reaction products was developed. The primary identification technique used was Thin Layer Chromatography (TLC). The initial lab protocol was optimized to give results with more distinct separation. Total internal reflection fluorescence microscopy (TIRFM) was also used to characterize the reaction products. This method leveraged the interactions between azide-linked sugars and a cycloalkyne fluorophore, dibenzocyclooctyne (DBCO) to fluorescently label and detect GM1 products.

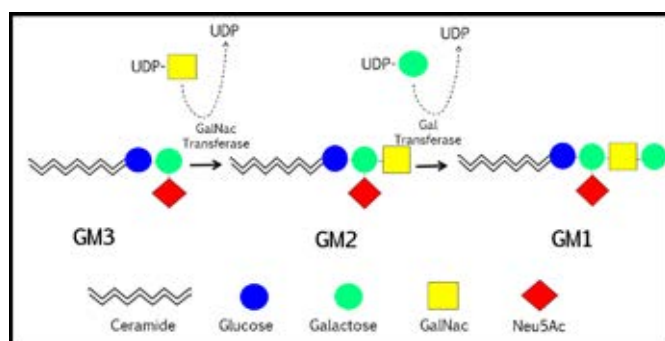


Figure 1: Biosynthetic pathway to ganglioside GM1 from ganglioside GM3.

Summary of Research:

GM1 is a promising therapeutic for HD. However, difficult synthesis and expensive extraction from native tissue have prevented clinical application of GM1. This project seeks to simplify the preparation of GM1- by mimicking its biosynthesis from ganglioside GM3, in a microfluidic device. During this biosynthetic pathway, GM3 undergoes two glycosylation reactions to produce

GM1 (Figure 1). The first stages of this project aimed to replicate the GM3-to-GM1 reaction sequence using a single-pot approach. This required the development of a quick and reliable way to determine the success of the reaction before the project could proceed.

The first technique used to characterize the products of the GM3-to-GM1 reaction was thin layer chromatography (TLC). The goal was to design a protocol that would consistently and distinctively separate GM3, GM1, and GM2 intermediates. In the initial TLC protocol, samples were suspended in methanol and the TLC plate was developed in a running solvent with chloroform/methanol/0.2% aqueous calcium chloride (55:45:10, v/v/v) (Figure 2A). This protocol failed to separate the reaction products, and it was altered by varying ratio of the running solvent. During TLC trials, samples were either suspended in methanol or in a 50/50 mixture of chloroform and methanol. Pure, commercial samples of GM3 and GM1 were used to test the altered TLC protocol (Figure 2). Protocols that provided clear separation were then used to analyze the products of the GM3-to-GM1 single-pot reaction.

The second method used to characterize the reaction products was total internal reflection fluorescence microscopy (TIRFM). TIRFM can selectively illuminate and excite fluorophores at the surface of a supported lipid bilayer (SLB), and thus, could be used to confirm the presence of fluorescently labeled GM1 in a SLB. To do so, GM3 lipids were placed into an SLB and underwent reactions with normal GalNac sugars and special galactose (gal) sugars carrying azide groups.

After the reaction, the azido-gal sugars that attached to glycolipids could couple with the cycloalkyne fluorophore, DBCO, to fluorescently label ganglioside products in the SLB. Since the gal sugar is the second sugar addition (Figure 1), fluorescent tags should only attach to GM1 products. The fluorescent signals in the SLBs were measured under the TIRF microscope and analyzed with ImageJ software [2].

Results and Conclusions:

The best TLC protocol use a running solvent with chloroform/methanol/0.22% aqueous calcium chloride (60:40:10, v/v/v). The samples were suspended in 50/50 chloroform and methanol. This protocol showed clear separation between GM1, GM2 intermediates, and GM3 (Figure 3). The average fluorescence intensity measured for each sample is reported in Figure 4. The results show that the target reaction in it, had the highest fluorescence intensity whereas the various controls had significantly lower intensities. This suggests that some GM1 was produced in the reaction and that its production can be detected by this method.

Future Work:

The improved TLC protocol and the TIRF experiments will be used to rapidly analyze the products of the GM3-to-GM1 reactions performed in the next phase of the project. Additionally, other methods such as high-performance liquid chromatography (HPLC) and mass spectrometry can be considered for further identifying products.

Acknowledgements:

Special thanks to Professor Susan Daniel for allowing me to work in her lab this summer, my mentor Ferra Pinnock, and all the members of the Daniel Research Lab. My internship was funded by the "Keeping Ezra's Promise" Program through the Robert Frederick Smith School of Chemical and Biomolecular Engineering.

References:

- [1] Di Pardo A, et al. Proc. Natl Acad. Sci. U.S.A. 2012, 109, 3528.3533.
- [2] Schneider, C. A.; Rasband, W. S., and Eliceiri, K. W. Nat. Meth. 2012, 9, 671.675.

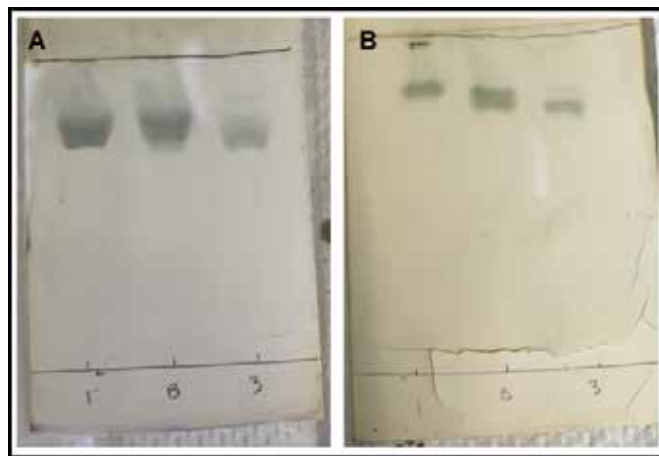


Figure 2: Early TLC plate tests. Figure 2A shows the initial TLC protocol. Figure 2B shows an improved protocol using a running solvent with chloroform/methanol/0.2% aqueous calcium chloride (60:40:10, v/v/v). All samples were suspended in methanol. For each plate, GM1 is spotted on the left, GM3 is spotted on the right, and there is a spot with both in the middle.



Figure 3: A TLC plate with the improved protocol. The top marks are likely other sugars or impurities. Columns 1 and 9 show GM1. Column 5 roughly indicates where GM3 is located. The remaining columns are GM2 intermediates.

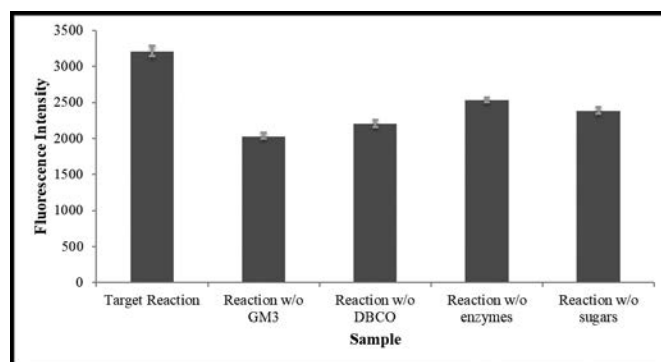


Figure 4: A comparison of the average fluorescence intensities of the SLB samples from the TIRF experiment. The first column has the target reaction. The other columns are controls used to determine the amount of background fluorescence or non-specific binding of DBCO.

Growing and Designing 2D Transition Metal Dichalcogenide (2D-TMDC) Materials for PARADIM Users

Marcus Marracci, 2018 PARADIM REU Intern

B.S. Chemistry, California State University, Fullerton

REU Program: 2018 Platform for the Accelerated Realization, Analysis, and Discovery of Interface Materials Research Experience for Undergraduates (PARADIM REU) Program

PARADIM REU Principal Investigator: Dr. Darrell Schlom, Materials Science and Engineering, Cornell University

PARADIM REU Mentor: Dr. Betül Pamuk, Materials Science and Engineering, Cornell University;
Mr. Don Werder, Cornell Center for Materials Research, Cornell University

Primary Source of PARADIM REU Funding: Support for PARADIM is provided under NSF Grant # DMR-1539918 as part of the Materials Innovation Platform Program

Contact: marcusmarracci@csu.fullerton.edu, schlom@cornell.edu, betul.pamuk@cornell.edu, djw326@cornell.edu

Websites: <http://paradim.cornell.edu/education>, http://www.cnf.cornell.edu/cnf_2018reu.html

Abstract:

Two-dimensional transition metal dichalcogenides (2D-TMDs) were grown using the metal-organic chemical vapor deposition (MOCVD) method. MoS_2 and WS_2 monolayers were grown with 100-200 nm and 2-4 μm grains respectively, and near-full coverage over a three-inch wafer. MoS_2 , MoSe_2 , WS_2 , and WSe_2 were simulated using density functional theory (DFT) in bulk, bilayer and monolayer structures. Raman active modes were identified and compared with literature and experiment with differences under 10 cm^{-1} . Electronic band structures were calculated for MoS_2 , MoSe_2 , WS_2 , and WSe_2 monolayers with band gaps of 1.8, 1.6, 1.8, 1.6 eV with indirect to direct band gap transitions observed between bulk and monolayers for all materials except WSe_2 .

Research Summary:

2D-TMDs have unique properties that have applications in piezoelectronics, photovoltaics, valleytronics, modern electronics, and optoelectronics [1]. Study into these materials can further advance several devices such as solar cells and field effect transistors. The layers in bulk are held together by van der Waals forces and can be separated using the exfoliation method producing micron-scale samples [2]. MOCVD was used to grow 2D-TMDs such as MoS_2 and WS_2 on three-inch silicon wafers. The scalable growth of 2D-TMDs can produce samples to be studied by PARADIM users and advance the development of new devices.

MoS_2 and WS_2 were grown using MOCVD on a silicon substrate with a 250 nm coating of SiO_2 . The starting parameters were provided by Dr. Jiwoong Park [1] and varied until near-uniform coverage and large grains were obtained. Figure 1 shows the parameters which yielded 100-200 nm grains for MoS_2 , 2-4 μm grains for WS_2 , and near-uniform coverage for both samples. SEM

	Ar Flow (sccm)	H ₂ Flow (sccm)	Metal Source (sccm)	Chalcogen Source (sccm)	Temp Zone 1/2/3 (°C)	Time (hrs)
MoS_2	1000	1	5	0.4	650/650/550	3.5
WS_2	1000	1	8	0.3	650/650/550	6
Lattice Constants (Å)	a Ref[7]	a (calculated)	c Ref[7]	c (calculated)		
MoS_2 (Ref[7],24000)	3.150	3.139	12.300	12.542		
MoSe_2 (Ref[7],16948)	3.290	3.269	12.930	13.115		
WS_2 (Ref[7],651387)	3.1530	3.146	12.323	12.656		
WSe_2 (Ref[7],652170)	3.282	3.273	12.960	13.222		

Figure 1: MOCVD growth parameters and lattice constants of bulk TMDs comparing DFT calculations with literature.

was used, on the Tescan Mira3 FESEM in the Cornell Center for Materials Research (CCMR), to determine degree of coverage and grain size, shown in Figure 2 for WS_2 .

Raman spectroscopy was used to check chemical purity of the samples. Figure 3 shows a spectrum of WS_2 , obtained using the Renishaw InVia Confocal Raman microscope in the CCMR, which agrees with literature [1] and DFT calculations within 10 cm^{-1} with peaks at 353 and 417 cm^{-1} .

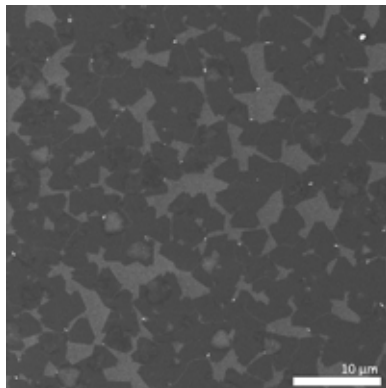


Figure 2: Secondary electron SEM of WS_2 showing near-full coverage of a silicon wafer with 2-4 μm grains.

Properties of MoS_2 , $MoSe_2$, WS_2 , and WSe_2 were simulated using DFT within the framework of the VASP package [3,4], which uses a plane-wave basis set to describe the valence-electron wave function and charge density [5] and Perdew-Burke-Ernzerhof revised for solids (PBEsol) was used for the exchange-correlation functional and the projector augmented wave pseudopotentials [6].

Initial structures for bulk materials were found on the Inorganic Crystal Structure Database (ICSD) [7]. The electronic energy was converged with a tolerance of 10^{-6} eV , the forces on the atoms were calculated, the atomic positions adjusted, and this two-step cycle repeated until the forces converged with a tolerance of $10^{-4}\text{ eV}/\text{\AA}$. The lattice constants of the bulk structures are summarized in Figure 1. Monolayers and bilayers were constructed by increasing the out-of-plane lattice constant from bulk to approximately 25 \AA , keeping n layers in a unit cell, $n = 1$ for monolayers and $n = 2$ for bilayers.

The lattice parameters were held constant and the atomic positions were relaxed with an electronic momentum mesh of $8 \times 8 \times 2$ for sulfides and $12 \times 12 \times 2$ for selenides. Differences in bond lengths and angles were analyzed between bulk, bilayer, and monolayer which were less than 1 m\AA and 1° .

Vibrational modes were calculated using relaxed structures and a $4 \times 4 \times 2$ electronic momentum mesh. Figure 3 shows the Raman active vibrational modes plotted on top of the experimentally obtained Raman

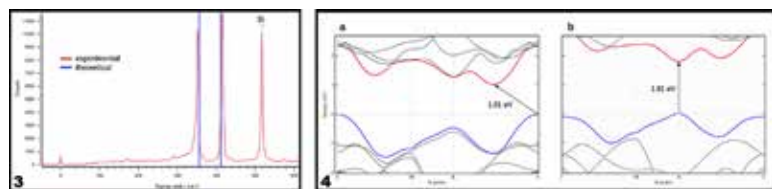


Figure 3, left: Raman spectra of WS_2 and Raman active vibrational modes calculated using DFT. Figure 4, right: Electronic band structure diagram of WS_2 in bulk, 4a, and a monolayer, 4b.

spectrum of WS_2 . The calculated modes are found at 354 and 416 cm^{-1} , which agree with literature and experiment within 10 cm^{-1} [1].

The electronic band structure was obtained by calculating the energy at each point in a $4 \times 4 \times 2$ electronic momentum mesh and mapping out a path between symmetry points [8]. The band gaps of MoS_2 , $MoSe_2$, and WSe_2 monolayers were 1.8 , 1.6 , and 1.6 eV , which agree with experimental values within 0.1 eV . The calculation for a WS_2 monolayer is underestimated by approximately 0.3 eV with a band gap of 1.8 eV [2]. In MoS_2 , $MoSe_2$, and WS_2 an indirect to direct band gap transition is observed between bulk and monolayer, but for WSe_2 , the band gap remains indirect.

In summary, MoS_2 and WS_2 were grown with the MOCVD method and characterized by Raman spectroscopy and SEM. DFT was used to calculate lattice constants, vibrational modes, and electronic band structure. In the future, MoS_2 and WS_2 MOCVD parameters need to be adjusted to increase grain size and reduce bilayer growth, additionally, $MoSe_2$ and WSe_2 will be grown. More rigorous calculations could be performed by including spin-orbit coupling to get more accurate electronic band structures and phonon modes, potentially giving insight into the unexpected indirect band gap in WSe_2 monolayers.

Acknowledgements:

Support for PARADIM is provided under the NSF grant DMR-1539918 as part of the Materials Innovation Platform Program. Facilities for MOCVD were supplied by the Platform for the Accelerated Realization of, Analysis & Discovery of Interface Materials (PARADIM). SEM and Raman microscopes supplied by the CCMR. Calculations using DFT were performed on the TARDIS computing cluster provided by the Cornell University Center for Advanced Computing (CAC), with access given by Dr. Craig Fennie.

References:

- [1] Kang, Kibum, et al., Nature, 520, 7549 (2015).
- [2] W. Choi, et al., Mater. Today, (2017).
- [3] G. Kresse and J. Hafner, Phys. Rev. B, 47, 558 (1993).
- [4] G. Kresse and D. Joubert, Phys. Rev. B, 59, 1758 (1999).
- [5] Brumme, T., et al., Physical Review B, 91, 15 (2015).
- [6] J. P. Perdew, et al., Phys. Rev. Lett. 100, 136406 (2008).
- [7] FIZ Karlsruhe. (n.d.). ICSD News. Retrieved from http://www2.fiz-karlsruhe.de/icsd_home.html, 24000(MoS_2), 16948($MoSe_2$), 651387(WS_2), 652170(WSe_2).
- [8] Y. Hinuma, et al. Comp. Mat. Sci. 128, 140 (2017).

STM Observation and Manipulation of Dimethyl Indolino Benzo-Nitrile (IBN) Molecules on Au <111> Surfaces

Paola Perez, 2018 CNF iREU Intern

Electrical and Computer Engineering Department, University of Texas at El Paso

REU Program: 2018 Cornell NanoScale Facility International Research Experience for Undergraduates (CNF iREU) Program at the National Institute of Material Science (NIMS), Tsukuba, Ibaraki, Japan

CNF iREU Principal Investigator & Mentor: Dr. Keisuke Sagisaka, Nanomechanics Group, Research Center for Advanced Measurement and Characterization, NIMS

Primary Source of CNF iREU Funding: National Science Foundation under Grant No. OISE-1559368

Contact: paperez5@miners.utep.edu, sagisaka.keisuke@nims.go.jp

Website: http://www.cnf.cornell.edu/cnf_2018reu.html

Abstract:

Controlling and understanding the structure and conformation change of a dimethyl indolino benzo nitrile (IBN) single molecule is key to fabricating molecular machines for future applications. A scanning tunneling microscope is used to conduct an atomic study of IBN molecules on an Au<111> surface. In this study, a scanning tunneling microscopy (STM) machine is used to image molecules in real space, give 3D profile of the surface, manipulate molecules to obtain spectroscopic data, and characterize molecular arrangements on the surface. Different alignments were observed depending on molecular coverage. Single molecules were able to be controllably moved and rotated after high-bias application. Additionally, excitation voltages of a single molecule were found at 10, 20, 40, and 80 pA currents.

Introduction:

Molecular manipulation with STM has gained greater attention since the Nobel Prize in Chemistry 2016 awarded to Jean-Pierre Sauvage, Sir J. Fraser Stoddart, and Bernard L. Feringa “for the design and synthesis of molecular machines” [1]. Molecular machines have potential applications in drug delivery, electrical sensors, actuators, energy storing devices, among others. Molecular manipulation is usually achieved by stimulants such as light, current, force, and magnetic field in solutions. We make use of tunneling current injected from an STM tip to analyze the IBN molecule that has particularly been synthesized for the study of molecular conformation manipulation on a solid surface.

Materials and Methods:

A low temperature, ultra-high vacuum STM was used to control single IBN molecules, analyze its properties in the atomic scale, and characterize molecular arrangements on a gold surface. The Au<111> surface used was cleaned through sputtering and annealing at 550°C. Then, IBN molecule was evaporated from a crucible at ~ 58°C on a room temperature substrate. STM imaging was done with a platinum-iridium alloy tip at low temperatures to reduce noise, suppress molecule diffusion, and minimize image drift. Deposition rate was controlled by temperature of the crucible and pressure in the deposition chamber. Molecular coverage was controlled by deposition time. Changing the parameters allows for different molecular motion and electronic properties.

Results and Discussion:

Figure 1 shows three STM images captured in constant-current mode. Different alignments were observed depending on molecular coverage (affected by pressure, temperature, and deposition time parameters). Figure 1(a) shows an STM image of one monolayer of IBN molecule covering the whole surface. The herringbone patterns of the gold surface are slightly visible through the molecular layer. This indicates that IBN molecules are weakly bonded to the surface. Figure 1(b) shows an STM image of 0.338 monolayers of IBN after decreasing the temperature and deposition time. The molecule showed organized line alignments and started forming clusters on the surface. Figure 1(c) shows 0.036 monolayers of IBN after decreasing the parameters even further. For this coverage, the molecule only formed clusters, mainly made of three or four single molecules. In order to understand the conformation change property of the single IBN molecule, further analysis was mainly done with low coverage deposition.

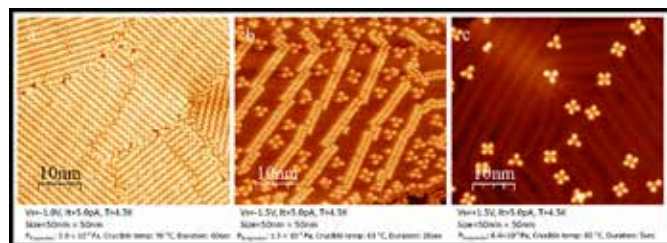


Figure 1: IBN coverages and alignments: (a) 1 monolayer, (b) 0.338 monolayer, and (c) 0.036 monolayer.

Prior to molecule manipulation, the molecule clusters were broken to separate a single IBN through the application of high bias voltages (Figure 2). After breaking the molecule clusters, a single IBN molecule was controllably isolated using tip-molecule interaction with high current for further analysis. The breaking of the clusters also helps identify molecular orientation. High bias voltage (typically 2.2 ~ 2.4 V at 5pA) was applied to the single molecule to observe that the tip height over the molecule switched between two slightly different states. We believe that this corresponds to molecular conformation changes, but the excited state (lower height state) was not successfully imaged by the STM due to instability of this state. In contrast, higher bias voltage (typically > 2.4 V at 5 pA) was able to rotate and move the single molecule across the surface as shown in Figure 3(a). Excitation voltages were found for the single molecule at different currents. This was done at 10, 20, 40, and 80 pA currents. Fig.3(b) shows that excitation voltage decreased as current increased.

Figure 4 shows the molecule's structure model and electrostatic potential map. Electrostatic calculations showed that the IBN molecule has a total neutral charge. However, it also has slight internal polarity. The slightly positive side (blue) and a slightly negative side (yellow) makes IBN a dipole. For the full coverage deposition, the molecule aligns in a conventional + - way. On the other hand, for low coverage deposition, the clusters show different, very interesting phenomena. The clusters don't follow the + - convention, but instead, have all the negative sides connected in the middle. Therefore, we hypothesize that there must be something in the middle holding the clusters together. The hypothesis is that a gold atom acts as a mediator to allow molecule clustering. This is because deposition is done in a room temperature substrate at which the IBN molecules easily diffuse over the gold surface to pick up gold atoms, possibly from step edges, and the CN functional group in the molecule tends to form strong bonds with gold. However, further testing is needed for confirmation.

Conclusions and Future Work:

In conclusion, the IBN molecule has different alignments depending on coverage, rotation and movement of single molecule is possible, and excitation parameters of a single molecule were found. Future studies consist of testing different molecular coverages, doing atomic force microscopy imaging with a CO tip for identification of the molecule's internal structure, and changing the surface to a different material such as silver or copper for testing with different molecule-surface interactions.

Acknowledgements:

This work was supported by the CNF iREU Program and National Science Foundation grant OISE-1559368. Special thanks to Keisuke Sagisaka, Oscar Custance, Waka Nakanishi, and Lynn Rathbun for all their assistance and guidance.

References:

- [1] The Nobel Prize in Chemistry 2016, <https://www.nobelprize.org/prizes/chemistry/2016/summary/>

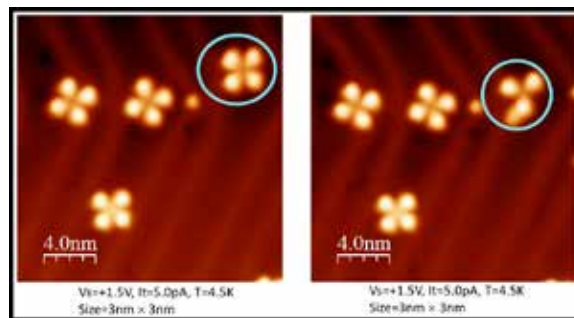


Figure 2: Effect of application of high bias voltages of molecule clusters.

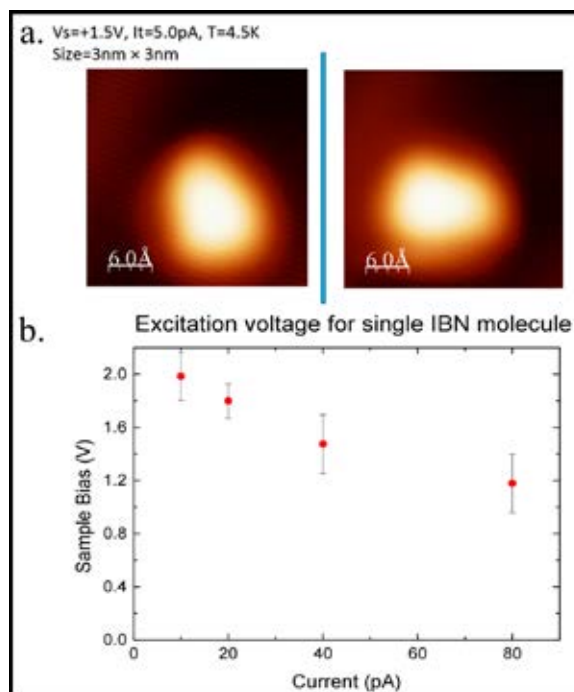


Figure 3: (a) Excitation and manipulation of single IBN molecule with high bias. (b) Excitation voltages for single IBN molecule.

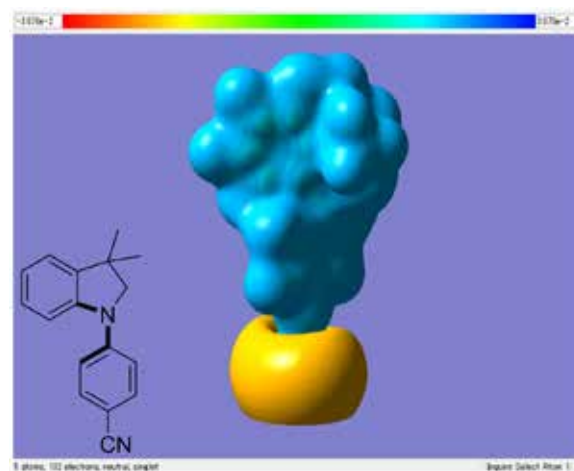


Figure 4: Electrostatic potential map.

Development of Nanoplasmonic Mo-Au Photocatalysts for Ammonia Synthesis

Joshua Romo, 2018 KEP Intern

Chemical Engineering, University of Dayton

Program: 2018 Keeping the Ezra Promise (KEP) Program

KEP Principal Investigator: Prof. Tobias Hanrath, Chemical and Biomolecular Engineering, Cornell University

KEP Mentor: Jéssica Akemi Cimada da Silva, Chemical and Biomolecular Engineering, Cornell University

Primary Source of KEP Funding: Keeping the Ezra Promise (KEP), Robert Frederick Smith School of Chemical and Biomolecular Engineering, Cornell University

Contact: romoj2@udayton.edu, tobias.hanrath@cornell.edu, jessicacimada@gmail.com

Website: http://www.cnf.cornell.edu/cnf_2018reu.html

Abstract:

The development of nanoplasmonic molybdenum-doped gold (Mo-Au) photocatalysts incorporated work on the molecular, lab, and systems level scale. On the molecular scale, Mo-Au nanoparticles (NPs) were synthesized through reaction of Au NPs with molybdenum (V) chloride (MoCl_5) and $(\text{MoS}_2)_2^{2-}$, respectively. We focused on the synthesis and characterization of Au NPs with $(\text{MoS}_2)_2^{2-}$. The NPs displayed an amorphous shell of $(\text{MoS}_2)_2^{2-}$ around the Au NP as well as a red shift in light absorption. On the lab scale, a reactor was designed and constructed to test the synthesized NPs for their catalytic performance. On the systems level scale, an ASPEN simulation model of an ammonia (NH_3) production process was created to study how pressure and temperature affect utility cost at an industrial scale.

Summary of Research:

The synthesis procedure consisted of two steps: (i) formation of Au NPs and (ii) treatment with Mo. In the first step, Au NPs were synthesized by the addition of a reducing agent, either sodium citrate ($\text{Na}_3\text{C}_6\text{H}_5\text{O}_7$) or sodium borohydride (NaBH_4), to an Au precursor, gold (III) chloride trihydrate ($\text{HAuCl}_4 \cdot 3\text{H}_2\text{O}$). The solution was stirred at 80°C for around one hour. In the second step, Mo precursor, either MoCl_5 or ammonia tetrathiomolybdate ($(\text{NH}_4)_2\text{MoS}_2$), was added to the solution of Au NPs synthesized in step 1. The reaction was kept under stirring at 60°C overnight (> 12 hours).

After each step of the synthesis, the NPs were purified via centrifugation (unless otherwise stated). To determine an optimal synthesis strategy in which total synthesis time is minimized while still obtaining a high-quality product, the reducing agent and number of purification steps were varied. The obtained products were compared using UV-vis spectroscopy and transmission electron microscope (TEM) imaging.

UV-vis spectroscopy was used to verify if the final synthesized NPs retained a plasmonic absorbance in the visible region, which is optimal for harnessing solar energy. TEM imaging was used to make qualitative observations about the NPs' morphology, determine average particle size, and verify crystallography with

electron diffraction (ED). Additionally, energy dispersive spectroscopy (EDS) with a scanning electron microscope (SEM) was used for an elemental analysis of the NPs.

It was determined necessary to design a lab-scale glass reactor to test the catalytic performance of synthesized Mo-Au NPs. Three parameters were important in the design process: maximize (i) reactant-catalyst interaction, (ii) light transmission, and (iii) ease of setup, takedown, and reloading. Adhering to these parameters, multiple designs were explored in collaboration with David Wise, a glass blower in the Chemistry Department. In the lab-scale set-up, mass flow controllers (MFCs) were used to control H_2 and N_2 reactant gas flow. A white LED was used as light source.

To explore a system-level NH_3 production process that can integrate experimental results from the lab-scale reactor system, a computational model was created using ASPEN. A conventional recycle-stream NH_3 production flowsheet was created by following two published tutorials. The published tutorials provided stream cost, utility costs with heating/cooling values, and simple kinetic model for the reactor. Simulations were run at various operating pressures and temperatures to study how they affect utility costs.

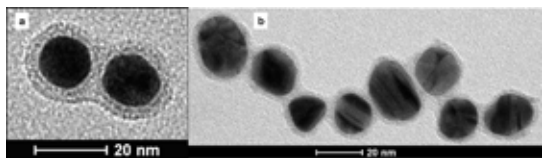


Figure 1: Au NPs with $(\text{MoS}_2)_2^-$ shell from 6-step (a) and 3-step (b) purification method.

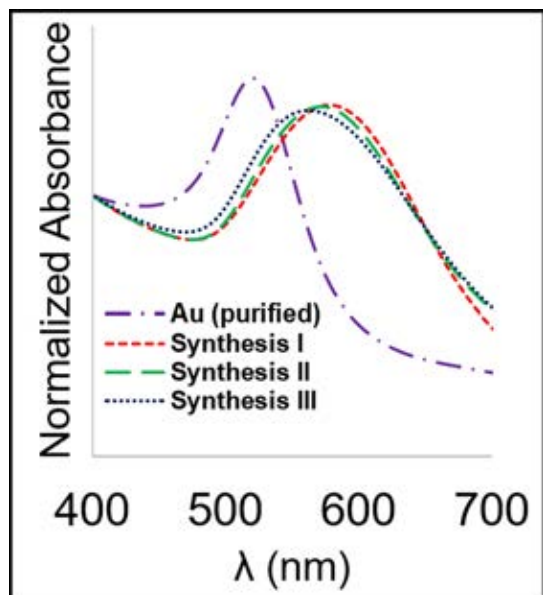


Figure 2: UV-vis of all synthesis methods.

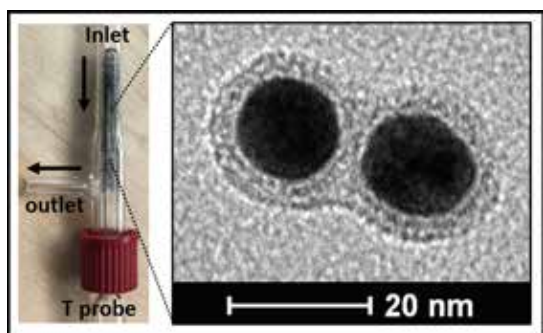


Figure 3: Lab-scale reactor coated with Au-Mo NPs.

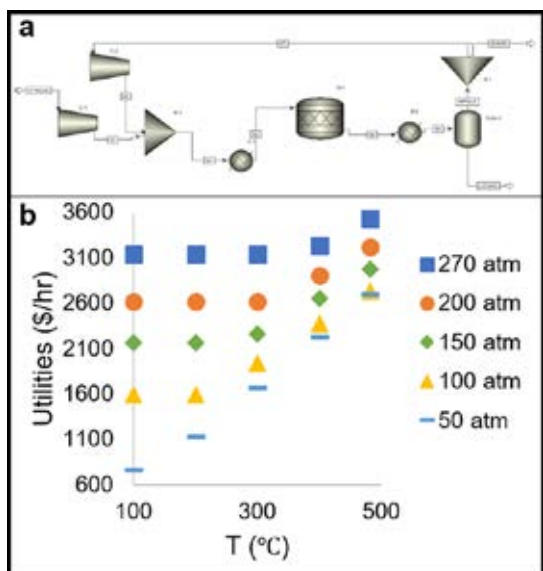


Figure 4: ASPEN model of NH_3 production (a) and utilities cost at various operating conditions (b).

Results and Conclusions:

Due to better chemical bonding of S to Au, we quickly realized that Au NPs coated with a $(\text{MoS}_2)_2^-$ shell was our desired Mo-Au catalyst. The most uniform sample of Mo-Au NPs was obtained using $\text{Na}_3\text{C}_6\text{H}_5\text{O}_7$ and performing three purifications after each step of the synthesis (Figure 1a). Although the purification process adds to the total synthesis time, it minimizes the size distribution of the final particles. However, due to the lengthy synthesis time (five days), we explored omitting the first three purification steps. This resulted in NPs with the Mo-containing shell in only one day (Figure 1b). However, the NPs were not as uniform in size. Therefore, it was concluded that the first purification step is important because it removes excess reducing agent. Thus, the optimal synthesis strategy involved one initial purification step to remove excess $\text{Na}_3\text{C}_6\text{H}_5\text{O}_7$ before adding $(\text{NH}_4)_2\text{MoS}_2$ and performing the final purification process. The total synthesis time for this procedure was about two days. All synthesis strategies produced NPs that showed a plasmonic absorbance in the 550-600 nm region and a red shift from the 521 nm peak of pure Au NPs (Figure 2). Additionally, the synthesized NPs were observed to aggregate while in solution over a period of days after having been synthesized, which is characteristic of plasmonic peak broadening and color change.

A 5 mm diameter quartz glass reactor that fulfilled all three design parameters was constructed. The “screw-top” design made it easy to coat the outside of the quartz thermocouple well and “screw-in” into position (Figure 3). When testing is complete, the reactor can simply be unscrewed, washed, re-coated, and reloaded. The outlet stem fed directly into an NH_3 gas detector. The created ASPEN model was used to generate a general relationship between operating conditions (P,T) and utility cost (Figure 4).

Future Work:

Using the optimized synthesis procedure, batches of Mo-Au NPs will be synthesized with varying concentrations of $(\text{MoS}_2)_2^-$. The catalytic activity of the NPs will be tested in the lab-scale reactor system. The lab-scale results will be used to inform a kinetic model and operating conditions that more accurately describe our novel photocatalytic process. The model will be used to compare the energetics and cost of conventional and novel NH_3 production processes.

Acknowledgements:

Hanrath Energy Lab; Funding provided by Keeping the Ezra Promise (KEP) Program, Robert Frederick Smith School of Chemical and Biomolecular Engineering, Cornell University.

References:

- [1] Polte, et al. “Mechanism of Gold Nanoparticle Formation in the Classical Citrate Synthesis Method Derived from Coupled *in situ* XANES and SAXS Evaluation.” *J. of the American Chemical Society*, 132 (4), 1296-1301 (2010).
- [2] Anna Lavie, et al. “Synthesis of core shell single-layer MoS_2 sheathing gold nanoparticles, $\text{AuNP}@1\text{L-MoS}_2$.” *Nanotechnology*, 28, 24LT03 (2017).
- [3] “Ammonia Synthesis with Aspen Plus® V8.0.” <https://lms.nchu.edu.tw/sysdata/doc/1/196bb4d4fac4c3d7/pdf.pdf> Revised Oct 18, 2012.

Characterization of Magnetic Thin Films for Actuating Origami Devices

Sierra Russell, 2018 CNF REU Intern

**Nanoscale Engineering & Applied Mathematics,
SUNY Polytechnic Institute – Colleges of Nanoscale Science & Engineering**

REU Program: 2018 Cornell NanoScale Science & Technology Facility Research Experience for Undergraduates Program

CNF REU Principal Investigator: Professor Paul McEuen, Department of Physics, Cornell University

CNF REU Mentor: Tanner Pearson, School of Applied and Engineering Physics, Cornell University

Primary Source of CNF REU Funding: National Science Foundation via the National Nanotechnology Coordinated Infrastructure (NNCI) Grant No. NNCI-1542081

Contact: srussell@sunypoly.edu, plm23@cornell.edu, tgp34@cornell.edu

Website: http://www.cnf.cornell.edu/cnf_2018reu.html

Abstract:

Fabrication inspired by origami offers a novel method for the development of micron-scale machines, which have a wide range of potential applications. The use of magnetic thin films in tandem with ultra-thin atomic layer deposition (ALD) films allows for the creation of actuatable devices that can be controlled with external magnetic torques. We characterized cobalt, nickel, and iron films to compare their viability for these devices. We deposited our films via electron-beam evaporation at thicknesses of 25 nm and 50 nm and deposition rates of 0.3 Å/s and 0.6 Å/s, on top of a 10 nm thick titanium adhesion layer. We performed stress measurements of each film pre-and post-deposition, as well as thickness verification. We obtained the hysteresis curve of each film by using a vibrating sample magnetometer (VSM). We see that Fe and Co have significantly higher magnetizations than Ni, whereas Ni benefits from having the lowest stress. We also showed that the addition of a low stress polymer (SU-8) spun on top of the magnetic films may help to reduce the stress in the composite film. We discuss the implications of these results for our origami-inspired devices.

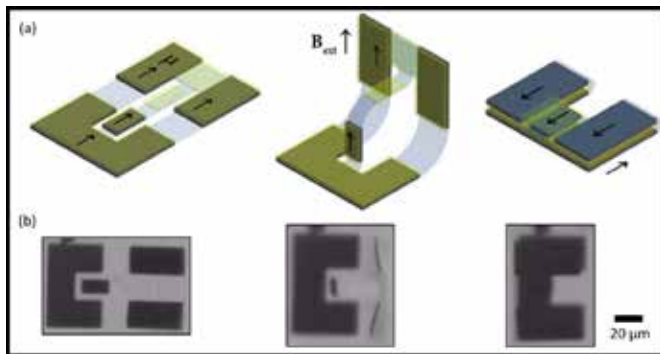


Figure 1: (a) Schematic and (b) optical image of 2D-to-3D magnetically actuated device with latching mechanism — μ represents the magnetic moment and B_{ext} the external magnetic field.

Summary of Research:

The goal of this work was to determine the viability of different magnetic materials for the fabrication of actuatable micron-scale devices. These devices, composed of a flexible ALD backbone and rigid magnetic

panels, can be controlled with external magnetic torques to create three dimensional structures from planar Si-based processing (Figure 1). We measured the stress experienced in the magnetic films, as it imparts curvature on the underlying ultrathin ALD films and alters their bending energies. We also studied the magnetic properties of the magnetic films. These include the magnetization saturation, which relates to the magnitude of the magnetic torques we can apply, and the coercive field, which is the field required to orient the magnetic moment of the film along a given axis.

We characterized three magnetic materials: cobalt, nickel, and iron. The materials were deposited via electron-beam evaporation. A 10 nm thick titanium layer was deposited prior to any magnetic films to promote adhesion to the wafer. Each material was deposited at 25 nm and 50 nm with deposition rates of 0.3 Å/s. Additionally, we deposited 50 nm of Co at a deposition rate of 0.6 Å/s to determine the effect on the stress. Once the films were deposited, the thickness was verified using a profilometer.



Figure 2: Bow of two wafers before and after deposition to compare the change in stress with the addition of SU-8 photoresist.

Stress measurements were taken with the FlexUs film stress measurement tool. This tool measures the bow of the wafer before and after deposition. Then it relates the change in the bow with the properties of the deposited material to determine the stress in the film. To see the influence a low stress polymer has on the overall stress in a film, 70 nm of Co was deposited on two wafers in parallel, followed by spinning 1 μm of SU-8 photoresist on one wafer (Figure 2).

Samples from each thickness of each material were put through a VSM to determine their saturated magnetizations and coercivities. The data produced by the tool provides the magnetic moment as a function of the magnetic field. We normalized the magnetic moments by the volumes of the respective films to determine their magnetizations.

Results and Conclusions:

We found that Fe films have the largest amount of stress, with both the 25 nm and 50 nm thick samples having an average stress of 820 ± 14.9 MPa. The Co films had an average stress of 400 ± 19.9 MPa, and the Ni films had an average stress of 170 ± 12.0 MPa. In the case of Co, increasing the deposition rate from 0.3 \AA/s to 0.6 \AA/s didn't impact the stress in the film. Moreover, the addition of the SU-8 on top of the Co film did reduce the stress in the total film by approximately 90%.

The VSM data showed that Fe has the largest coercive field and magnetization saturation, while Co

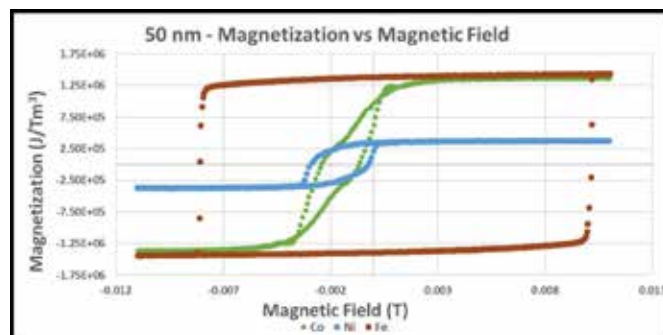


Figure 3: Magnetic hysteresis curves of 50 nm thick Co, Fe, and Ni.

has the lowest coercive field and Ni has the lowest magnetization saturation (Figure 3). The 25 nm and 50 nm samples showed similar magnetization saturations, but the coercive fields tended to increase with increasing thickness. However, we didn't expect to see Ni having a larger coercive field than Co, since Ni is considered a softer magnetic material. We think this could be due to possibly depositing oxide during our Co deposition, instead of pure Co.

We've shown that Co and Fe films have much greater stresses than Ni films, which makes them more of a risk to use as they're more likely to impact the stiffness of the ALD films in our devices. Ni films are much weaker magnets than Co and Fe films; therefore, we wouldn't be able to apply as strong of magnetic torques. To balance these factors, we can use SU-8 to reduce the stress in Co and Fe, resulting in films with both low stress and high magnetization that maximize device performance. The next steps for this project are to investigate more magnetic materials, such as magnetic alloys, and different methods of deposition.

Acknowledgements:

Thank you to Professor Paul McEuen for taking me on as an intern for this program, and Tanner Pearson for the excellent mentorship throughout the summer. This work was funded by the NNCI NSF (grant no. ECCS-1532081).

Modeling Random Memristive Nanowire Networks

Daniel Teal, 2018 CNF iREU Intern

Mechanical Engineering and Math, UT Austin

REU Program: 2018 Cornell NanoScale Facility International Research Experience for Undergraduates (CNF iREU) Program at the National Institute of Material Science (NIMS), Tsukuba, Ibaraki, Japan

CNF iREU Principal Investigator & Mentor: Dr. Tomonobu Nakayama, MANA, NIMS

Primary Source of CNF iREU Funding: National Science Foundation under Grant No. OISE-1559368

Contact: daniel@teals.org, nakayama.tomonobu@nims.go.jp

Website: http://www.cnf.cornell.edu/cnf_2018reu.html

Abstract:

Nanowires (NWs), micron-scale cylinders with high aspect ratios, are easy to precisely fabricate in many materials and dimensions. Furthermore, the junctions between crossed nanowires may form high-performance transistors, diodes, or other electronic elements. These properties make NWs appealing building blocks for future microelectronics [1]. However, it is difficult to assemble individual NWs into circuits. Thus, we investigate the properties of easier-to-assemble random networks. Here, we study networks of polyvinylpyrrolidone (PVP)-coated Ag (Ag@PVP) nanowires. Modeling junctions as variable resistors, we describe two modes of behavior: sufficient voltage across a network causes current to rise exponentially; in its absence, the network eventually returns to its original state. Experimental measurements support this model for a time decay on the order of weeks. These networks might be used to build ephemeral memories, current switches, or planar memristors.

Summary of Research:

Methods. Although, as aforementioned, it is difficult to manufacture electronics from precisely placed individual components, bottom-up assembled networks have been used to construct structures such as reservoir computers [2]. We investigated Ag@PVP networks in search of similarly useful emergent properties. PVP-coated Ag NWs were formed via a wet chemistry process [3]. NW length varied about 10 μm , NW diameter was on the order of 500 nm, and PVP coated the NWs in a layer single nanometers thick. Au electrodes 10 nm thick and 3 mm apart were sputtered on glass, on top of which were drop-cast NWs in ethanol, as shown in Figure 1, for a density near 0.2 NW/ μm^2 .

Model. It was hard to physically measure the complete internal dynamics of the network. Instead, we constructed a digital simulation that would be verified by simpler physical experiment. We modeled each nanowire as a line segment on a 2D plane, as shown in Figure 1, and marked any intersection between two nanowires as a junction. Electrodes were defined and connected to any overlapping nanowires. The network was treated as a resistive circuit, where a voltage was applied across electrodes, nanowires were zero-resistance wires, and junctions were presumed to be resistive connections between nanowires.

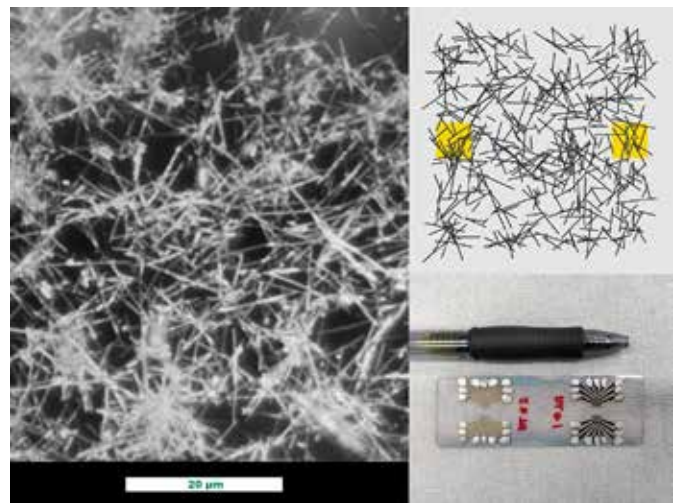


Figure 1: Left, micrograph of an Ag@PVP network. Top right, visualization of a computer-simulated network with two electrodes. Bottom right, Two physical networks with gold electrodes.

The junction model, based on the common linear memristor model and Gimzewski, et al. [2], assumes two nanowires are separated by a thin film of PVP. Any voltage potential between the nanowires drives a small current, which moves Ag ions via electromigration into

the PVP film, forming a low-resistance filament. Thus the junction is an ohmic resistor with a value between low and high states using Equation 1, where w , the width of the filament, varies between zero and w_{\max} , the thickness of the PVP film. In the absence of current, the filament dissolves over time.

We modeled the change of filament width using Equation 2, where μ is an ion mobility constant and τ is a dissolution time constant. When the dissolution state of (2) dominated, the width decreased exponentially with half-life determined by Equation 3, and when significant current instead reinforced the formation term of (2), the junction width increased with positive second derivative and half-life determined by Equation 4.

$$V = \left[\frac{w}{w_{\max}} \cdot R_{on} + \left(1 - \frac{w}{w_{\max}} \right) \cdot R_{off} \right] \cdot I \quad (1)$$

$$\frac{dw}{dt} = \mu \cdot \frac{R_{on}}{w_{\max}} \cdot |I| - \frac{w}{\tau} \quad (2)$$

$$\ln(2) \cdot \tau \quad (3)$$

$$\frac{R_{off} \cdot w_{\max}^2}{2 \cdot \mu \cdot R_{on} \cdot V} \quad (4)$$

Equations 1-4.

Simulation. Using the model, we applied a constant voltage to two electrodes on a 250 NW network. In response, current rose asymptotically, as shown in Figure 2. Eventually, a path of low resistance was formed between the two electrodes. Filament decay may be observed indirectly in the same way by tracking the conductivity of the network under a negligible current flow.

Experiment. The model was supported by physical experiment. 5V applied to electrodes of multiple networks, fabricated as previously described, via a Keithley 4200-SCS system produced the current profiles of Figure 4, which mimic Figure 1. In the same way, a low 1 mV resulted in conductivity decay. Extrapolation measures the decay time constant in weeks.

Conclusions and Future Work:

Experimentally supported computer simulation of random PVP@Ag nanowire networks demonstrated two modes of behavior: an accelerating, internally chaotic rise and an exponential decay. The week-long decay constant and resistive behavior of the physical network discourages real-time reservoir computing. However, such networks could remember data via low-resistance paths for fixed amounts of time (ephemeral memory), use these paths to switch currents between multiple electrodes, or simply serve as sheet memristance. Further study of the networks should be able to improve parameter control. Addition of capacitance may improve dynamics for computational purposes.

Acknowledgements:

The author thanks Dr. Tomonobu Nakayama and the Nano Functionality Integration Group for hosting this project, part of the 2018 iREU Program between CNF and the National Institute of Materials Science (NIMS). Thanks also to organizer Dr. Lynn Rathbun and NSF grant OISE-1559368.

References:

- [1] Lieber, C., Zhang, A., and Zheng, G. (2016). Nanowires. New York, NY: Springer.
- [2] Gimzewski, et al. (2013). Nanotechnology. doi:10.1088/0957-4484/24/38/384004
- [3] Zhang, et al. (2013). Journal of Nanomaterials. doi:10.1155/2013/456098

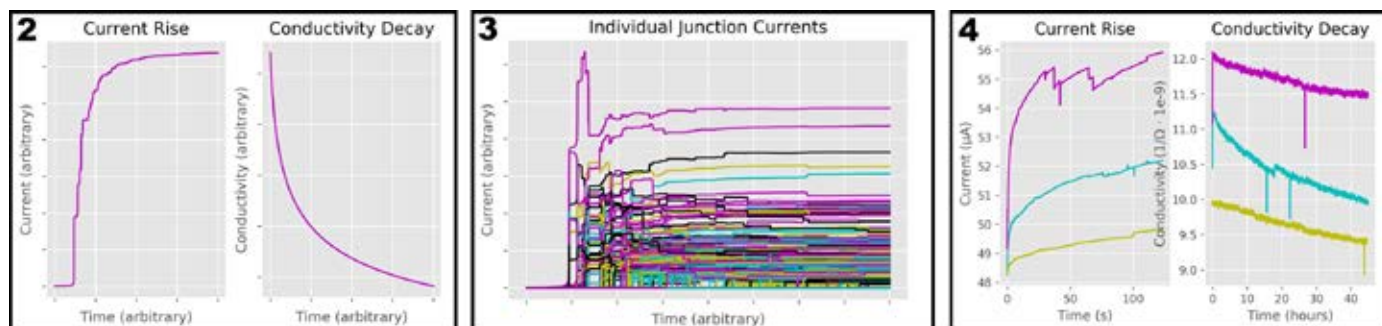


Figure 2, left: Response of the simulated network to a constant voltage with arbitrary units. Left: with high voltage, current rises. Discrete steps mark individual junction filament growth. Right: with negligible voltage and current, network conductivity decreases. **Figure 3, middle:** As current flows through the network, filament growth across a junction increases its individual flow, decreases total network resistance, and triggers a cascade of further growth. **Figure 4, right:** Experimental responses of three Ag@PVP networks to low and high voltage, respectively, analogous to Figure 2. Left: noise is unexplained. Right: data discontinuities are due to experimental errors.

Development of a MEMS Tool to Study the Physics of Water and Ice

Kody Whisnant, 2018 CNF REU Intern

Chemical Engineering, Wayne State University

REU Program: 2018 Cornell NanoScale Science & Technology Facility Research Experience for Undergraduates Program

CNF REU Principal Investigator: Dr. Abraham Stroock, Chemical and Biomolecular Engineering, Cornell University

CNF REU Mentor: Hanwen Lu, Sibley School of Mechanical and Aerospace Engineering, Cornell University

Primary Source of CNF REU Funding: National Science Foundation via the National Nanotechnology Coordinated Infrastructure (NNCI) Grant No. NNCI-1542081

Contact: kody.whisnant@wayne.edu, abe.stroock@cornell.edu, hl943@cornell.edu

Website: http://www.cnf.cornell.edu/cnf_2018reu.html

Abstract:

Freezing of water in confinement is commonly found in geological, biological and architectural contexts. It is believed that the phase equilibrium and crystal formation is influenced by the confinement in pore space, which often has nanoscopic dimensions. The small scale and structural complexity of porous materials hinders our ability to understand the detailed kinetics and phase equilibrium of crystals in confinement. To shed light into this problem, we developed a microelectromechanical systems (MEMS) based porous system consisting of geometrically well-defined high aspect ratio nanochannels with nanoscale (30 nm to 100 nm) channel heights and micron-scale channel width. Such configurations provide a wide field of view (~microns) for direct visualization of crystallization kinetics and phase equilibrium within nanoconfinement. Channels were first fabricated via conventional photolithography techniques on silicon and glass substrates. Notably, a 200 nm silicon nitride layer was deposited via low pressure chemical vapor deposition (LPCVD) underneath the channels to enhance contrast between liquid water and ice. The final channel geometries were verified via capillary condensation within the channels. Finally, we experimentally observed the ice-water interface in nanoconfinement. The melting of confined ice is in quantitative agreement with the Gibb-Thomson relation.

Project Summary:

Introduction. Freezing of water in nanoconfinement is of great importance in geological, biological, and archeological contexts [1,2]. It is believed that the phase equilibrium of water and ice is shifted according to the Gibbs-Thomson relation [3] (Figure 1). However, owing to the small and complex geometrical nature of porous materials, the local phase equilibrium in nanoconfinement remains unresolved. Direct imaging of freezing can provide local mechanistic information on water-ice phase equilibrium and crystallization dynamics under confinement. Herein, we demonstrate the unique opportunity of observing confined phase equilibrium in a MEMS high aspect ratio nanochannel array with in-situ phase contrast enhancement enabled by a Si_3N_4 dielectric mirror [4] (Figure 2).

Fabrication and Experiment. The device fabrication process can be summarized as follows: A LPCVD Si_3N_4 layer of ~ 200 nm thickness was first deposited on a silicon wafer followed by a PECVD layer of silicon oxide with thickness corresponding to the desired channel

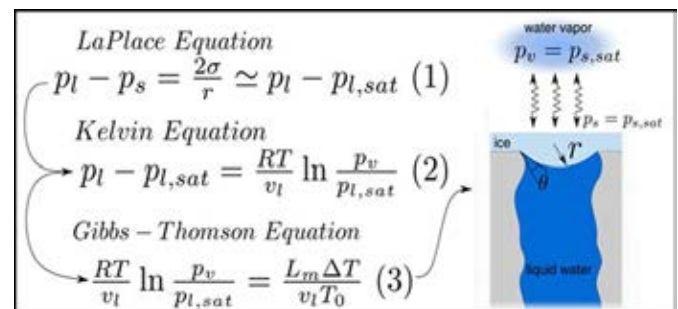


Figure 1: Liquid water in a pore can coexist, metastably, with ice and an unsaturated vapor. Capillarity between liquid and ice (Laplace) places the liquid under tension and allows for phase equilibrium (Kelvin) with the liquid under tension. This equilibrium can be expressed as the Gibbs-Thomson equation.

height. Nanochannel patterns were then transferred and patterned via photolithography. The channels were formed by etching the oxide layer with 30:1 buffered oxide etch (BOE).

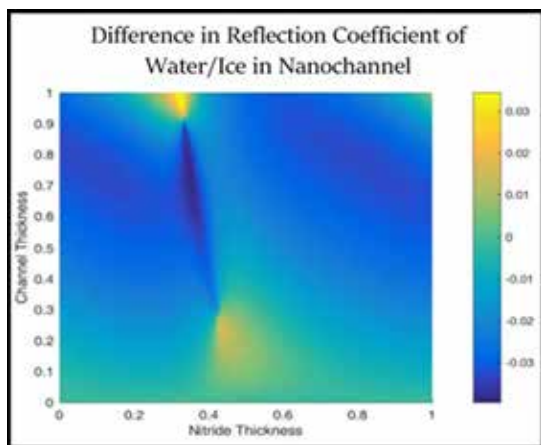


Figure 2: Calculated difference in the reflection coefficient of water and ice in the nanochannels, with axes normalized to incident wavelength. The maximum difference is found with nitride thickness in between 0.4 and 0.5, which for visible light correlates to a nitride thickness of 130 nm-260 nm. This difference is insensitive to channel thickness.

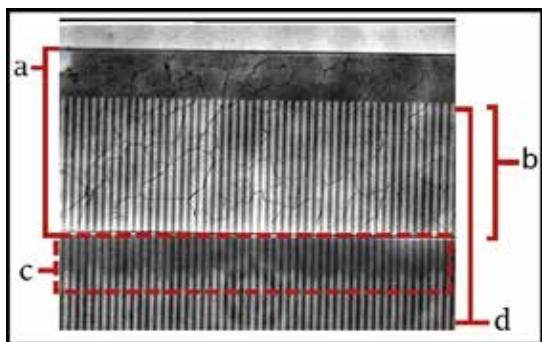


Figure 3: Image obtained from freezing experiment. (a) Microchannel containing bulk ice, identified by the grain boundaries present in image. (b) 500 μm channel overlap. (c) Liquid water in nanochannels (darker region) coexisting with ice (brighter region) at subfreezing temperature. (d) Nanochannel array.

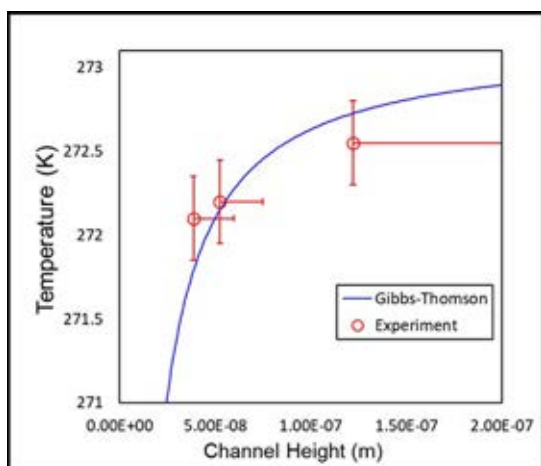


Figure 4: Melting temperatures of ice in nanochannels with different channel heights compared to the Gibbs-Thomson prediction. Values agree with those predicted by the Gibbs-Thomson relation.

For the glass wafer, a 250 nm PECVD amorphous silicon (a-Si) layer was deposited and annealed as an etch mask. Photolithography was then used to transfer the pattern of microchannels. SF_6/O_2 reactive ion etch in the Oxford 80 etcher was used to pattern the a-Si etch mask and the 10 μm microchannels were etched in 49% hydrofluoric acid.

When complete, the patterned silicon and glass wafers were aligned and anodically bonded using the MA6-BA6 contact aligner and SÜSS SB8e substrate bonder. The bonded wafers were diced and microchannel inlets were cut out with the Vaserlaser.

For testing, individual devices were placed in an environmental chamber with pressure and temperature regulation. Water vapor was then pumped through the chamber to fill the nanochannels with liquid water upon capillary condensation, from which the channel height was deduced. The microchannels were filled by condensation by further raising the vapor pressure to saturation. Once filled, the chamber temperature was lowered to initiate freezing in the nanochannels and confined phase equilibrium was captured with a CCD camera positioned above the chamber. The nanoconfined water-ice phase equilibrium was successfully captured as shown in Figure 3. The melting temperatures of confined ice were reported in Figure 4 and were consistent with the Gibbs-Thomson prediction.

Conclusions:

A microfluidic device consisting of high aspect ratio nanochannels was fabricated. A layer of ~ 200 nm Si_3N_4 was deposited underneath the channels, resulting in detectable contrast between the liquid water and ice in the channels. The melting temperatures of confined ice agreed with the Gibbs-Thomson relation. Continued work will focus on studying the transport dynamics of ice-water in confinement.

Acknowledgements:

Professor Abraham Stroock, Hanwen Lu, Melanie-Claire Mallison, CNF REU Program Coordinators, and CNF Staff. This work was completed in part at the Cornell NanoScale Science and Technology Facility, an NNCI member, which is supported by the NSF (Grant No. NNCI-1542081). This work was supported in part by a grant from the Air Force Office of Scientific Research (FA9550-18-1-0345).

References:

- [1] Bartels-Rausch, T., et al. "Ice structures, patterns, and processes: A view across the icefield." *Rev. Mod. Phys.* 2012, 84, 885.
- [2] Wettlaufer, J., et al. "Premelting Dynamics." *Annu. Rev. Fluid Mech.*, 2006, 38, 427-452.
- [3] Liu, Z., et al. "Measurement of freezing point depression of water in glass capillaries and the associated ice front shape." *Phys. Rev.*, 2003, 67, 6.
- [4] Li, H., et al. "Direct visualization of fluid dynamics in sub-10 nm nanochannels." *Nanoscale*, 2017, 9, 9556.

Fabricating 2D Silica with Atomic Layer Deposition

Reed Yalisove, 2018 CNF REU Intern

Materials Science and Engineering, University of Michigan

REU Program: 2018 Cornell NanoScale Science & Technology Facility Research Experience for Undergraduates Program

CNF REU Principal Investigator: Professor James R. Engstrom, Richard F. Smith School of Chemical and Biomolecular Engineering, Cornell University

CNF REU Mentor: Taewon Suh, Richard F. Smith School of Chemical and Biomolecular Engineering, Cornell University

Primary Source of CNF REU Funding: National Science Foundation via the National Nanotechnology Coordinated Infrastructure (NNCI) Grant No. ECCS-1542081

Contact: reedy@umich.edu, jre7@cornell.edu, ts695@cornell.edu

Website: http://www.cnf.cornell.edu/cnf_2018reu.html

Abstract:

Two-dimensional (2D) materials exhibit exciting new properties that could have applications for next-generation electronic devices. One such material is 2D silica, called silicatene, which is an SiO_2 bilayer that only binds to a surface via van der Waals forces. Previous research has shown that silicatene can be made via evaporation of Si and subsequent annealing in oxygen on a few single-crystalline metal surfaces, including Pd, Pt, and Ru. Atomic layer deposition (ALD) is a thin-film deposition technique used in the manufacturing of a variety of devices. This process repeats two self-limiting reaction steps to deposit a thin film, allowing angstrom-scale control of film thickness. The focus of this project was to investigate the use of ALD to deposit silicatene on several metal substrates. The metal films were deposited on silicon wafers via electron-beam assisted evaporation, and silica films were deposited with ALD. Post-deposition characterization of deposited film includes ellipsometry, contact angle, and x-ray photoelectron spectroscopy (XPS).

Introduction and Goals:

The thinnest stoichiometric arrangement of silica is a bilayer of silicon dioxide, known as silicatene. This material adheres to its substrate through van der Waals forces (see Figure 1). Silicatene has been fabricated on single crystal palladium (Pd), platinum (Pt), and ruthenium (Ru).

Silicon (Si) was evaporated onto the metal substrate with an electron-beam assisted evaporator, then the films are annealed near 800°C and 10^{-6} mbar in an oxygen-rich environment [1].

Atomic layer deposition (ALD) is a thin-film deposition technique in which two self-limiting reactions are repeated, forming a film, atomic layer-by-atomic layer. This method allows low-temperature deposition of

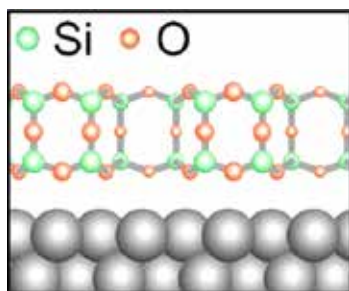


Figure 1: Figure adapted from ref. [1], the structure of silicatene. It consists of a bilayer of SiO_2 molecules attached to a metal substrate via van der Waals forces.

highly conformal, uniform films [2]. This research aimed to fabricate silicatene using ALD.

Methods:

We chose Pd, Pt, and Ru as metal films for SiO_2 ALD. These metals were deposited on p-type silicon using an electron beam-assisted evaporator. Each metal film was 150\AA thick, and the Pt film was deposited on a 100\AA thick Ti adhesion layer on Si. Metal films were characterized with contact angle and ellipsometry. SiO_2 films were deposited with ALD, using tris(dimethylaminosilane) (3DMAS) precursor and O_2 plasma as a co-reactant. Before the precursor was introduced, substrates were reduced in a H_2 plasma.

Films were deposited at 200°C , with 5, 10, 20, 50, and 100 cycles of ALD. In addition, a "0 cycle" sample was created, which was not exposed to the Si precursor or the O_2 plasma, and a "20 second-half cycle" sample was created, which was not exposed to the 3DMAS, but did undergo 20 cycles of the O_2 plasma co-reactant. Samples

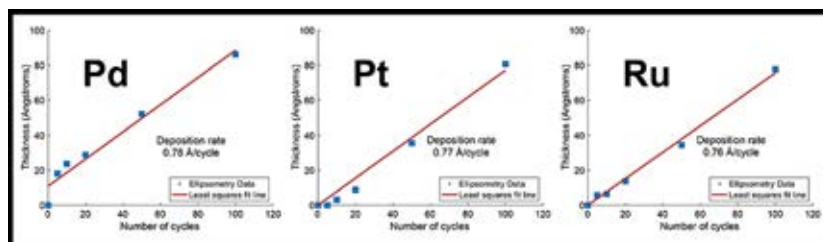
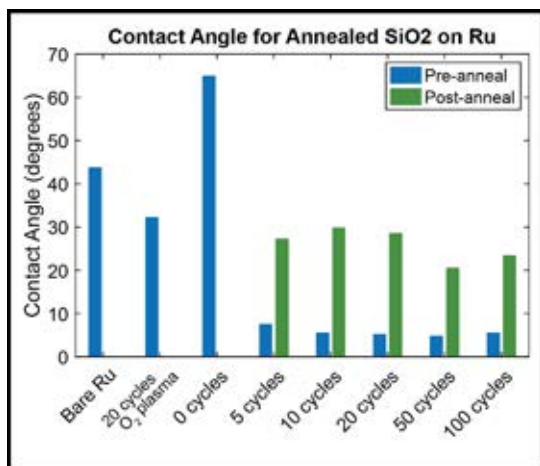


Figure 2, left: Contact angle data before and after annealing. Before annealing, contact angle is high without the introduction of Si precursor. When the Si precursor is introduced, the contact angle is consistently low. After annealing, the contact angle increases. **Figure 3, above:** Ellipsometry data before annealing. All metals show a linear increase in thickness with number of ALD cycles.

were annealed in an oxygen environment at 800°C for 10 minutes at atmospheric pressure, then were allowed to cool to 300°C. Samples were characterized with contact angle, ellipsometry, x-ray photoelectron spectroscopy (XPS), and angle-resolved XPS (ARXPS) before and after annealing.

Results:

Contact angle showed high angles of water contact for the samples that were not exposed to the Si precursor (bare metal, 0 cycles, and 20 second-half cycles). The contact angles for the pre-annealed samples that were exposed to the Si precursor were uniform and low. This data shows that the exposure to the Si precursor caused a change on the sample surface, suggesting that SiO₂ was deposited.

After annealing, contact angles were high, which is inconsistent with the expectation for silicatene. This trend (summarized in Figure 2) was observed for all three. Ellipsometry data shows a linear increase in thickness with the number of ALD cycles for all metal substrates, as seen in Figure 3. This suggests that we observed normal ALD behavior, as the formation of silicatene would have led to an asymptote in the film thickness because it is unlikely the complete bilayer would have reacted with additional precursor due to the lack of dangling bonds.

Ellipsometry data for the annealed samples was different than that of the pre-annealed samples, and it could not be fit to the expected models. XPS confirmed that the amount and thickness of SiO₂ increased with the number of ALD cycles. ARXPS showed that before annealing, our sample consisted of a thin film of SiO₂ on a buried Ru substrate. After annealing, ARXPS still showed a layer of SiO₂ on top of the sample but the morphology of Ru was inconclusive.

Conclusions:

XPS and ellipsometry suggest that silicatene was not produced. It is likely that during annealing, the SiO₂ combined with the metal to form metal silicides. This is supported by the change in contact angle after annealing and a study showing that Si will diffuse into metals, forming silicides [3]. This would also change the optical constants of the film, which caused the failure of the ellipsometry models.

Future Work:

Successful silicatene fabrication involved single crystal metal substrates [1], whereas our metal films were amorphous due to their evaporation. As a result, we would like to replicate this experiment on single-crystalline metal substrates.

Acknowledgements:

I would like to thank the CNF and its funding sources. Additionally, I would like to thank my PI, James R. Engstrom, and my mentor, Taewon Suh, for their willingness to give me a role in this research. I would like to give special thanks to Aaron Windsor for his patience and help with the evaporator, without which I would not have been able to complete my research.

References:

- [1] Büchner, C., and Heyde, M. (2017). Two-dimensional silica opens new perspectives. *Progress in Surface Science*, 92(4), 341-374.
- [2] George, S. M. (2010). Atomic Layer Deposition: An Overview. *Chemical Reviews*, 110(1), 111-131.
- [3] Petersson, C., Baglin, J., Dempsey, J., D'Heurle, F., and La Placa, S. (1985). Silicides of ruthenium and osmium: Thin film reactions, diffusion, nucleation, and stability. *Vacuum*, 35(6), 237.

Systematic Floating Zone Single Crystal Growth for Machine Learning Objectives

Jessica Zahn, 2018 PARADIM JHU REU Intern

Chemistry, Math, The University of the South

REU Program: 2018 Platform for the Accelerated Realization, Analysis, and Discovery of Interface Materials Research Experience for Undergraduates Program at Johns Hopkins University (PARADIM JHU REU)

PARADIM JHU REU Principal Investigators: Dr. Tyrel M. McQueen, Chemistry, Johns Hopkins University; Dr. W. Adam Phelan, Chemistry, Johns Hopkins University

Primary Source of PARADIM JHU REU Funding: Support for PARADIM is provided under NSF Grant # DMR-1539918 as part of the Materials Innovation Platform Program

Contact: zahnjl0@sewanee.edu, mcqueen@jhu.edu, wphelan2@jhu.edu

Websites: <http://paradim.cornell.edu/education>, http://www.cnf.cornell.edu/cnf_2018reu.html

Abstract:

PARADIM is an NSF-sponsored program that provides users access to the platform's world unique equipment in order to expand their research and encourage discovery of new materials at an accelerated rate via materials design. In particular, the development of unique floating zone furnaces has led to a dramatic increase in the discovery of new materials with desirable properties (e.g. magnetic frustration). However, users are often unfamiliar with the equipment, and extensive training is often required for the acquisition of initial results. In order to assist the inexperienced user, machine learning software is being developed by the PARADIM DATA Collective (PDC) for the floating zone furnaces. At present, data were generated from a variety of floating zone growths to develop training sets. By landmarking key points from video footage, a computer can be trained to gauge the success of experiments. Subsequently, a computer can make recommendations to the user for on-the-fly experimental parameter changes should an experiment reach an unhealthy state.

Summary of Research:

A variety of floating zone growths were completed with parameters systematically manipulated to generate a diverse set of data. Key points of the experiments were selected to be landmarked for the training set. A python script was developed to extract the key parameters, such as laser position and inclination, rotation rate and direction, and feed rate and direction of both rods, and the laser power used, from the video data. Three main types of growth were characterized by the respective widths of the top, neck, and bottom of the molten zone: healthy (Figure 1), thinning (Figure 2), and convex (Figure 3). The potential causes and additional characterization, such as movement of the rods or molten zone, of these three types of molten zones were also determined.

in the same direction, no jerking motion of either rod, and little to no changes in molten zone shape or growth parameters.

In contrast, a thinning molten zone, seen in Figure 2, consists of the width of the bottom solid/liquid interface being much larger than the neck and the top of the molten zone. Thinning molten zones are problematic because they lead to separation of the rods and potentially end the growth. They can be caused by the top feed rate being too slow to keep up with the seed rods travel rate, the power being too low to melt enough of the material, or the rods being too far apart. Thus, a thinning molten zone can be fixed by increasing the top feed rate, decreasing the bottom feed rate, increasing the power, or moving the rods closer together manually.

Results and Conclusions:

Analysis of floating zone data led to the determination of three main categories of floating zones: healthy, thinning, and convex. Healthy floating zones, depicted in Figure 1, were characterized by a 11:10:11 ratio of widths of the top: neck: bottom of the molten zone, rods travelling

Conversely, a convex molten zone (Figure 3) has a molten zone neck that is wider than the top and bottom rods, which consequently can cause the molten zone to fall. The top rod moving proportionately too quickly or the power being too high can produce a convex molten zone.

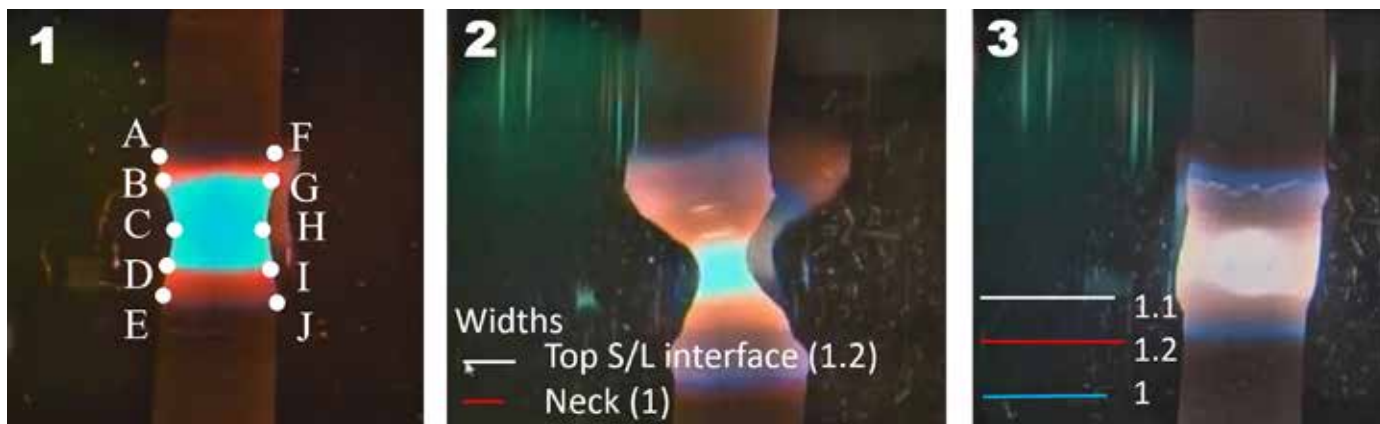


Figure 1, left: Landmarked image of a healthy molten zone marking the edge of the top rod (A,F), top of the molten zone (B,G), “neck” of the molten zone (C,H), bottom of the molten zone (D,I), and edge of the bottom rod (E,J). Figure 2, middle: Thinning molten zone due to user error. Respective widths of various parts of the molten zone characterize it as unhealthy. Figure 3, right: Convex molten zone characterized by the neck of the molten zone being the widest point.

By systematically altering parameters one at a time throughout a variety of experiments, a diverse training set of successful and unsuccessful crystal growths was developed. After inputting this data into a computer program, the computer will recognize not only when a growth is failing, but what parameters must be adjusted. Furthermore, the computer will be able to predict values such as crystal size and density, time left in the growth, and the melting point of the material via simple equations, such as the ones seen in Figure 4.

More complex equations can also be implemented into the program to allow the computer to compute this experimental data automatically. Because the program

$$Vol_{crys} = \pi \left(\frac{w_{crys}}{2} \right)^2 h_{crys}$$

$$h_{crys} = \frac{w_t^2}{w_{crys}^2} * \frac{d_t}{d_{crys}} * h_t$$

$$d_{crys} = \frac{d_t h_t}{h_{crys}} * \frac{w_t^2}{w_{crys}^2}$$

Figure 4: Sample calculations of crystal height, volume, and density desired from the machine learning program. Note: calculations assume no vaporization.

will have access to thousands of data points, countless calculations will be performed giving the researcher a multitude of data about the material and growth that would have been otherwise lost or time consuming. Such an influx of data will streamline the process of materials research and improve the quality of results.

Future Work:

Further experiments using less traditional floating zone techniques must be conducted so that the data may be added to the training set. In addition to collecting more data, the landmarking program must be selected or developed. Subsequently, the selected training set can be officially landmarked and uploaded to the machine learning program. Once the program has learned sufficiently from the training set, it may be implemented.

Acknowledgements:

NSF Grant # DMR-1539918; Dr. David Elbert, Johns Hopkins University; Ali Rachidi, Johns Hopkins University.

References:

- [1] W.A. Phelan, J. Zahn, Z. Kennedy, and T.M. McQueen, “Pushing Boundaries: High Pressure, Supercritical Optical Floating Zone Materials Discovery,” Submitted J. Sol. St. Chem. (2018).

Spin-Orbit Torques from SrRuO₃-SrIrO₃ Epitaxial Heterostructure

Cyrus Zeledon, 2018 PARADIM CU REU Intern

Materials Science and Engineering, Cornell University

REU Program: 2018 Platform for the Accelerated Realization, Analysis, and Discovery of Interface Materials Research Experience for Undergraduates Program at Cornell (PARADIM CU REU)

PARADIM CU REU Principal Investigator: Professor Darrell G. Schlom, Materials Science and Engineering, Cornell University

PARADIM CU REU Mentor: Dr. Ludi Miao, Physics, Cornell University

Contact: cz265@cornell.edu, schlom@cornell.edu, lm783@cornell.edu

Primary Source of PARADIM CU REU Funding: Support for PARADIM is provided under NSF Grant # DMR-1539918 as part of the Materials Innovation Platform Program

Websites: <http://paradim.cornell.edu/education>, http://www.cnf.cornell.edu/cnf_2018reu.html

Abstract:

Spin-orbit torques can be generated in two different ways: the Rashba-Edelstein effect and the spin Hall effect. These effects generally occur in trilayer heterostructures consisting of an oxide, ferromagnet, and heavy metal layer. SrRuO₃-SrIrO₃ heterostructures grown on varying substrates (NGO, STO, DSO, and GSO) should generate a spin-orbit torque at the interface. Spin torque ferromagnetic resonance and second harmonic Hall voltage measurements will be used to determine the effect that dominates the spin-orbit generation at the heterostructure's interface.

Summary of Research:

The purpose of the study was to determine the spin-orbit torques generated by a heterostructure consisting of a ferromagnetic layer coupled with a heavy metal layer. Strontium ruthenate (SRO) and strontium iridate (SIO) were chosen as the ferromagnetic and heavy metal layers, respectively. SRO is a 4d transition metal oxide that behaves as a ferromagnet below 150 K, and SIO is a 5d transition metal oxide with strong spin-orbit coupling. The heterostructures will be grown on different substrates, which will affect the magnetization of the ferromagnetic thin film. The mechanisms in which the torques can be generated is through the Rashba-Edelstein effect or the spin Hall effect.

To measure the films, they must be patterned via photolithography, deposited with metal (typically platinum) contacts, and ion milled to isolate channels on the sample. Two devices were made to test the spin-orbit torques: ST-FMR devices and Hall bars. All device fabrication was done at the Cornell NanoScale Science & Technology Facility (CNF).

If the samples depend on the thickness of the ferromagnetic layer, then the spin-orbit torques will be generated via the spin Hall effect; otherwise, the Rashba-Edelstein effect (REE) will be the reason for the spin-orbit torques. Similar to the splitting of charges on opposite lateral ends in the classical Hall effect, the spin Hall

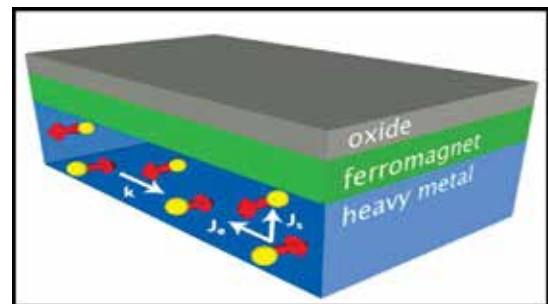


Figure 1: Spin-orbit torques are generated in an oxide, ferromagnet, and heavy metal trilayer. The spin Hall effect occurs when conduction electrons flow through the heavy metal layer drift due to their spin polarization and generate a spin current that flips the magnet moment of the ferromagnet.

effect (SHE) separates spin-up and spin-down electrons on the lateral surface. Figure 1 shows the SHE and the spin current generated from it, which flips the magnetic moment of the ferromagnetic layer. On the other hand, the Rashba effect occurs when the spin band splits since there exists a structural inversion asymmetry.

The Rashba effect is thickness independent, meaning the change in layer size of the ferromagnet or heavy metal will not affect the spin-orbit torque. REE can manipulate

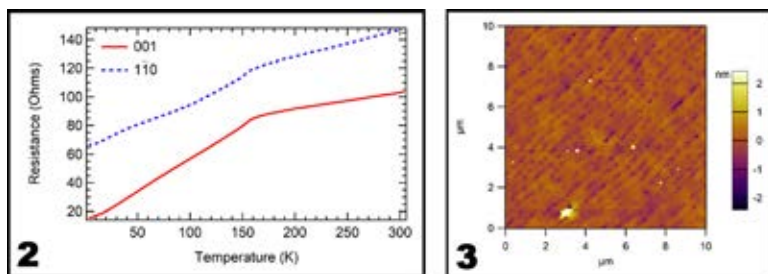


Figure 2, left: The resistance versus temperature of the SRO-SIO heterostructure shows an anisotropy in direction since $\langle 001 \rangle$ and $\langle 110 \rangle$ have a difference of ~ 50 Ohms at each temperature. Figure 3, right: The SRO-SIO heterostructure has step-terraces on the surface of the film. The step height of a step-terrace is 0.2 nm. There are some defects on the film, such as the 2 nm bump.

the magnetization of a material by flowing a charge current through the ferromagnetic layer, which generates a net spin accumulation.

Results and Conclusions:

One sample was grown on August 5, and was characterized with atomic force microscopy (AFM), x-ray diffraction (XRD), and transport measurements to ensure a high quality heterostructure was grown. The transport measurements of SRO-SIO heterostructure showed an anisotropy of 50 Ohms between measurements of $[001]$ and $[110]$. Figure 2 shows the anisotropy measured in the film and a distinct resistance versus temperature curve similar to that of SRO. AFM was then performed to check the film surface for any surface defects that would explain the anisotropy in the bilayer. Figure 3 shows clear step-terrace formations of the SIO layer with some bumps which may correspond to a defect from the ruthenium layer that propagated to the surface layer. XRD was used to determine the thickness of the layers and to check coherence of the strain between the layers. Figure 4 shows the reciprocal space map of the SRO-SIO film, which demonstrates the coherence in the strain throughout the heterostructure. No significant conclusions were made since the growth of the heterostructure occurred five days before the close of the program. The transport characterization showed an anisotropy which may suggest that the spin Hall magnetoresistance will also show an anisotropic behavior. No conclusions can be made about the spin orbit torque generation yet since the samples have not been fabricated with devices.

Future Work:

Once several heterostructures are grown in growth module 1 and 2 (GM1 and GM2), the sample will have devices fabricated on it at CNF. A mask will be made for the Hall bars, the ferromagnetic resonance measurements,

and potentially spin Hall magnetoresistance measurements. Spin torque ferromagnetic resonance (ST-FMR) measurements will be taken to study the effects off the spin orbit torque generated by the heavy metal and ferromagnet. The ST-FMR measurements will be taken with the setup in Professor Dan Ralph's group. Second harmonic Hall voltage measurements will be used to confirm the results from the ST-FMR. Depending on the results, angle-resolved photoelectron spectroscopy will be used to observe the band structure of the heterostructure and see if the spin Hall effect is evident from it. Both the second harmonic Hall voltage and spin Hall magnetoresistance measurements will be performed on the Vector magnet supplied by Professor Ralph. From these Hall measurements, the ST-FMR results will be compared to ensure the same conclusion is reached in terms of the spin-orbit torque generation at the interface of the bilayer.

Acknowledgements:

I would like to thank Professor Darrell Schlom for giving me the opportunity to investigate this heterostructure and providing support for my project. Support for PARADIM is provided by the NSF under grant # DMR-1539918 as part of the Materials Innovation Platform program.

References:

- [1] D.Bhowmik, O.Lee, L.You, and S.Salahuddin, Department of Electrical Engineering and Computer Sciences, University of California Berkeley, John Wiley & Sons, Ltd.
- [2] D.MacNeill, G.Stiehl, M.Guimarães, N.Reynolds, R.Buhrman, and D.Ralph. Physical Review B 96, 054450 (2017).
- [3] Matsuno, et al., "Interface-driven topological Hall effect in SrRuO₃-SrIrO₃ bilayer", Sci. Adv. (2016).
- [4] M.Hayashi, J.Kim, M.Yamanouchi, H.Ohno, "Opportunities at the Frontiers of Spintronics", Phys.Review B 89, 144425 (2014).

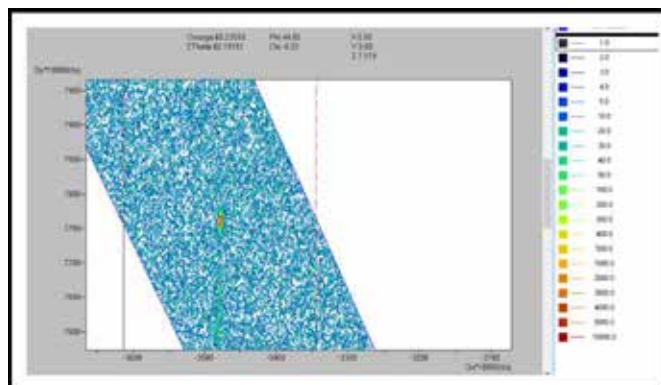


Figure 4: Reciprocal space maps of the $\langle 113 \rangle$ peak shows that the SRO-SIO heterostructure is strained coherently throughout the layers.

Development of a Multipurpose Ultrahigh Vacuum System for Electrical and Optical Measurements of Surface-Modified Quantum Materials

William Zhang, 2018 PARADIM REU @ Cornell Intern

Mechanical Engineering, Cornell University

REU Program: 2018 Platform for the Accelerated Realization, Analysis, and Discovery of Interface Materials Research Experience for Undergraduates Program at Cornell (PARADIM REU @ Cornell)

PARADIM REU @ Cornell Principal Investigator: Prof. Kyle Shen, Department of Physics, Cornell University

PARADIM REU @ Cornell Mentor: Brendan Faeth, Department of Physics, Cornell University

Primary Source of PARADIM REU @ Cornell Funding: Support for PARADIM is provided under NSF Grant # DMR-1539918 as part of the Materials Innovation Platform Program

Contact: wz76@cornell.edu, kth62@cornell.edu, brendanfaeth@gmail.com

Websites: <http://paradim.cornell.edu/education>, http://www.cnf.cornell.edu/cnf_2018reu.html

Abstract:

The goal of The Platform for the Accelerated Realization, Analysis, and Discovery of Interface Materials (PARADIM) is to discover and characterize quantum materials, specifically superconductors. The challenge with synthesizing and characterizing most quantum material samples is that they are extremely air sensitive, meaning that exposure to atmospheric pressure will damage the sample making it unable to be characterized. At one atmospheric pressure, particulates in the air (dust) deposit onto the sample's surface making it impossible for instruments to characterize the sample. To combat this challenge, samples are synthesized and characterized in ultra-high vacuum (UHV). UHV is defined as any pressure below 10^{-9} torr. At low pressures, samples can be used for longer since they are not being ruined by air particulates. PARADIM has created a lab in 308 Duffield Hall at Cornell University that integrates molecular beam epitaxy (MBE) with material characterization instruments all connected in UHV, keeping the sample clean as they transport it from synthesis to characterization. During this summer, PARADIM was beginning to implement another UHV synthesis and characterization system at Cornell University. The goal of our project this summer was to help coordinate the layout of chambers in the PARADIM lab, as well as design UHV chambers that would be used by PARADIM Researchers.

Design Process:

Lab CAD Modeling. In order to achieve the goal of helping PARADIM users construct the layout for the lab and designing UHV Chambers, we first have to create an extremely accurate model of the PARADIM Lab. In Autodesk Inventor 2018, we created a model for the PARADIM lab that was accurate down to less than an inch. This step was important because it allowed PARADIM users to take models of chambers they designed and find where those chambers could fit.

Using a tape measure and a laser measuring tape, we first measured and modeled the general room dimensions and floor plan. After that, we measured the space objects such as cabinets and pipes take up and their relation to the walls of the lab. For the chambers that already existed in the lab (MBE), we used a computer aided design (CAD) model that had already existed in Shen's lab group's Dropbox and placed them in the model.

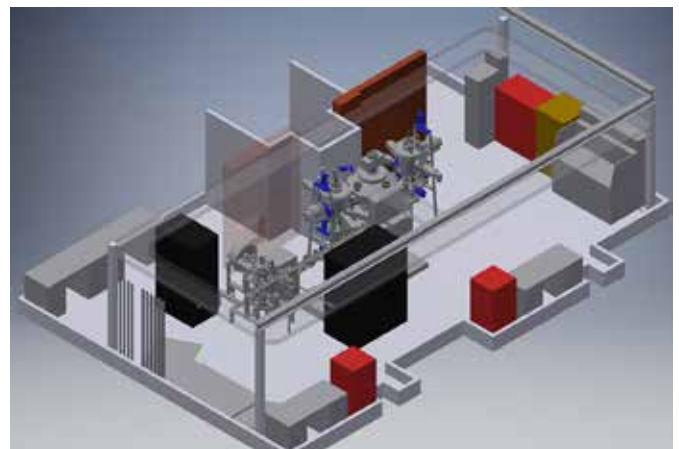


Figure 1: PARADIM lab model, proposed layout.

Upon completion of the model, we were tasked with helping Ed Lochocki and Luca Moreschini with placing chamber designs they were working on. Ed was working on a transfer tube that would allow users to transfer samples between chambers without taking them out of UHV and Luca was designing an ARPES chamber. We took suggestions from PARADIM users including PI, Professor Kyle Shen, and PARADIM director, Professor Darrell Schlom, and created a mock layout of the lab in Inventor Model. The current layout of the PARADIM Lab can be seen in Figure 1.

Sample Garage Design. In addition to creating the CAD model of the PARADIM Lab, we also worked on designing chambers that would be used by PARADIM users. The first design we worked on was a Sample Garage. One of the big limitations of the current system in Duffield 308 is the lack of samples that can be inside at a given time. Without a chamber dedicated to storing samples, users must grow their sample and measure them immediately. A storage chamber would allow users to have more flexibility when they characterize their samples. By having a sample garage, samples can be stored in UHV and can be used longer than what can be achieved currently.

For the sample garage design, we had several things we had to consider. The goal was to create a chamber that could store as many samples as possible in the smallest amount of space. Using a body that was 25 inches tall and 8 inches in diameter, we were able to design a sample garage that can hold up to 80 samples.



Figure 2: Storage sample garage.

Inside the chamber, there are four stacks of disks that each hold 20 samples. Each stack has two layers, a larger layer that can hold 12 samples and a smaller one that can hold 8 samples. Each disk will be made of aluminum, which will be waterjet cut at a machine shop. Within each sample holder space, there is a spring that secures the sample holder in place. The sample garage can be seen in Figure 2.

Aside from the design of the sample garage, we also had to design viewports and locations of transfer arms. We decided to place the transfer arm responsible for controlling the sample garage on the bottom of the chamber, so users could easily reach it. Since this sample garage would be attached to the transfer tube designed by Ed, a second arm was added which would be responsible for transferring samples in and out of the sample garage. We also added viewports that pointed to allow users to easily watch their sample as they were performing a sample transfer.

Future Work:

Towards the end of the summer, we began working on a surface science chamber. This is a characterization chamber that will be responsible for measuring the resistivity of a sample with respect to its temperature. This chamber is still in development and we will continue to work on it throughout next semester. The goal is to have this chamber to be part of the PARADIM Lab.

Acknowledgements:

I worked closely with my PI, Professor Kyle Shen, on my project and would like to thank him for this opportunity. Also thanks to my mentor, Brendan Faeth, for his guidance. I would also like to thank PARADIM REU for hosting and coordinating this program, especially Julie Nucci, Michele Conrad and Melanie-Claire Mallison for organizing. Lastly, I would like to thank the National Science Foundation who founded the REU program. Support for PARADIM is provided under DMR-1539918 as part of the Materials Innovation Platform program.

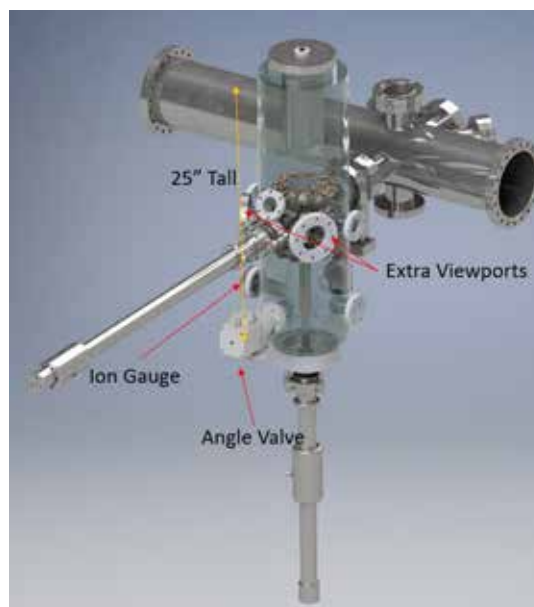


Figure 3: Storage sample chamber.

REU REPORTS INDEX

REU PROGRAMS

Cornell NanoScale Science & Technology Facility (CNF)	4, 24, 40, 46, 48
CNF International (CNF iREU) Program	8, 12, 18, 36, 42, 44
Center for Transportation, Environment & Community Health (CTECH)	2
Keeping the Ezra Promise (KEP)	6, 32, 38
Platform for the Accelerated Realization, Analysis, and Discovery of Interface Materials (PARADIM)	10, 14, 16, 20, 30, 34
PARADIM Cornell University (CU) REU	22, 28, 52, 54
PARADIM Johns Hopkins University (JHU) REU	26, 50

A

Aishee, Sayeeda Tuz Jahin	2
Alabi, Christopher	6
Alpha, Christopher	24
Anil, Vivek	4

B

Bohn, John	6
------------------	---

C

Castillo, Isabel	8
Castro-Rivera, Miguel	10
Chang, Peter	12
Chiew, Esther	2
Cimada da Silva, Jéssica Akemi	38
Coleman, Anthony	14

D

Daniel, Susan	32
---------------------	----

E

Eberly, Stephanie	16
Engstrom, James R.	48

F

Faeth, Brendan	54
Felstiner, Carl	18

G

Glushchenko, Iryna	20
Guélou, Gabin	44

H

Hanrath, Tobias	38
Ho Tai Ran, Ken	22
Holtz, Megan	14, 20
Howard-Jennings, Jordan Phillip	24
Huang, Steven He	4

J

Jung, Seok-Heon	24
-----------------------	----

K

Kennedy, Zachary	26
------------------------	----

L

Lee, Yonghun	28
Lema, Cesar	30
Lochocki, Edward	16
Lu, Hanwen	46

M

Mannino, Regina	32
Marracci, Marcus	34
McEuen, Paul	40
McQueen, Tyrel	26, 50
Miao, Ludi	52
Moreschini, Luca	16
Mori, Takao	44

N

Nakanishi, Jun	8
Nakayama, Tomonobu	42
Nelson, Jocienne	28
Noda, Takeshi	18
Nozick, Linda	2

O

Ober, Christopher	24
Ohashi, Naoki	12
Ohsawa, Takeo	12

P

Pamuk, Betül	10, 34
Pearson, Tanner	40
Perez, Paola	36
Phelan, W. Adam	26, 50
Pinnock, Ferra	32

R

Romo, Joshua	38
Ruf, Jacob	22
Russell, Sierra	40

S

Sagisaka, Keisuke	36
Sakai, Kazunori	24
Schlom, Darrell	10, 14, 16, 20, 30, 34, 52
Shcherbakov, Maxim	4
Shen, Kyle	22, 28, 54
Shvets, Gennady	4
Stroock, Abraham	46
Suh, Taewon	48

T

Teal, Daniel	42
Tsujii, Naohito	44

W

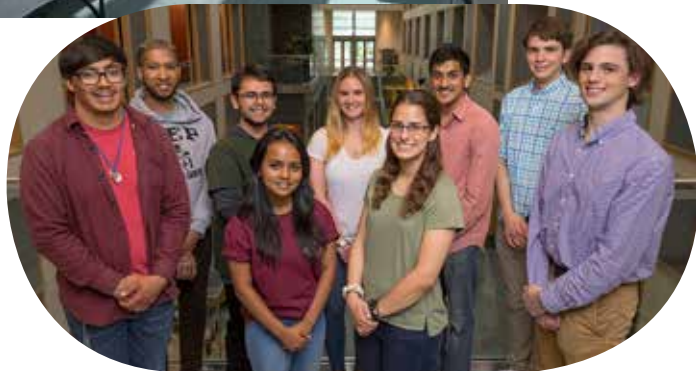
Walker, Joshua	6
Waybright, Jace	44
Werder, Don	30, 34
Whisnant, Kody	46

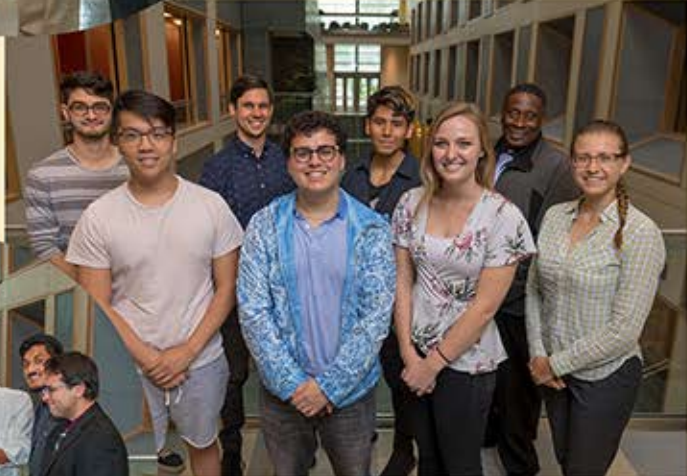
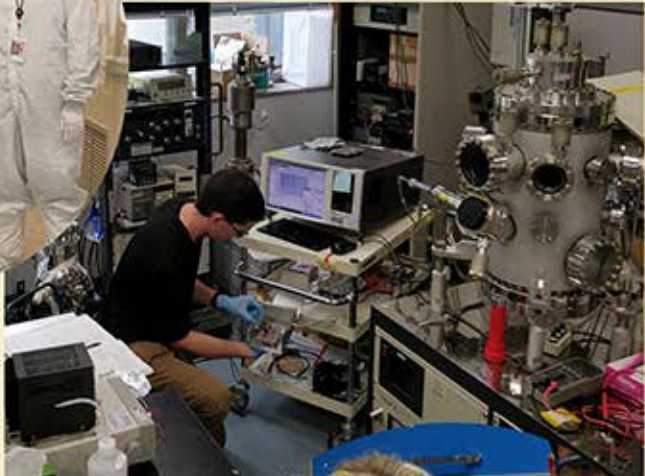
Y

Yalisove, Reed	48
Yamamoto, Shota	8

Z

Zahn, Jessica	50
Zeledon, Cyrus	52
Zhang, William	54





10nm

